博士論文

Long-Period Ground Motion Simulations using the Ambient Seismic Field

(地震波干渉法による長周期地震動シミュレーション)

ロイック　ヴィアンス

Abstract

Seismic waves generated by earthquakes have the potential to damage human-made structures and affect a large population worldwide. Japan, which is located at the junction of several tectonic plates, is under the constant threat of both subduction and crustal seismic events. In this context, the prediction of earthquake ground motions is critical to assess seismic hazard and prevent disasters. In this thesis, we focus on the long-period component of the ground motions ($\geq$ 1 s) which became a source of primary concern with the ever-increasing construction of large-scale structures, such as high-rise buildings, oil storage tanks, and suspension bridges.

Ground shaking is generally predicted using ground motion prediction equations (GMPEs) that are derived from records of past earthquakes. However, these equations suffer from a shortage of data for large earthquakes at short distances and are limited in their capability to accurately predict local site effects. Physics-based methods, which simulate the whole earthquake process from the source to a given site, have also been developed. However, such simulations require accurate velocity models and large computational resources to generate realistic waveforms.

Over the last decade, seismic interferometry has revolutionized seismology. This technique allows to extract the response of the Earth to a point force, called Green's function, between a pair of seismic stations that continuously record the ambient seismic field. Reliable phase and amplitude of Green's functions can be extracted through the deconvolu-

tion method by regarding seismometers located close to earthquake hypocenters as virtual sources and other stations as receivers. We take advantage of the ambient seismic field continuously recorded by thousands of seismometers in Japan to simulate long-period ground motions generated by different kinds of earthquakes.

We first demonstrate that after amplitude calibration, the extracted Green's functions can be used to simulate the long-period ground motions of a shallow M_w 5.0 subduction earthquake that occurred along the Nankai Trough. We use an offshore ocean bottom seismometer located in the vicinity of the earthquake epicenter as the virtual source and onshore stations as receivers. We show that the extracted offshore-onshore Green's functions can be used to accurately simulate the long-period ground motions generated by the offshore event. We also find that the distribution of the 5% damped pseudovelocity responses computed from the earthquake and Green's function waveforms have similar amplifications patterns.

Local velocity structures, such as sedimentary basins, can significantly affect the propagation of seismic waves through the Earth. We investigate the propagation characteristics of seismic waves across the Kanto basin, Japan, using Green's functions extracted from the ambient seismic field. We use two stations situated on the eastern and southern edges of the basin as virtual sources and the stations of the Metropolitan Seismic Observation network (MeSO-net), as receivers. Using dense seismometers aligned along two straight lines with the virtual sources, we find that several types of waves can be recovered, each with different sensitivities to the layers that compose the basin. We then compare the extracted Green's functions to the seismic waves generated by two moderate M_w 4–5 shallow earthquakes that occurred close to the virtual sources. For these two events, long-period ground motions are well simulated. This demonstrates all the power of dense networks that continuously record the ambient seismic field for assessing seismic hazard at high spatial resolution in metropolitan areas.

Large (M_w >6) earthquakes have the potential to generate damaging long-period ground motions. For such events, the point source hypothesis that is made for moderate earthquakes is no longer valid and an extended rupture needs to be taken into account. We focus on the 2008 M_w 6.9 Iwate-Miyagi Nairiku earthquake that occurred in the Tohoku region. We extract Green's functions between stations located in the vicinity of the mainshock fault plane and dozens of stations that are regarded as receivers. We calibrate the amplitude of the extracted Green's functions with the records of a M_w 5.0 aftershock which has a reverse faulting focal mechanism similar to the one of the mainshock. We use scaling relations between small and large earthquakes to construct simple finite source models that have similar parameters to the ones retrieved by source inversion studies. We compare the simulated waveforms obtained by the different source models and find a general good agreement with the observed records at long-periods. This study supports the fact that the ambient seismic field can be used together with simple finite source models to assess the seismic hazard related to large earthquakes.

We finally show that the deconvolution method can be used not only to simulate ground motions, but also to predict the motion of buildings during earthquakes. In the Tokyo metropolitan area, several large scale structures have been equipped with seismic sensors. We extract the response of a telecommunication tower located in the Kanagawa prefecture from earthquake data and ambient vibrations recorded at different heights of the structure. We first estimate several characteristics of the waves propagating in the structure, such as their velocity, frequency content, and attenuation. Using Green's functions extracted from the ambient seismic field, we simulate the long-period ground motions of a M_w 4.1 event which occurred in the Hakone region. We construct a finite source model that is used together with the extracted Green's functions to predict the ground motions of a hypothetical M_w 6.5 earthquake that could occur in the same area along the Sagami Trough. Simulated and predicted ground motions are finally convolved with the

tower response to simulate the building motions that could be caused by such moderate and large events. The integrated simulation from earthquake source to building motion shows promising results that might help to mitigate seismic risk.

Acknowledgments

I would like to express my gratitude to my advisor Professor Kazuki Koketsu for his guidance and support during these 3 years of PhD. I am very grateful to Dr. Hiroe Miyake for all the fruitful discussions, advice, and encouragements that greatly contributed to shape my research.

I am grateful to Professors Riki Honda, Tatsuya Itoi, Toshimi Kabeyasawa, and Koichi Kusunoki for their reviews and comments that helped to improve this thesis.

I acknowledge Hi-net/NIED and JMA for providing the continuous data. I am also thankful to JMA and F-net/NIED for the information about the earthquakes used in this study. I thank Naoshi Hirata, Shin'ichi Sakai, Shigeki Nakagawa, and all the MeSO-net project members for the MeSO-net data. The MeSO-net project is supported by the Special Project for Reducing Vulnerability for Urban Mega Earthquake Disasters from the Ministry of Education, Culture, Sports, Science, and Technology (MEXT) of Japan. I also acknowledge the Association of Electricity and Telecommunication Engineering for Land and Infrastructure and Koichi Kusunoki for the data of the Hazawa telecommunication tower.

I am also grateful to Fabian Bonilla, Marine Denolle, and Kiwamu Nishida for all the great discussions about this work. I also thank Shin'ichi Sakai and Takuto Maeda for valuable discussion about the OBS stations.

I acknowledge the Ministry of Education, Culture, Sports, Sciences and Technology

of Japan (MEXT), for awarding me a full financial support for these 3 years of Ph.D. at the Earthquake Research Institute, The University of Tokyo.

Last but not least, I thank Acha, Arlo, Haruka, Miko-chan, Saki-chan and Shige-chan, Yuki, all my Judo friends (specially Hide and Takashi) and others for making my stay in Japan a wonderful experience! Je remercie aussi ma famille pour m'avoir approvisionné, durant ces trois années à l'autre bout du monde, en fromage et autres gourmandises qui ont indéniablement contribué à la réussite de ce doctorat !

Contents

Chapter 1

Introduction

1.1 Background

Earthquakes are one of the most destructive geologic hazard and are currently threatening a large population worldwide. With the exception of tsunami and surface fault rupture, ground shaking induced by the passage of seismic waves is the principal destructive effect of earthquakes. In this context, the prediction of seismic waves generated by faulting is critical to accurately assess seismic hazard and mitigate their impact on human-made structures. The long-period component of the ground motion became a source of particular concern with the ever-increasing construction of large-scale structures, such as high-rise buildings, oil storage tanks, and suspension bridges. These long-period seismic waves slowly attenuate with distance and are very sensitive to local velocity structures, such as sedimentary basins, which have the potential to significantly amplify seismic waves even hundreds kilometers away from the hypocenter. Such phenomena was observed during several earthquakes in the past decades. One of the most dramatic example is the 1985 M_w 8.0 Michoacán earthquake, which destroyed or badly damaged hundreds of buildings in Mexico City situated approximately 350 km away from the epicenter (*Anderson et al.*, 1986; *Beck and Hall*, 1986). In Japan, long-period ground motions caused fires of oil

storage tanks during the 2003 M_w 8.3 Tokachi-oki earthquake in the Tomakomai region situated 250 km away from the hypocenter (*Koketsu et al.*, 2005). More recently, seismic waves generated during the 2011 M_w 9.0 Tohoku earthquake (United States Geological Survey (USGS) catalog) were significantly amplified in the Kanto region (*Takewaki et al.*, 2011) and in the Osaka sedimentary basin which is situated approximately 830 km away from the epicenter (Figure 1.1a). Sensors located on the 52nd floor of the Sakishima Office building, which is located in the center of the Osaka basin, experienced strong shaking at long periods (~7 s) as shown in Figure 1.1.

Since the occurrence time and shaking intensity of future earthquakes are currently unpredictable, seismic hazard needs to be accurately evaluated to mitigate earthquake losses. Two approaches are generally used to assess seismic hazard: deterministic and probabilistic. The objective of deterministic seismic hazard assessment (DSHA) is first to determine the location and characteristics of possible earthquake scenarios that might affect a given site. The next step is to compute synthetic seismograms to evaluate possible parameters of the ground motions (e.g., peak ground acceleration (PGA), peak ground velocity (PGV), peak ground displacement (PGD), and response spectra). On the other hand, probabilistic seismic hazard assessment (PSHA), first introduced by *Cornell* (1968), considers all possible earthquakes that can affect a given site and quantifies the probability of exceedance corresponding to various levels of a ground motion parameter, for a given exposure time. Both methods have differences, advantages, and disadvantages, and should be used together to provide complementary insights to the seismic hazard or risk problem (e.g., *McGuire*, 2001).

For both DSHA and PSHA approaches, ground shaking parameters need to be estimated. Until recently, these parameters were generally predicted using ground motion prediction equations (GMPEs). Hundreds of these equations (*Douglas*, 2014; *Bommer and Alarcón*, 2006), which are the results of multivariate regressions of ground motion

databases, have been developed to estimate PGA, PGV, or PGD at a given site for a specific earthquake scenario. However, GMPEs mostly suffer from insufficient data for large earthquakes at short distances and the difficulty of correctly accounting for site amplifications. In addition to GMPEs, physics-based methods, which simulate the whole earthquake process from the fault rupture to the propagation of radiating waves through the Earth, have been developed (*Komatitsch et al.*, 2004; *Olsen et al.*, 2006; *Furumura et al.*, 2008). In contrast to GMPEs, these simulations generate full waveforms from which ground motion parameters can be determined. However, the complexity of the source, path, and site effects makes difficult accurate predictions at all frequencies without complete knowledge of the velocity structure.

Over the last century, new opportunities have emerged in seismology through the use of the ambient seismic field that is continuously recorded by seismometers. The ambient seismic field, also called seismic noise, is mainly caused by human activities at periods shorter than 1 s and by natural activities, such as ocean waves and meteorological events, at longer periods (*Bonnefoy-Claudet et al.*, 2006). The short- and long-period components are called microtremors and microseisms, respectively. Spectral analysis of microseisms shows two distinct peaks (Figure 1.2). The primary peak exists in the period range of 12 to 20 s and the secondary peak, which has a larger amplitude, falls in the period range of 4 to 10 s. The primary microseism peak is generated by a nonlinear coupling of ocean wave energy into the seafloor by the shoaling action of waves in shallow water (*Hasselmann*, 1963). *Longuet-Higgins* (1950) demonstrated that the secondary microseism peak is generated by nonlinear pressure perturbations on the ocean bottom caused by the interference of two ocean waves traveling in opposite directions.

The first observation of the ambient seismic field was made by *Bertelli* (1872) and was followed by a study by *Gutenberg* (1911) about its nature and origin. Following these pioneer works, the ambient seismic field has been extensively used in seismology and

earthquake engineering. *Kanai et al.* (1954) showed that the maximum amplification period of the seismic noise at a given site depends on the nature of the soil. Then, *Kanai and Tanaka* (1961) and *Kanai et al.* (1966) showed that this maximum amplification period of the seismic noise is related to the predominant period of earthquake ground motions and can be linked to the damage caused to wooden houses during the 1944 M_w 8.1 Tonankai, 1948 M_w 6.8 Fukui, and 1964 M_w 7.6 Niigata earthquakes. *Aki* (1957, 1965) developed the spatial auto-correlation method (SPAC) to determine the velocity structure beneath an array of seismometers that record the ambient seismic field. This technique is based on the ratio between the azimuthal average of cross correlations computed from ambient seismic field records at a reference station and stations distributed along a surrounding circle, and the auto-correlation at the reference station. This ratio takes the form of a Bessel function from which the phase velocity dispersion curve, which is directly related to the underlying velocity structure, can be determined. Later, *Nogoshi and Igarashi* (1970, 1971) and *Nakamura* (1989, 2000) developed the horizontal-to-vertical Fourier amplitude spectral ratio (HVSR) method to provide an estimate of the site amplification function.

During the last decade, *Lobkis and Weaver* (2001) demonstrated that the cross correlation of a diffuse acoustic wavefield recorded by two sensors leads to the impulse response function of the medium in which the acoustic waves travel. *Campillo and Paul* (2003) showed that the cross correlation technique can be also used in seismology to extract the response of the Earth by cross correlating the late seismic coda part of earthquakes recorded by a pair of seismometers. Following this work, *Shapiro and Campillo* (2004) and *Sabra et al.* (2005) demonstrated that the cross correlation of ambient seismic field time series recorded by a pair of stations also allows to retrieve the response of the Earth from one station to another. Under the assumption of equipartition of ambient seismic source sources, the cross-correlation function yields to the Green's function. For simplicity, we call the Earth response as Green's function in the following, even if the appropriate

conditions are not fully satisfied. A schematic representation of the Green's function extraction from the ambient seismic field using seismic interferometry is shown in Figure 1.3. Ambient seismic field time series recorded at each receiver contain a coherent part that can be recovered after stacking the cross correlations over time. Extracted Green's functions mainly contain only the fundamental mode of surface waves because of the location of the sensors at the surface. However, under certain conditions, higher modes of surface waves and body waves might also be retrieved (*Savage et al.*, 2013; *Roux et al.*, 2005; *Poli et al.*, 2012; *Nakata et al.*, 2015a). Green's functions retrieved by seismic interferometry have been widely used in many passive seismology studies including imaging the Earth structure at local (*Mordret et al.*, 2014), regional (*Lin et al.*, 2008; *Nishida et al.*, 2008; *Shapiro et al.*, 2005), and global (*Boué et al.*, 2013) scales, estimating seismic anisotropy (*Takeo et al.*, 2013), monitoring velocity changes in volcanoes (*Brenguier et al.*, 2008a), or studying the response of the crust after a large earthquake (*Brenguier et al.*, 2008b).

Surface-to-surface Green's functions extracted with the deconvolution method have also been used for seismic hazard assessment purposes. By regarding one station located close to an earthquake epicenter (virtual source) and another station located in the surrounding area (receiver), the deconvolution without any preprocessing technique allows to extract Green's functions having both reliable phase and amplitude. *Prieto and Beroza* (2008) showed that the long-period ground motions (4–10 s) generated by a moderate M_w 4 class crustal earthquake can be accurately simulated by surface-to-surface Green's functions (Figure 1.4). Subsequently, *Denolle et al.* (2013) improved this method by correcting the surface-to-surface Green's functions for both the source depth and the double-couple focal mechanism of the targeting earthquake (Figure 1.5). *Denolle et al.* (2014a) extended the point source method to finite rupture modeling to predict the ground motions of several M_w 7 class earthquake scenarios that could occur along the San Andreas

fault. Their results agree quite well with the physics-based simulations of the CyberShake project (*Graves et al.*, 2011). However, it is still critical to evaluate the accuracy of this method by simulating the long-period ground motions of past large earthquakes. Finally, *Viens et al.* (2014) demonstrated that surface-to-surface Green's functions can be used together with high-frequency stochastic modeling to simulate broadband ground motions of moderate M_w 5 class events from 0.05 to 30 Hz.

Seismic interferometry by deconvolution is also a powerful tool to study the response of buildings. Such time domain analysis of the characteristics of a building is complementary to the traditional frequency domain approach that consists of finding the frequencies of vibration and corresponding mode shapes of a structure. Several studies (*Snieder and Şafak*, 2006; *Kohler et al.*, 2007; *Todorovska and Trifunac*, 2008; *Nakata et al.*, 2013) demonstrated that the response of a building can be extracted by deconvolution of earthquake waveforms recorded at different floors. *Prieto et al.* (2010) and *Nakata and Snieder* (2014) expended the technique to ambient vibrations that are continuously recorded by seismic sensors (Figure 1.6a). The building response is represented as a superposition of upgoing and downgoing waves that propagate inside the structure and that are reflected from boundaries. Several parameters of the seismic waves propagating in buildings can be determined from the extracted building responses, such as their velocity, attenuation, and frequency content. *Prieto et al.* (2010) showed that the shaking of a building during a moderate earthquake can also be accurately predicted by convolving the earthquake record at the basement with the building response (Figure 1.6b). *Nakata et al.* (2015b) also revealed that the 2011 M_w 9.0 Tohoku earthquake caused a reduction of the wave velocity inside a building located in the Tokyo metropolitan area. Such reduction of the wave velocity is linked to changes of the structure properties after the strong shaking that the authors interpreted as a weakening of the building.

1.2 Objectives

The purpose of this thesis is to demonstrate the potential of Green's functions extracted from the ambient seismic field to simulate/predict the long-period ground motions that can be generated by different kinds of earthquakes.

We focus on Japan, which has been well-documented as a highly seismically active area due to its tectonic setting at the junction of four tectonic plates: The Pacific and Philippine oceanic plates and the Eurasian and North American continental plates. This junction makes the Japanese islands under the constant threat of both subduction and crustal earthquakes. To record, analyze, and understand the whole earthquake process, thousands of seismic stations recording continuously the Earth motions have been installed across the country, making Japan one of the most well-instrumented country in the world. These seismometers are operated by different organizations, including the National Research Institute for Earth Science and Disaster Prevention (NIED), the Japan Meteorological Agency (JMA), local governments, and universities.

The tectonic setting combined to the huge amount of seismic data makes Japan an ideal natural laboratory to investigate the potential of the ambient seismic field for predicting ground motions. In this thesis, we choose to use only surface-to-surface Green's functions and do not bury the Green's functions at depth and correct for the surface-wave radiation pattern effects of earthquakes with the method proposed by *Denolle et al.* (2013). As we only target shallow events ($\leq$ 30 km) and their long-period seismic waves, the depth correction does not affect much the Green's functions. Moreover, such correction requires the velocity structure beneath the virtual source station which is not always precisely known. The effect of the surface-wave radiation pattern might be significant in some cases, and is only taken into account when simulations are made for stations distributed over an azimuth larger than approximately 90°. However, the correction that

is used to correct for this effect in this thesis is empirical and is different from the one proposed by *Denolle et al.* (2013).

The first goal of this study is to demonstrate that this technique can be applied not only to moderate crustal events (*Prieto and Beroza*, 2008; *Denolle et al.*, 2013), but also to moderate subduction earthquakes. Second, we aim to prove that the surface-to-surface Green's functions extracted between stations of a dense seismic network can be used to accurately map the amplification of the long-period ground motions caused by a sedimentary basin.

Japan has one of the most rigorous earthquake building codes in the world that ensure human-made structures to have adequate strength and ductility to survive without any damage to frequent moderate earthquakes. However, large ($M_w \geq 6$) earthquakes might generate damaging seismic waves. Such events have a finite source area that needs to be taken into account in the simulations. The third goal of this thesis is to demonstrate the accuracy of the method introduced by *Denolle et al.* (2014a) by simulating the long-period ground motions of a past large seismic event.

The good agreement between our simulations and the records of past earthquakes for the three cases previously described demonstrates the power of the method to assess seismic hazard. The fourth and final step of this thesis is to try to link seismology and earthquake engineering by using the simulated ground motions of moderate-to-large earthquakes together with the response of buildings to study the motions of human-made structures during such events.

1.3 Organization

After the general introduction presented in this first chapter, we focus in Chapter 2 on the recovery of Green's functions between offshore and onshore seismometers which con-

tinuously record the ambient seismic field. We use ocean bottom seismometers (OBSs) deployed along the Nankai Trough by JMA as virtual sources and Hi-net/JMA stations located onshore as receivers. We show that the extracted offshore-onshore Green's functions can be used to accurately predict the long-period ground motions generated by a moderate M_w 5.0 subduction earthquake which occurred in the vicinity of the OBSs. We also find that the earthquake and Green's function pseudovelocity responses at different periods have similar maximum amplifications in the Omaezaki region which is located close to the earthquake epicenter.

Chapter 3 is dedicated to the analysis of the propagation characteristics of seismic waves across the Kanto basin, Japan, using Green's functions extracted from the ambient seismic field. We use two stations situated on the eastern and southern edges of the basin as virtual sources, and approximately 420 stations, which are mainly a part of the Metropolitan Seismic Observation network (MeSO-net), as receivers. We find that several types of waves that are sensitive to the different layers that compose the basin can be recovered. We show that after amplitude calibration, the extracted Green's functions can accurately simulate the seismic waves of two moderate M_w 4–5 shallow earthquakes that occurred close to the virtual sources. Furthermore, we find that the distribution of the 5% damped pseudovelocity response at different periods computed from the records of each event and the Green's function waveforms have similar amplification patterns. This study supports the fact that dense networks recording continuously the ambient seismic field in metropolitan areas can be used to accurately assess seismic hazard at high spatial resolution.

In Chapter 4, we concentrate on the extension of the point source method to finite source modeling to simulate the long-period ground motions of large earthquakes. We choose the well-recorded Iwate-Miyagi Nairiku earthquake (M_w 6.9), which occurred on 14 June 2008 in the Tohoku region, Japan. This earthquake, which has a reverse

faulting mechanism, caused several fatalities, collapse of houses and a bridge, and severe landslides. To simulate the long-period ground motions (4–15 s) generated by this event, we take advantage of the ambient seismic field continuously recorded by seismic stations deployed by NIED, JMA, and the Tohoku University. Stations located in the vicinity of the mainshock fault plane are used as virtual sources and other stations as receivers. We use the deconvolution method to extract point force Green's functions between each pair of stations. We first show that after calibration of the amplitude, Green's functions accurately simulate the long-period ground motions of a moderate M_w 5.0 aftershock that occurred close to the mainshock hypocenter. To simulate the mainshock, we construct several finite source models which have similar characteristics to the ones determined by source inversion studies. The fault plane is first discretized into subfaults of the size of the moderate M_w 5.0 aftershock. We interpolate the Green's functions extracted between the virtual sources and each receiver to obtain one Green's function for each subfault. We finally initiate and spread the rupture radially from the hypocenter with a constant rupture velocity to simulate the long-period ground motions. We find that the simulated long-period ground motions for the different source models agree generally well with the earthquake records, which confirms the power of this technique to assess seismic hazard related to large earthquakes.

In Chapter 5, we link seismology and earthquake engineering by combining simulated ground motions and building responses to predict building motions during earthquakes. We first retrieve Green's functions between virtual sources located in the Hakone region and receiver stations located in the Kanto basin. The Green's functions are first used to simulate the long-period ground motions of a M_w 4.1 event which occurred in the Hakone region. We construct a finite source model that is used together with the extracted Green's functions to predict the ground motions of a hypothetical M_w 6.5 earthquake that could occur in the same area along the Sagami Trough. Using ambient vibrations recorded at

different heights of a telecommunication tower located in the Kanagawa prefecture, we extract the response of the structure and study the properties of the recovered seismic waves. Simulated and predicted ground motions are finally convolved with the tower response to simulate the building motions that could be caused by such moderate and large events.

Chapter 6, which is the last chapter of this thesis, presents the general conclusions of the thesis and future possible extensions. The different steps undertaken in this thesis are summarized in the flowchart in Figure 1.7.

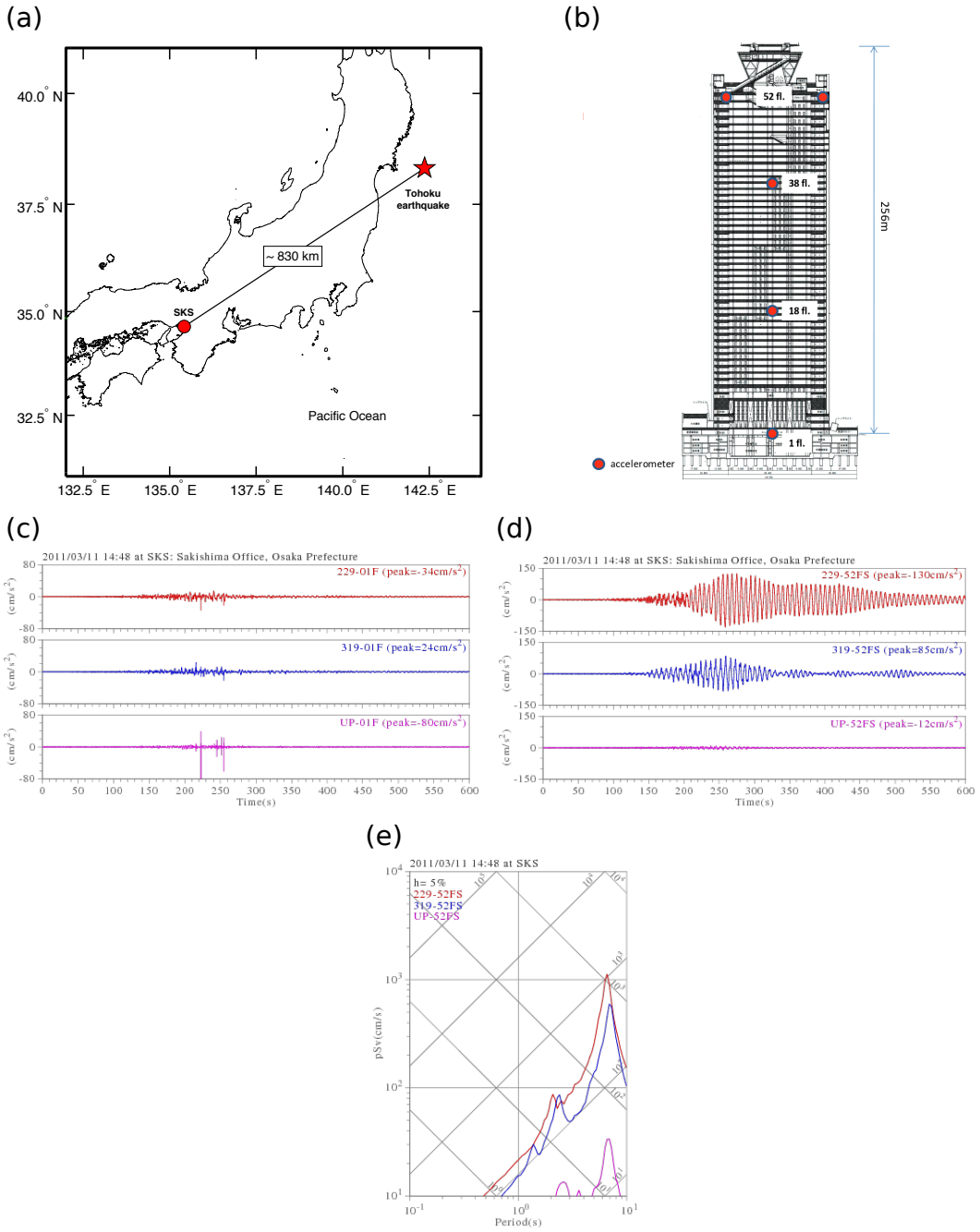

Figure 1.1: (a) Location of the M_w 9.0 Tohoku earthquake epicenter (red star) and the Sakishima Office building (red circle). (b) Sensor locations in the building. (c) Ground acceleration at the first floor of the building for the horizontal components (red and blue curves) and the vertical component (purple curve). (d) Ground acceleration recorded by one of the two sensors at the 52th floor. (e) 5% damped pseudo velocity response spectra of the records at the 52th floor (Fom BRI website, http://smo.kenken.go.jp/smreport/201103111446).

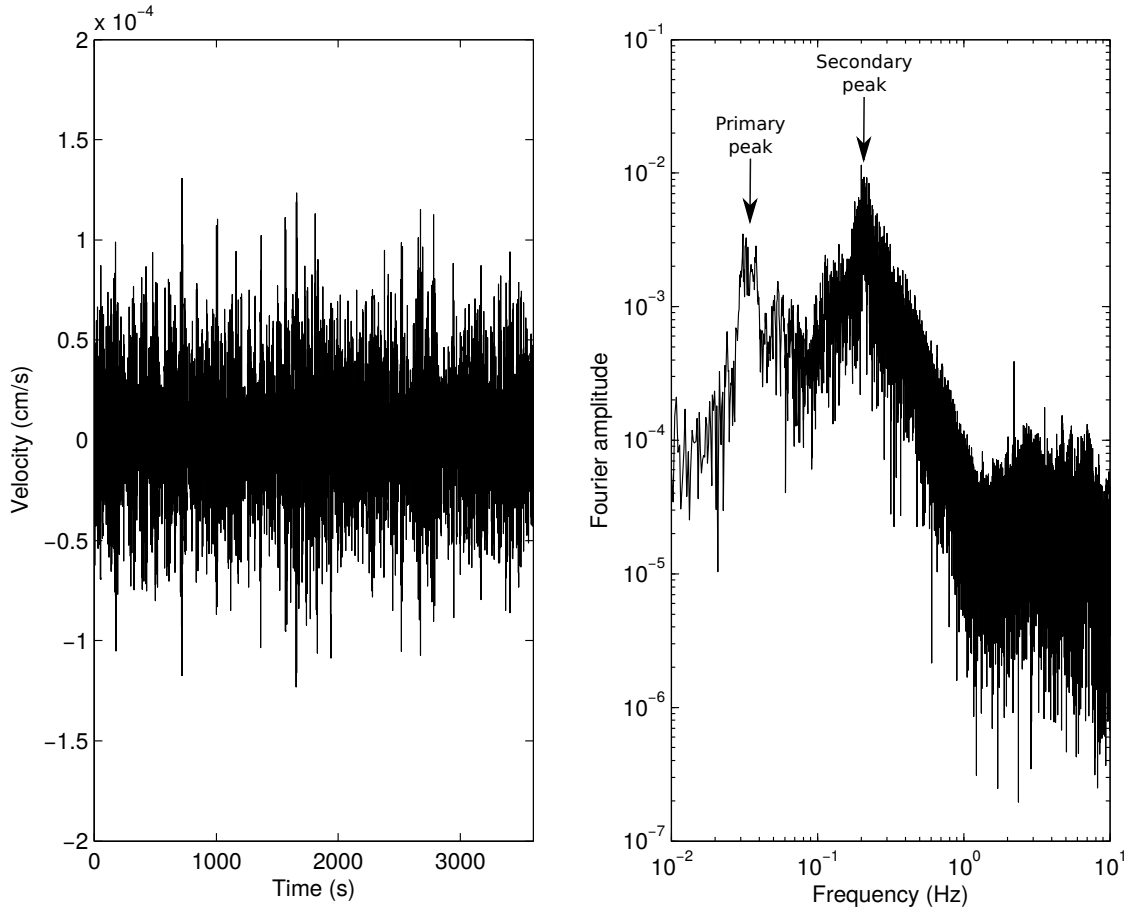

Figure 1.2: (a) One hour velocity waveform recorded by the F-net station N.TSKF (Ibaraki Prefecture) in January 2014 and (b) its Fourier spectrum. The primary and secondary microseism peaks are clearly visible at approximately 0.05 Hz (20 s) and 0.2 Hz (5 s), respectively.

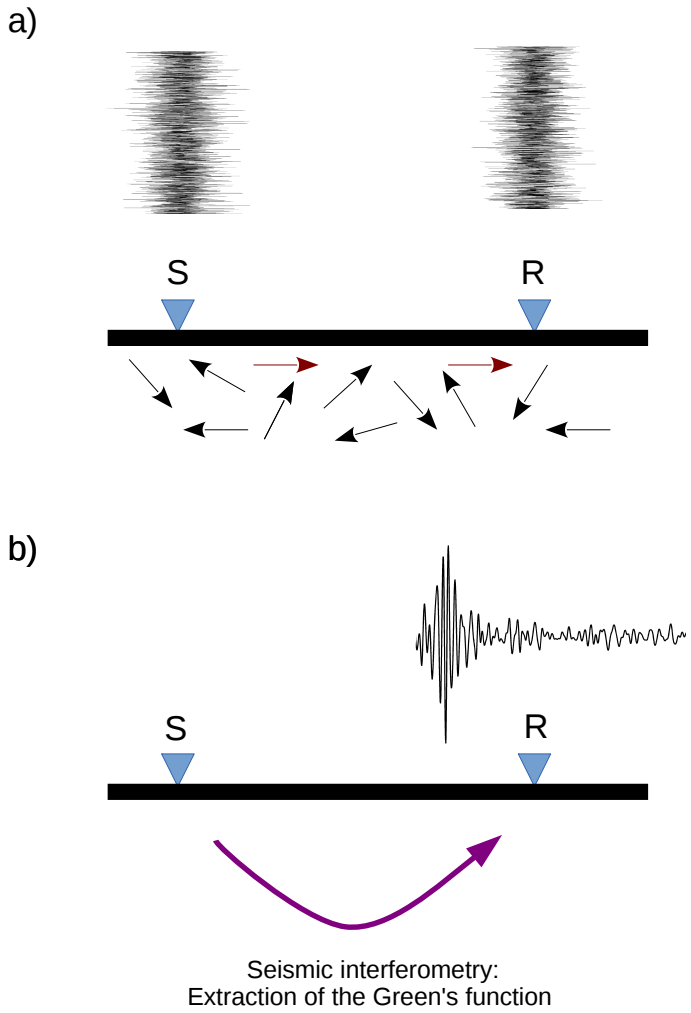

Figure 1.3: Schematic representation of the Green's function extraction from the ambient seismic field. (a) The ambient seismic field is recorded simultaneously at the virtual source (S) and receiver (R) stations. (b) By applying seismic interferometry (e.g., cross correlation, coherence, or deconvolution), the wave propagation between the two stations, which yields to the Green's function, can be retrieved.

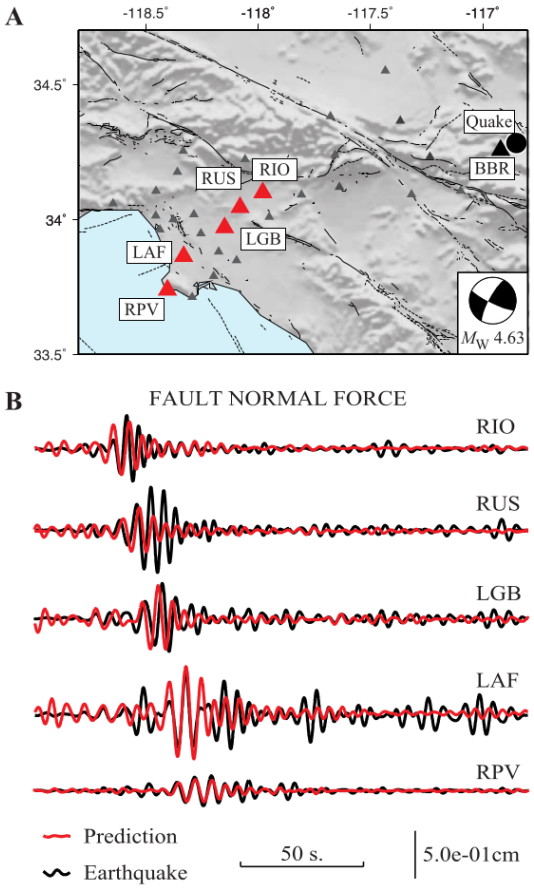

Figure 1.4: Simulation of the long-period ground motions of a M_w 4.6 earthquake which occurred close to the BBR station in California. Waveforms are shown for the radial component and are bandpass filtered between 4 and 10 s (From *Prieto and Beroza*, 2008).

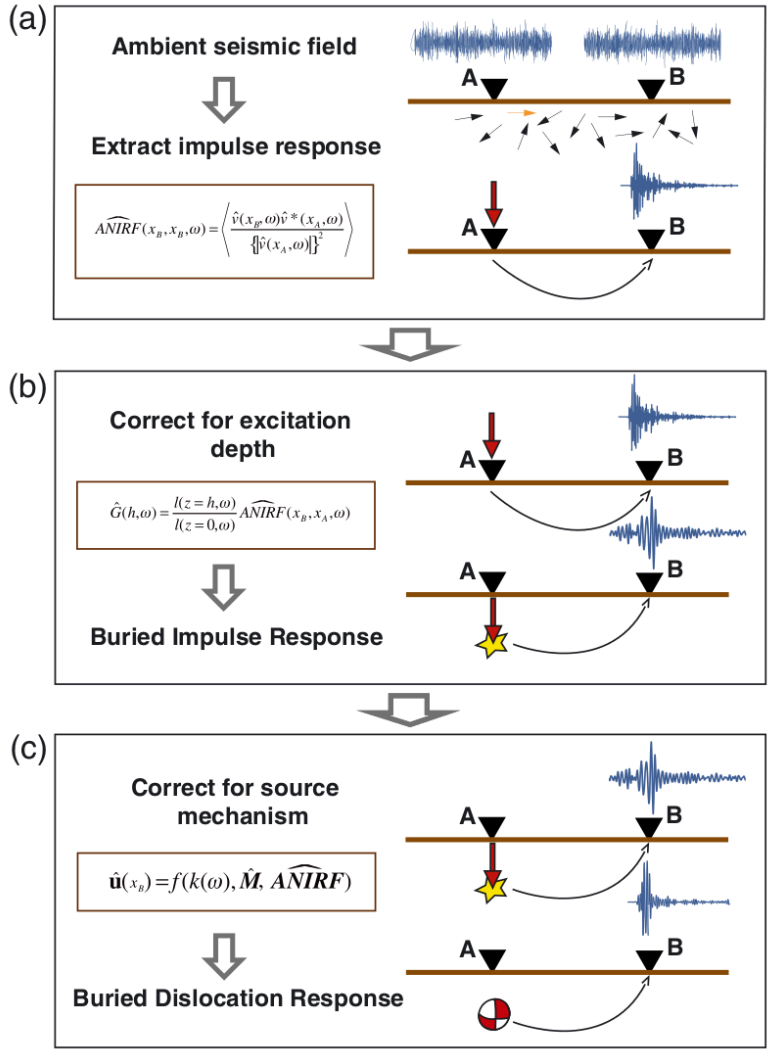

Figure 1.5: Schematic representation of the prediction of the ground motions using the method developed by *Denolle et al.* (2013). Green's functions are (a) extracted between seismometers located close to the Earth surface, (b) buried at the depth of the targeting earthquake, and (c) corrected for the focal mechanism of the earthquake (From *Denolle et al.*, 2013).

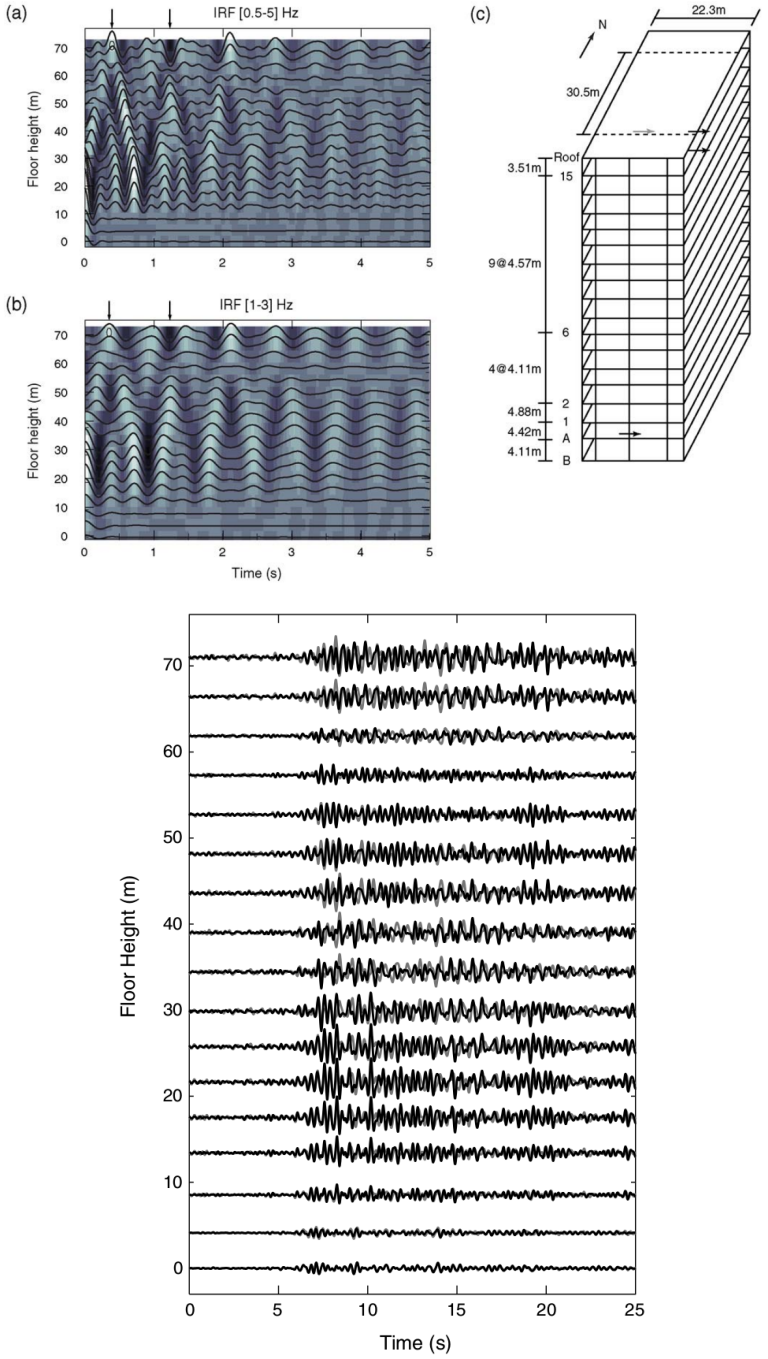

Figure 1.6: (top) Impulse response functions extracted from ambient vibrations at each floor, bandpass filtered between (a) 0.5 and 5 Hz, and (b) 1 and 3 Hz to illustrate the resonance of the second harmonic (1.6 Hz) of the building shown in (c). (bottom) Prediction of the building displacements at each floor by convolving the impulse response functions with the basement records of a M_w 4.2 earthquake. Predicted displacements (black) are very similar to the observed displacements (gray) for this earthquake (From *Prieto et al.*, 2010).

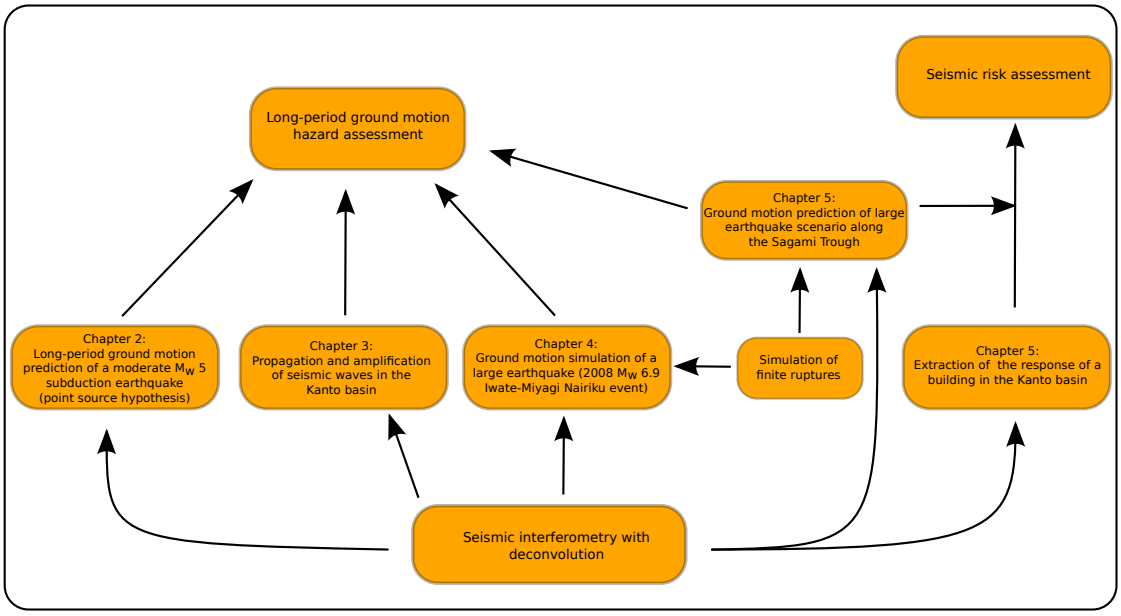

Figure 1.7: Flowchart of the thesis.

Chapter 2

Long-Period Ground Motion Simulation of a Subduction Earthquake using the Offshore-Onshore Ambient Seismic Field

This chapter has been slightly modified from Viens, L., H. Miyake, and K. Koketsu (2015), Long-period ground motion simulation of a subduction earthquake using the offshore-onshore ambient seismic field, *Geophysical Research Letters*, 42, 5282–5289, doi:10.1002/2015GL064265.

2.1 Introduction

The ever-increasing construction of large-scale structures, such as high-rise buildings, oil tanks, and suspension bridges, requires an accurate prediction of long-period ground motions to assess seismic hazard. Weak attenuation of long-period seismic waves and sensitivity of sedimentary basins to long-period seismic amplification yield significant

hazard for urban areas with large-scale structures that are threatened by distant megathrust earthquakes. One of the worst examples occurred during the 1985 Michoacán earthquake (M_w 8.0), in which hundreds of buildings were destroyed or badly damaged in Mexico City, situated more than 350 km from the hypocenter (*Anderson et al.*, 1986; *Beck and Hall*, 1986). Another example is the oil tank fires that occurred during the 2003 Tokachi-oki earthquake (M_w 8.3) in the Tomakomai region, Japan, situated more than 250 km from the hypocenter (*Koketsu et al.*, 2005).

Long-period ground motions ($T \geq 4$ s) are generally predicted using ground motion prediction equations (GMPEs). These equations, which are multivariate regressions of ground motion databases, mostly suffer from insufficient data for large earthquakes at short distances and the difficulty of correctly accounting for site amplifications. In addition to the GMPEs, physics-based methods that simulate fault rupture and propagation of radiating waves have been also developed (*Komatitsch et al.*, 2004; *Olsen et al.*, 2006; *Furumura et al.*, 2008). However, the complexity of the source, path, and site effects makes difficult accurate predictions at all frequencies without a complete knowledge of the velocity model.

Prieto and Beroza (2008) showed that ground motion generated by moderate crustal earthquakes can be accurately predicted using the ambient seismic field in the 4–10 s period range. Reliable phase and relative amplitude of the surface-to-surface Green's functions can be extracted from the ambient seismic field recorded at two stations by regarding one as a virtual source and the other as a receiver. Subsequently, *Denolle et al.* (2013) introduced the virtual earthquake approach by correcting the surface-to-surface Green's functions for the source depth and for the double-couple focal mechanism of the targeting earthquakes. Finally, *Denolle et al.* (2014a) extended this method from point sources to finite ruptures to simulate large-magnitude earthquakes, and *Viens et al.* (2014) demonstrated that surface-to-surface Green's functions can be coupled with stochastic

modeling to simulate broadband ground motions of moderate events from 0.1 to 30 Hz.

The prediction of the ground motions generated by subduction earthquakes that occur under the seafloor using the ambient seismic field is, however, more challenging due to the fact that the deployment of permanent ocean bottom networks remains costly. While interferometry methods have been successfully applied between ocean bottom seismometers (OBSs) to extract the phase velocity of Love and Rayleigh waves and to estimate velocity models (*Harmon et al.*, 2007) or seismic anisotropy (*Takeo et al.*, 2013) beneath oceanic regions, extraction of Green's functions between OBSs and onshore stations remains uncommon. For example, *Harmon et al.* (2012) used short-period Rayleigh wave group dispersion obtained by cross correlation of OBS differential pressure gauges and vertical components of onshore seismic stations to estimate the crustal shear velocity of the Sumatran fore arc. However, offshore-onshore cross correlations were only computed for two paths perpendicular to the coast, and their spectrograms revealed that signals only have energy in the 6 to 9 s period range, within the secondary microseism band. Thus, the extraction of Rayleigh and Love waves from the ambient seismic field recorded by three-component seismometers located offshore and onshore must still be demonstrated.

In southwest Japan, the Philippine Sea Plate is subducting beneath the Eurasian Plate along the Nankai Trough. Historically, megathrust earthquakes have occurred repeatedly with a recurrence interval of 100 to 150 years (*Ando*, 1975) and have caused severe damage in western and central Japan. In the northern part of the Nankai Trough, two cable OBS systems were deployed in 1979 and 2008 atop the subduction zone by the Japan Meteorological Agency (JMA), as shown in Figure 2.1. The first deployed cable is called Tokai and includes four OBS stations only equipped with vertical velocity seismometers. The second cable is called Tonankai and is composed of five OBS stations equipped with three-component velocity seismometers. We thus refer this area as the Tokai/Tonankai area in this chapter.

On 12 August 2011 at 04:37 (Japan Standard Time), a M_w 5.0 earthquake with reverse faulting mechanism occurred in the vicinity of the TK4OBS and TT5OBS stations at a depth of 11 km (National Research Institute for Earth Science and Disaster Prevention (NIED) centroid moment tensor solution). We use these two OBS stations as virtual sources and onshore Hi-net (*Okada et al.*, 2004; *Obara et al.*, 2005) and JMA stations in the surrounding area as receivers. Both onshore and OBS stations consist of short-period seismometers with natural frequencies of 1 and 4.5 Hz, respectively. To retrieve the long-period component of ground motion, we correct the data for instrumental responses using the time domain filter developed by *Maeda et al.* (2011). After the correction of instrument response, we extract the Green's functions between offshore and onshore stations and show that Rayleigh and Love waves can be retrieved. Then, we confirm that the offshore-onshore Green's functions can be used for accurate simulation of the ground motions generated by a moderate M_w 5.0 subduction earthquake in the Nobi basin, where amplification of the long-period ground motions has been observed during past earthquakes (*Miyake and Koketsu*, 2005). We finally show that the distribution of the 5% damped pseudovelocity response at a period of 6 s computed from both Green's function and earthquake waveforms exhibit similar amplification patterns.

2.2 Offshore-Onshore Ambient Noise Green's Functions

Green's functions are computed using the deconvolution method in the frequency domain ω between 1-h time series recorded by two seismic stations located in x_s (virtual source) and x_r (receiver) as

$$\widehat{G}_{ij}(x_r, x_s, \omega) = \left\langle \frac{\hat{u}_i(x_r, \omega)\hat{u}_j^*(x_s, \omega)}{\{|\hat{u}_j(x_s, \omega)|\}^2 + \xi} \right\rangle. \tag{2.1}$$

i and j are the ith component at the receiver position and the jth component at the source

position, respectively. $\langle\rangle$ denotes the stack of the Fourier-transformed 1-h time series over one month, and asterisk $*$ denotes the complex conjugate. To maintain the stability of the deconvolution, we smooth the denominator spectrum using a 20-point running average, denoted by $\{\}$, and we add a water level ξ that we set to 1% of the average spectral power. Finally, the inverse Fourier transform is computed to retrieve both anticausal and causal Green's functions in the time domain.

Takagi and Obara (2014) showed that the source of the ambient seismic field in Japan varies seasonally and is frequency dependent. In the Tokai/Tonankai area, the ambient seismic field is mainly derived from the Pacific Ocean during the summer and from the Japan Sea during the winter in the 4 to 8 s period range. For 2014, causal parts of the Green's functions computed with data recorded in October 2014 have the highest signal-to-noise ratio and are the ones presented herein. Vertical-to-vertical (Z-Z) Green's functions using TK4OBS as the virtual source are shown in Figure 2.2a, and Z-Z, radial-to-radial (R-R), and transverse-to-transverse (T-T) Green's functions using TT5OBS as the virtual source are shown in Figures 2.2b–d, respectively. All the waveforms are bandpass filtered between 5 and 8 s using a Butterworth filter with four poles and two passes.

For the Z-Z component (Figures 2.2a and 2.2b), clear signals arrive with a group velocity of ~2.7 km/s at both causal and anticausal deconvolution lags. Long-period peak ground velocities (PGVs) of both anticausal and causal parts are nearly the same but strong asymmetries of signal duration are observed. The relatively slow group velocity of the surface-to-surface Green's functions can be explained by the low S-wave velocity of 1 km/s in the ~5.5 km thick accretionary prism located immediately beneath the virtual sources (*Koketsu et al.*, 2008).

For horizontal components, the wave propagation is not as clear as for the vertical component. Strong asymmetries of signal duration and large PGV differences can be observed between anticausal and causal deconvolution lags of both R-R and T-T com-

ponents in Figures 2.2c and 2.2d. For the R-R component, the group velocity can be determined from the anticausal part of the signal, as well as from the causal part for most of the stations despite the weaker amplitude. As shown in Figure 2.2e, the R-R group velocity is slightly faster than for the Z-Z component. Moreover, the plot of Z-Z versus R-R components in Figure 2.2f shows retrograde elliptical particle motion, suggesting that Rayleigh waves can be extracted from the offshore-onshore ambient seismic field. Finally, the group velocity of the T-T component is much slower than that observed for the other components in the 5 to 8 s period range. We also show in Figure 2.3 that clear wave propagation with a velocity of 3 km/s can be observed at longer periods (7–10 s) for the T-T component. Therefore, the low velocity observed in the 5 to 8 s period range can be interpreted as the dispersion effect of the Love waves.

In the following, we only consider the Z-Z component of the Green's functions for which clear wave propagation can be observed on both causal and anticausal deconvolution lags even at large distances. Moreover, as strong signal duration asymmetries can be observed between anticausal and causal parts, we select only the causal parts of the signals that correspond to wave propagation from the offshore virtual source to the onshore receivers.

2.3 Long-Period Ground Motion Simulation of a M_w 5.0 Subduction Earthquake

To validate the use of the offshore-onshore ambient seismic field as an alternative method to simulate the ground motion generated by subduction earthquakes, we compare the extracted Z-Z Green's functions to the vertical records of the previously described M_w 5.0 earthquake in the 5 to 8 s period range. As the earthquake hypocenter and the virtual source (TK4OBS) are not exactly colocated, we first need to account for the difference

in location to retrieve coherent phases between Green's functions and earthquake records. To do so, we apply a time-shift to the earthquake records that corresponds to the difference between the TK4OBS-receiver and hypocenter-receiver distances, divided by a theoretical surface wave velocity that is set to 2.5 km/s. However, this time-shift does not allow the recovery of coherent phases due to the slow group velocity in the accretionary prism of the surface-to-surface Green's functions, as explained previously, and uncertainties on the earthquake location. On the other hand, seismic waves generated by the earthquake, which occurred at a depth of 11 km, are less affected by this low-velocity layer. We finally apply a 3 s delay to the earthquake records as a first-order correction for the effect of the accretionary prism and the uncertainties about the earthquake location to retrieve coherent phases.

To compare quantitatively the phase difference between Green's function waveforms and earthquake records at each station, we compute the normalized correlation coefficients (CC) in the time domain between 2.5% and 92.5% of the cumulative energy of both signals (sum of the time series values squared), as done by *Denolle et al.* (2013) and *Viens et al.* (2014). We finally account for the different sources of uncertainty (e.g., excitation depth using a velocity model and the focal mechanism of the event, earthquake location, and occurrence time) pointed out by *Denolle et al.* (2013) by allowing a free phase shift of 2 s to the earthquake occurrence time to maximize the correlation coefficient.

Finally, the deconvolution method allows retrieval only of the relative, rather than the absolute, amplitude of the Green's functions. Therefore, Green's function amplitudes must always be calibrated when comparing with earthquake records. We follow *Viens et al.* (2014) to compute one calibration factor common to all the stations located in the direction of the Nobi basin, where Nagoya city is located. To compare Green's function and earthquake amplitudes for each station, we compute the PGV difference (PGV_{diff}) in percent as

$$PGV_{diff} = \frac{|PGV_G - PGV_{eq}|}{PGV_{max}} \times 100, \tag{2.2}$$

where PGV_G and PGV_{eq} are the PGVs of the calibrated Green's function and earthquake record, respectively. PGV_{max} is the largest PGV of the two waveforms.

Calibrated Z-Z Green's function waveforms and vertical velocity records of the M_w 5.0 earthquake are shown in Figure 2.4b. In the 5 to 8 s period range, high-correlation coefficients (≥0.8) for most of the stations suggest that earthquake ground motions can be accurately simulated by the Green's functions. Moreover, PGV differences are less than 50% for all the considered stations, indicating that the attenuation of amplitude with distance caused by geometrical spreading is also well retrieved by the Green's functions, despite slightly different propagation paths. Finally, several findings can be obtained. First, small PGV_G and PGV_{eq} values are observed at N.ANJH, N.HMAH, and N.KYSH stations, which are located in the Nobi basin, when compared to the PGVs recorded by surrounding stations. This feature can be explained by the location of the sensors in deep boreholes that reach the basement of the basin. Therefore, the ground motions recorded at these stations are not amplified by basin effects. Second, a local amplification likely to be related to the basin effect can be observed at N.MCTH station, which is located in a 100 m depth borehole in the Nobi basin. Indeed, PGV_G and PGV_{eq} values observed at this station, respectively, equal to 5.98×10^{-3} and 5.38×10^{-3} cm/s, are slightly larger than the PGVs recorded at closer distances from the virtual source by N.ATMH, N.ABNH, and N.HAZH stations. Third, the group wave velocity for the stations located on the western edge of the Nobi basin (e.g., EIGENJ, N.TAGH, and N.KIDH) is lower than that for the other stations and is likely to be related to propagation of the seismic waves through the sedimentary basin, as observed by *Hayashida et al.* (2014).

2.4 Distribution of 5% Damped Pseudovelocity Response at Different Periods

Velocity response spectra, which were introduced by *Biot* (1933) and *Housner* (1959), are peak amplitudes of velocity motions of single-degree-of-freedom systems with various natural frequencies responding to earthquake ground motions, for a given level of damping. As many large-scale structures behave as simple oscillators, the velocity response spectra of the long-period ground motion can be directly related to building design and development of building codes. In the following, we first calibrate the amplitude of the Green's functions for all the stations shown in Figure 2.6a and differentiate once the calibrated Green's functions and the earthquake records to retrieve the corresponding accelerations. We finally compute the pseudovelocity response spectra, which are the division of the acceleration response spectra by the natural angular frequencies, to avoid numerical problems that may arise from the integration of acceleration into velocity.

As observed by several authors (*Stehly et al.*, 2006; *Gerstoft and Tanimoto*, 2007), the sources of the ambient seismic field are not uniformly distributed with respect to azimuth and affect the amplitude retrieval. For first-order correction of this azimuthal pattern, we first correct the pseudovelocity response spectra for the surface wave geometrical spreading ($1/\sqrt{r}$), where r is the distance between seismic stations. We plot the results for a period of 6 s and 5% damping as a function of the azimuth, fit the data with a 4th-degree polynomial, and minimize the misfit between the polynomial and the arithmetic mean of the data (Figure 2.5a). Distributions of the pseudovelocity response at a period of 6 s before and after application of this correction are shown in Figures 2.5b and 2.5c. The amplification effect observed at stations located perpendicularly to the coast, which is caused by a seismic field coming mainly from the Pacific Ocean, is considerably reduced by our first-order correction.

Distributions of the 5% damped pseudovelocity response at periods of 6 s for the M_w 5.0 earthquake records and the calibrated Green's functions corrected for the azimuthal pattern are shown in Figures 2.6a and 2.6b. The same maps for a period of 7 s are shown in Figures 2.7a and 2.7b. In both cases, the maximum amplification is observed in the Omaezaki region, where amplification of the long-period ground motions was reported for the 2004 M_w 7.4 off the Kii Peninsula earthquake (*Miyake and Koketsu*, 2005). Such amplification can be explained by a 4–5 km-thick layer of low *S* wave velocity (1–2 km/s) that overlaps the bedrock in this area, as revealed by *Tsuno et al.* (2003). One can also note that the earthquake amplification in the Omaezaki region and in the direction of the Nobi basin is larger than the one of the Green's functions. This pattern is probably related to a focal mechanism effect of the earthquake that has a theoretical two-lobed Rayleigh wave pattern having the similar azimuth at 6 s (not shown here). Local amplifications that can be observed for the Green's functions in Figure 2.6b, but not for the earthquake, may be caused by the complex anisotropic distribution of the ambient seismic field sources, which is not fully taken into account by the first-order correction that we applied to the Green's functions. Finally, unlike *Miyake and Koketsu* (2005) for the 2004 M_w 7.4 off the Kii Peninsula earthquake, we did not observe any large-peak response spectra at long periods in the Nobi basin. Such feature is probably due to the moderate size of the earthquake, which was not sufficient to generate surface waves with enough energy to propagate over large distances, and the fact that most of the stations in the basin are located in deep boreholes.

2.5 Conclusions

We successfully extracted the surface-to-surface Green's functions between offshore and onshore seismic stations in the Tokai/Tonankai area and showed that Rayleigh waves with

elliptical retrograde particle motions as well as dispersive Love waves can be retrieved in the 5 to 8 s period range.

After taking into account that the earthquake hypocenter and the virtual source are not colocated, we obtained good agreement between the phases of Z-Z Green's functions and vertical earthquake records in the 5 to 8 s period range for stations located in direction of the Nobi basin. Moreover, only small PGV differences are observed, and the geometrical amplitude decay is well retrieved after the computation of the calibration factor for the considered stations. Such results validate the use of the offshore-onshore seismic field to simulate the ground motions of moderate subduction earthquakes in a period range, which is, however, shorter than for onland-onland simulations (4–10 s).

We finally computed the pseudovelocity response spectra for the earthquake records and the calibrated Green's functions that we corrected for the anisotropic distribution of the ambient seismic field sources and showed that they both have maximum values in the Omaezaki area. As only surface-to-surface Green's functions were computed in this study, we have not yet recovered the amplifications caused by the focal mechanism effect. Nevertheless, this technique, coupled with physics-based methods and GMPEs, could be a powerful tool to assess seismic hazards related to offshore subduction earthquakes.

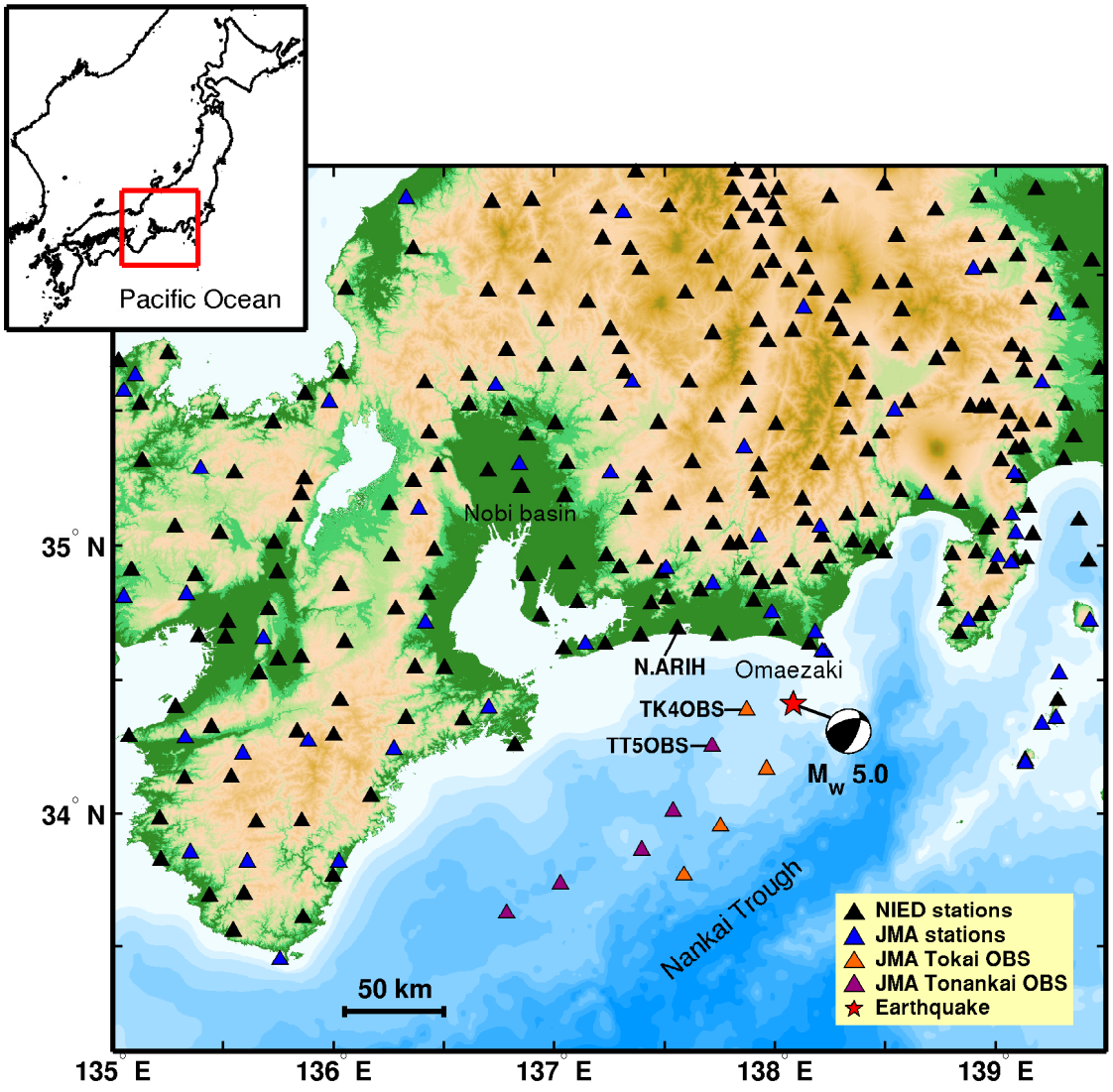

Figure 2.1: Map of the Tokai/Tonankai area, including Hi-net stations (black triangles), stations of the Japan Meteorological Agency (blue triangles), and the Tokai and Tonankai cable OBS systems that were deployed in 1979 (orange triangles) and 2008 (purple triangles), respectively. The location of the M_w 5.0 earthquake is indicated by the red star.

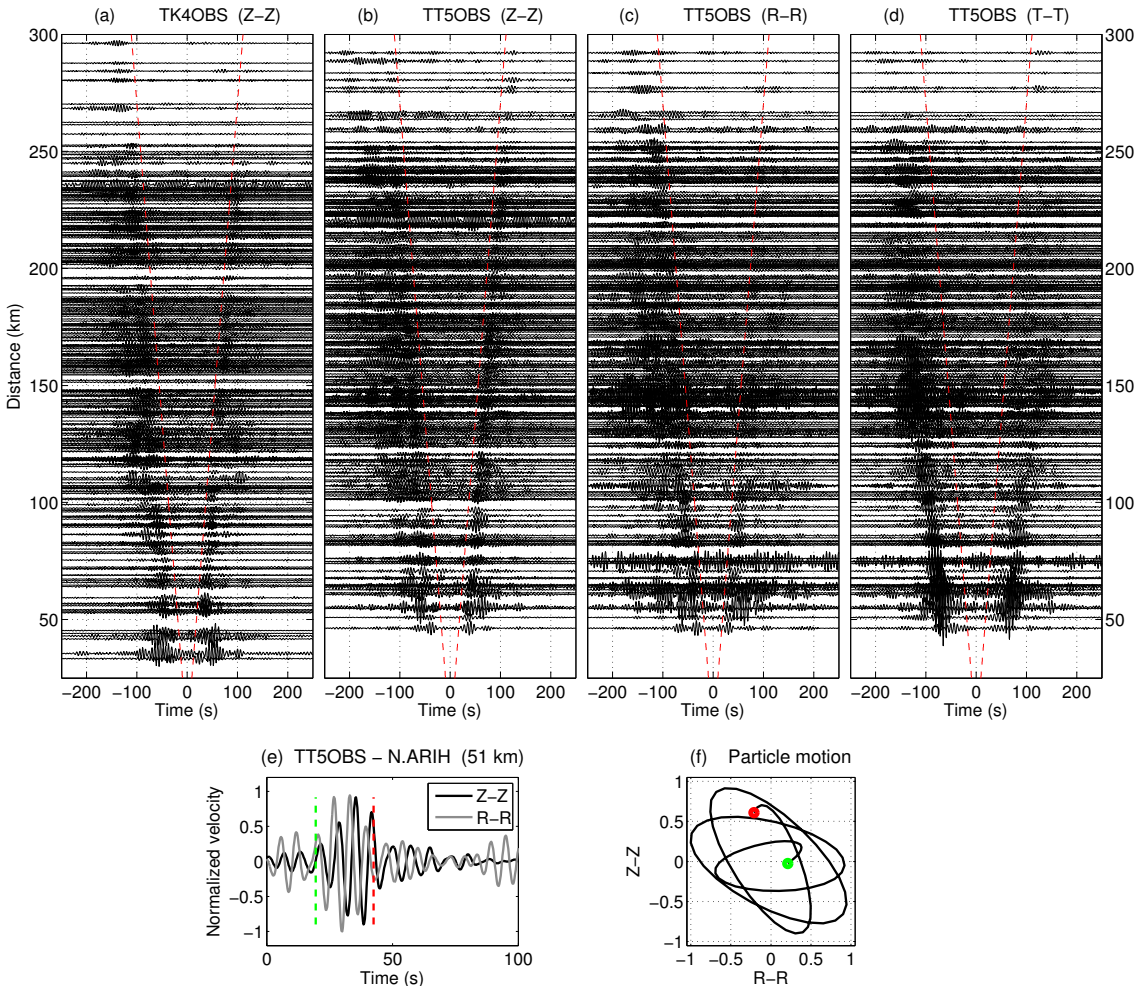

Figure 2.2: (a) Vertical-to-vertical (Z-Z) ambient noise Green's functions using TK4OBS as the virtual source. Z-Z, radial-to-radial (R-R), and transverse-to-transverse (T-T) ambient noise Green's functions using TT5OBS as the virtual source are shown in (b), (c), and (d) as a function of the distance from the virtual source. All the waveforms have been bandpass filtered between 5 and 8 s and the ambient noise Green's functions shown in Figures 2.2b–2.2d have amplitudes twice as large as those extracted using TK4OBS in (a). Red dashed lines represent the wave propagation speed of 2.7 km/s. (e) Z-Z and R-R ambient noise Green's functions normalized to the maximum value of the R-R component between stations TT5OBS and N.ARIH. (f) Particle motion plot of the Z-Z versus R-R components computed between the green and the red dashed lines shown in Figure 2.2e.

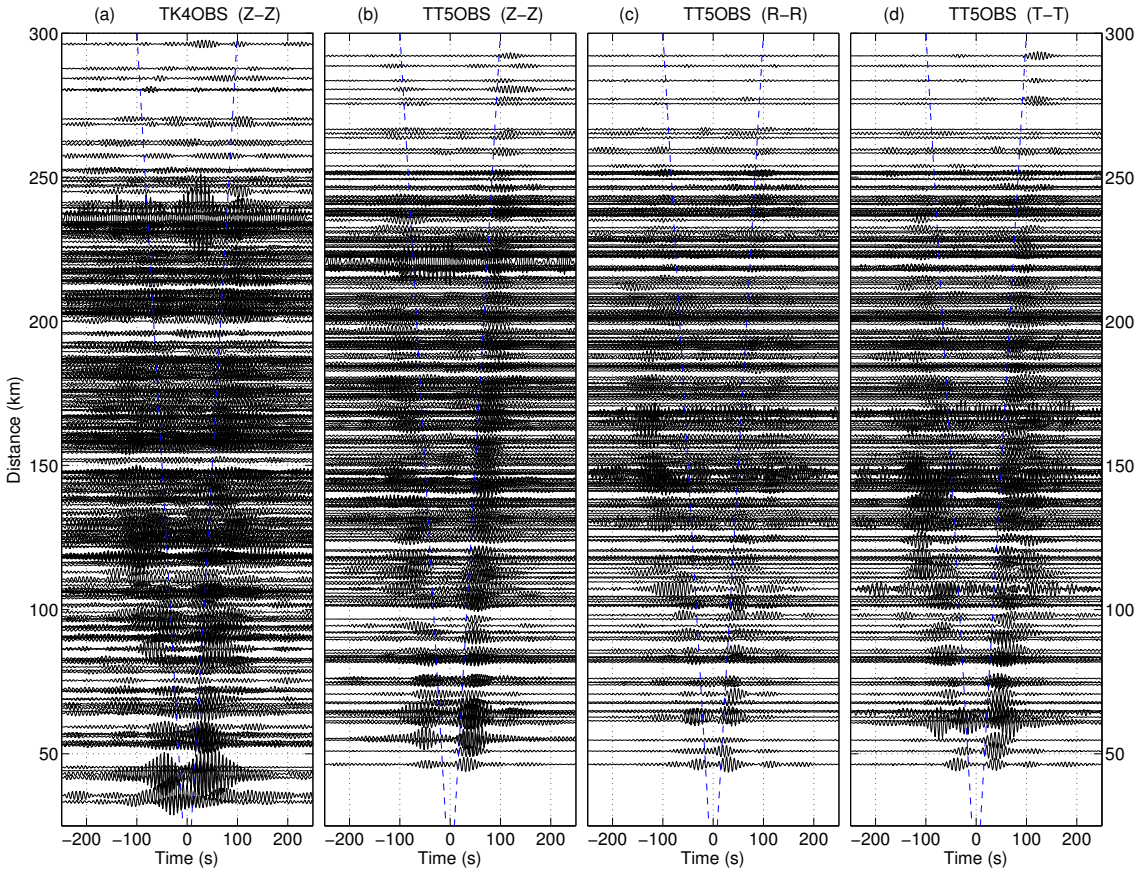

Figure 2.3: (a) Vertical-to-vertical (Z-Z) ambient noise Green's functions using TK4OBS as the virtual source. Z-Z, radial-to-radial (R-R), and transverse-to-transverse (T-T) ambient noise Green's functions using TT5OBS as the virtual source are shown in (b), (c), and (d) as a function of the distance from the virtual source. All the waveforms have been bandpass filtered between 7 and 10 s. Blue dashed lines represent the 3.0 km/s wave velocity.

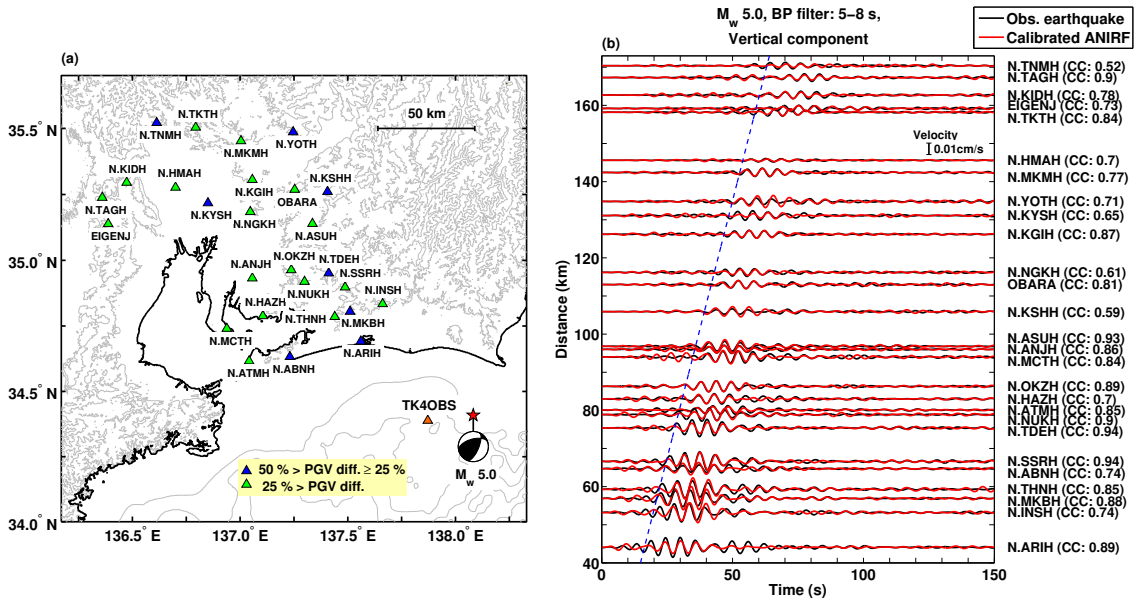

Figure 2.4: Simulation of long-period ground motions at (a) stations in the Nobi basin and surrounding area (triangles) for a M_w 5.0 earthquake (star). The color of the triangles on the map indicates the percentage difference between the PGVs of the extracted ambient noise Green's functions and the earthquake records computed using equation (2.2). (b) Calibrated ambient noise Green's functions (red lines) and earthquake records (black lines), bandpass filtered between 5 and 8 s in velocity for vertical components, are shown as a function of the distance from the virtual source (TK4OBS). The blue dashed line represents the wave propagation speed of 2.7 km/s and correlation coefficients (CC) are given in parentheses.

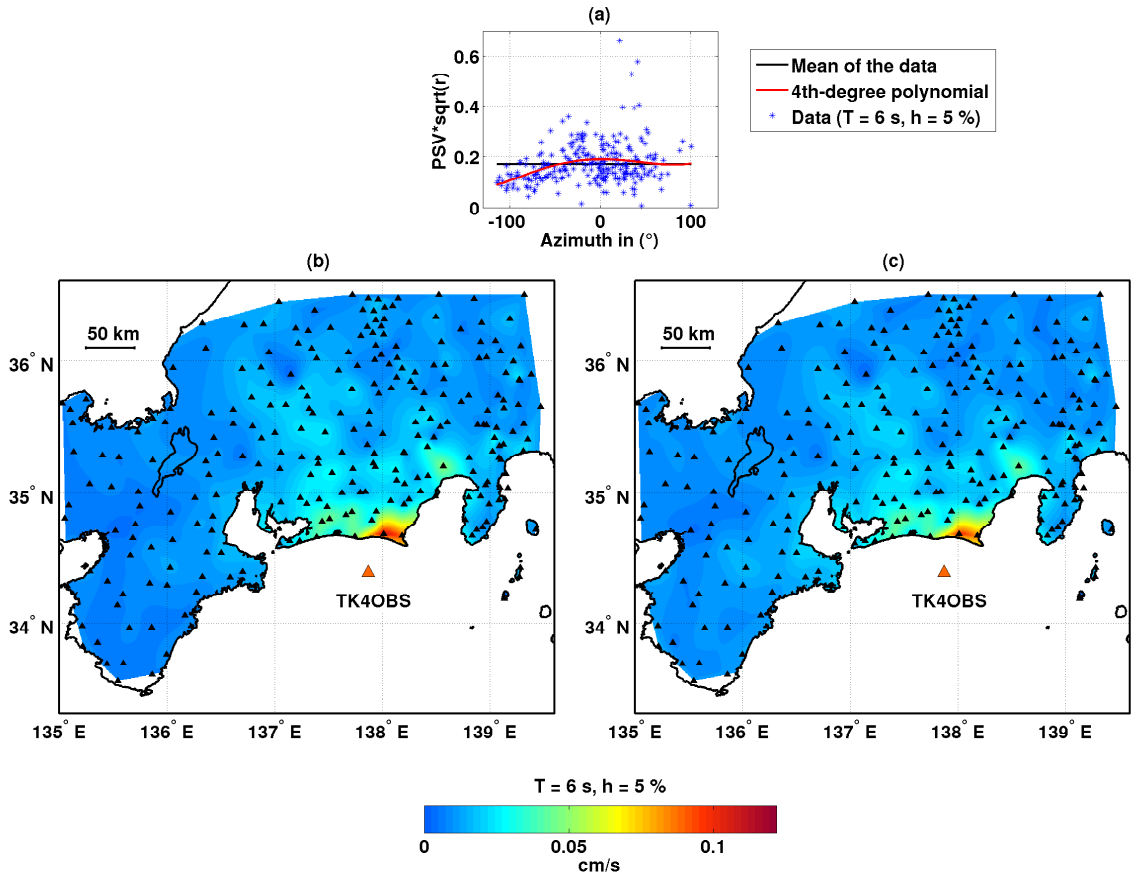

Figure 2.5: (a) Values of 5% damped pseudo-velocity response at a period of 6 s corrected for the geometrical spreading as a function of the azimuth are shown by blue stars, and the 4th-degree polynomial that fitted the data and the arithmetic mean are shown by the red and black curves, respectively. Distributions of 5% damped pseudo-velocity response at a period of 6 s computed using the amplitude calibrated Green's functions (b) before and (c) after applying the correction of the anisotropic distribution of the ambient seismic field sources.

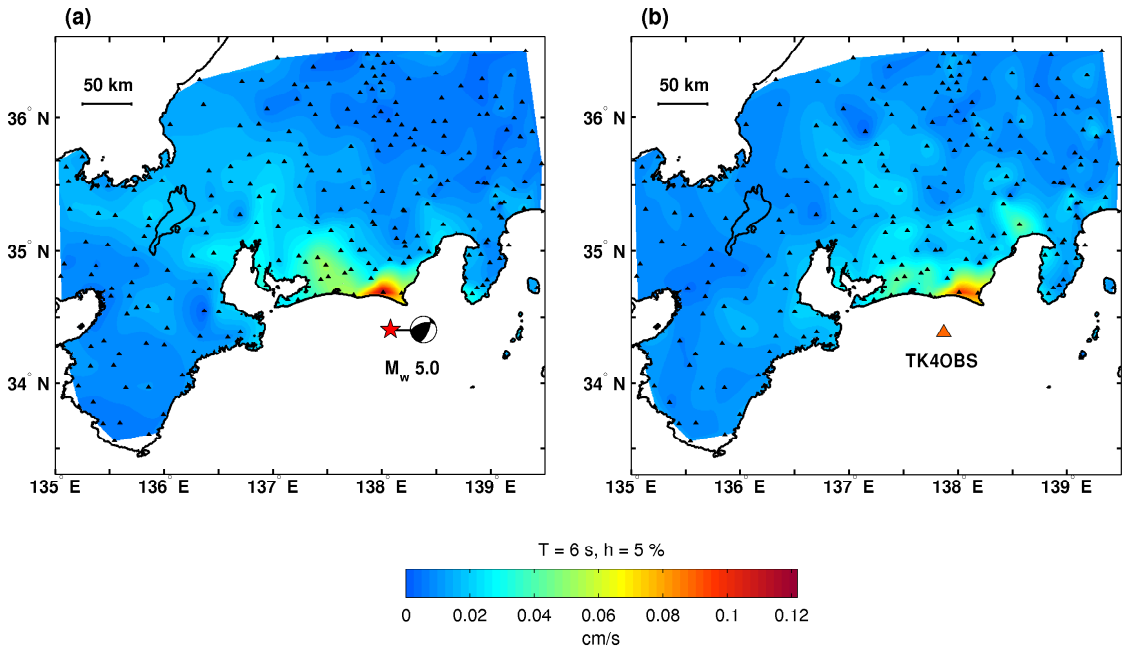

Figure 2.6: Five percent damped pseudovelocity response at a period of 6 s computed using (a) records of the M_w 5.0 earthquake and (b) ambient noise Green's functions after calibration of the amplitude and correction of the anisotropic distribution of the ambient seismic field sources.

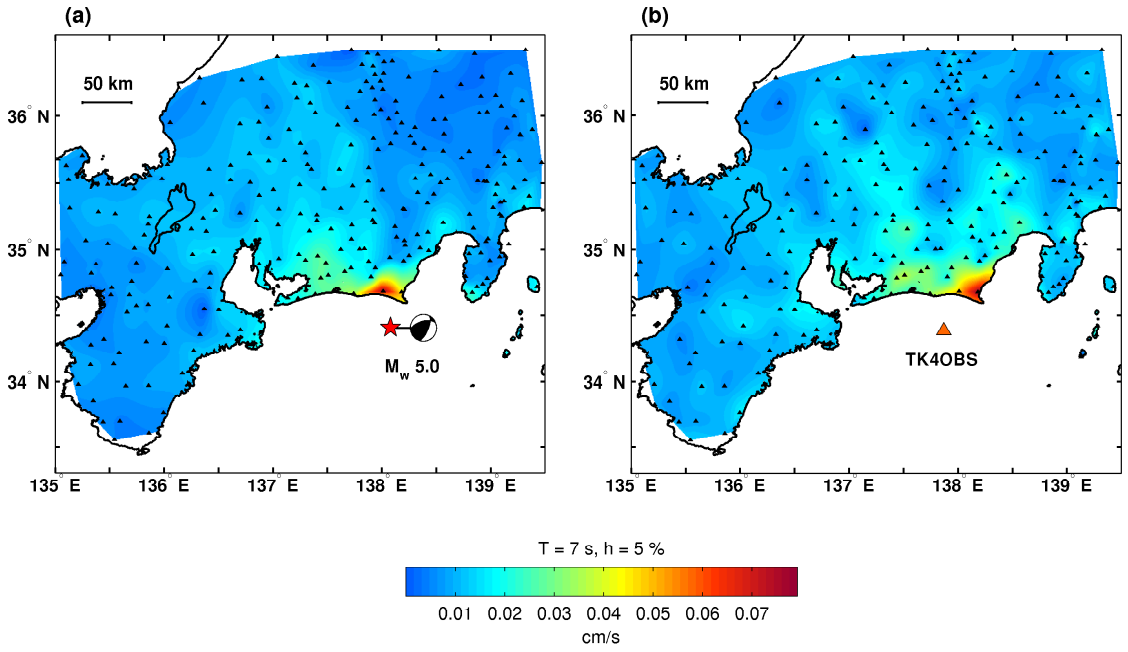

Figure 2.7: Same as Figure 2.6 at a period of 7 s.

Chapter 3

Basin-Scale Green's Functions from the Ambient Seismic Field Recorded by MeSO-net Stations

This chapter has been slightly modified from Viens, L., K. Koketsu, H. Miyake, S. Sakai, and S. Nakagawa (2016), Basin-scale Green's functions from the ambient seismic field recorded by MeSO-net stations, *Journal of Geophysical Research: Solid Earth*, 121, 2507–2520, doi:10.1002/2016JB012796.

3.1 Introduction

Seismic waves generated by earthquakes can be significantly affected by the near-surface seismic velocity structure of the Earth. Sedimentary basins, which lie beneath a majority of metropolitan areas including Los Angeles and Tokyo, have the potential to trap and strongly amplify earthquake ground motions. Significant damage on large-scale structures, including high-rise buildings and oil storage tanks, caused by such phenomena were observed even hundreds of kilometers away from the hypocenter during the large 1985

Michoacán (*Anderson et al.*, 1986; *Beck and Hall*, 1986) and 2003 Tokachi-oki (*Koketsu et al.*, 2005) earthquakes.

The Kanto sedimentary basin, which lies beneath the Tokyo metropolitan area, is a large-scale basin that spreads over 17,000 km^2. It is bounded by mountains on the western and northern sides and by the Pacific Ocean on the southern and eastern sides (Figure 3.1a). This basin, which is locally deeper than 4 km, is shown in Figure 3.1b, where the V_s = 3.2 km/s isosurface taken from the Japan Integrated Velocity Structure Model (JIVSM) is used as a proxy of basin depth (*Koketsu et al.*, 2008, 2012). This model decomposes the Kanto basin into three layers that have *S* wave velocities equal to 0.5, 0.9, and 1.5 km/s from top to bottom (*Koketsu et al.*, 2009). The deepest layer of the basin lies on the bedrock that has a *S* wave velocity equal to 3.2 km/s.

The effect of the complex shape of the Kanto basin on seismic waves has been observed during several earthquakes. Initially, *Kudo* (1978, 1980), followed by the study of *Mamula et al.* (1984), identified that the Kanto basin has a resonance period of 7–10 s. Together with the reflection survey by *Koketsu and Higashi* (1992), the geological survey by *Suzuki* (1996, 1999), and the microtremor survey by *Yamanaka and Yamada* (2002, 2006), the shape of the Kanto basin and that of the shallow layers were determined. Using dense strong motion networks, *Koketsu and Kikuchi* (2000) and *Furumura and Hayakawa* (2007) discovered the surface wave propagation characteristics in the Kanto basin. The resonance period of the Kanto basin is mainly controlled by the basin depth. However, the shallow layers also influence the amplification and the dominant period. Recently, *Yoshimoto and Takemura* (2014) reported that the predominant period of the long-period waves generated by several moderate-to-large earthquakes is around 7 s for basin-bedrock interfaces with depths exceeding 2 km. Such long-period resonance of the basin has direct implications for the numerous tall buildings of the Tokyo metropolitan area that have similar natural periods.

The Metropolitan Seismic Observation network (MeSO-net) was deployed between 2007 and 2011 to assess the associated seismic hazard in the seismically highly active and densely populated Kanto basin (*Kasahara et al.*, 2009; *Sakai and Hirata*, 2009). This network is composed of approximately 300 accelerometer sensors buried in boreholes that are approximately 20 m deep. In addition to this network, approximately 120 short-period velocity seismometers, which are a part of the Hi-net of the National Research Institute for Earth Science and Disaster Prevention (NIED) (*Okada et al.*, 2004; *Obara et al.*, 2005), Japan Meteorological Agency (JMA), and University of Tokyo networks, were deployed in the basin and its surroundings (Figure 3.1a). All of these seismic stations record continuous data.

Over the last decade, new opportunities in seismology have emerged through the use of the ambient seismic field, which is continuously recorded by seismic networks. Careful processing of this ambient seismic field enables the extraction of the Green's function between a pair of stations. This technique, called seismic interferometry, was previously applied for seismic hazard assessment purposes. Examples include the prediction of the long-period (≥4 s) seismic waves generated by moderate M_w 4–5 class crustal earthquakes (*Prieto and Beroza*, 2008; *Denolle et al.*, 2013; *Viens et al.*, 2014), a moderate M_w 5.0 subduction event (*Viens et al.*, 2015), and large M_w 7 class crustal finite source models (*Denolle et al.*, 2014a), without any knowledge of the velocity structure. Seismic interferometry has also been used to characterize wave amplification at the basin and local scales. *Savage et al.* (2013) extracted Green's functions between stations located in the Canterbury basin of New Zealand and used horizontal-to-vertical amplitude ratio of the first higher-mode Rayleigh waves to determine the basement resonance period. *Denolle et al.* (2014b) studied the seismic wave amplification in the Kanto basin using Hi-net stations located outside the basin as virtual sources, and MeSO-net stations as receivers. They concluded that the basin amplification is strongly affected by the azimuthal

variations of the seismic waves entering into the basin. Using the 5200 geophone array deployed over a few square kilometers in Long Beach, California, *Bowden et al.* (2015) computed high-resolution maps of site amplification at frequencies of 0.67, 1.0, and 2.0 Hz.

In this study, we extract vertical-to-vertical Green's functions from the ambient seismic field in the Kanto basin using two stations as the virtual sources. These stations are the TENNOD (JMA) and N.ITOH (NIED) stations and are located on the eastern and southern edges of the basin, respectively (Figure 3.1b). These virtual sources were chosen to compare the extracted Green's functions to the waveforms of two earthquakes of M_w 5.8 and M_w 4.9 (Table 3.1) that occurred in their vicinity. Figure 3.1a shows the location of these events, which occurred with normal faulting and strike-slip faulting mechanisms (F-net of NIED centroid moment tensor solution). These two earthquakes are some of the largest shallow events (depth < 15 km) that occurred in the proximity of the basin and are more likely to have generated long-period ground motions. Moreover, seismic waves generated by these events arrive with two different azimuths in the basin, which allow us to examine in more details the effect of the shape of the Kanto basin on the wave propagation.

We first show that Green's functions extracted between seismic stations aligned along straight lines contain several groups of seismic waves traveling with different velocities. We further investigate the characteristics of these waves using time-frequency analysis and compare them to synthetic Green's functions in order to demonstrate their sensitivity to the different layers that compose the basin. We also find that after amplitude calibration, the Green's function waveforms agree well with the earthquake records in different period ranges. Finally, we present the distribution of the 5% damped pseudovelocity response at a period of 6 s computed from the records of each event and the calibrated Green's functions, followed by a discussion.

3.2 Basin-Scale Green's Functions From the Ambient Seismic Field

Vertical-to-vertical (Z-Z) Green's functions are extracted from the ambient seismic field recorded at two seismic stations using the deconvolution method as

$$\widehat{G}_{ZZ}(x_r, x_s, \omega) = \left\langle \frac{\hat{u}_Z(x_r, \omega)\hat{u}_Z^*(x_s, \omega)}{\{|\hat{u}_Z(x_s, \omega)|\}^2 + \xi} \right\rangle. \tag{3.1}$$

$\hat{u}_Z(x_s, \omega)$ and $\hat{u}_Z(x_r, \omega)$ are Fourier-transformed 1 h velocity time series at the virtual source and the receiver station, respectively. To prevent the denominator term from reaching zero and create an unstable equation, we smooth the virtual source spectrum (20-point running average), which is represented by the operator $\{\}$. ξ is a water level that is set to 1% of the average spectral power as done by *Viens et al.* (2015). We finally stacked the 1 h deconvolutions over 1 month, denoted by $\langle\rangle$, and computed the inverse Fourier transform of $\widehat{G}_{ZZ}(x_r, x_s, \omega)$ to recover the anticausal (negative lag) and causal (positive lag) parts of the Green's functions in the time domain.

We extract Green's functions between the virtual sources and all the stations located inside the basin and its surroundings from the ambient seismic field recorded in October 2014. In the Kanto basin, the predominant source of ambient seismic field is the Pacific Ocean. Since the virtual sources are located close to the ocean, the anticausal and causal parts of the Green's functions can be strongly asymmetric. In the following sections, we only focus on the causal part that contains most of the energy because of the virtual source locations close to the coast.

The great advantage of MeSO-net is to have seismometers that are aligned along straight lines. Such lines of receivers allow to study the different characteristics of the seismic waves propagating away from the virtual sources through the Kanto sedimentary basin. Moreover, the effect of an eventual nonhomogeneous distribution of the ambient

seismic field sources on the extracted Green's functions should be reduced as the virtual source and all the receiver stations are aligned along the same direction. We select two lines of receivers, called Lines 1 and 2, which are aligned with the TENNOD and N.ITOH stations, respectively (Figure 3.1b). We extract the *S* wave velocity profiles below these two lines from the JIVSM, filter the Green's functions in different period bands using a four-pole and two-pass Butterworth filter, and show the results for Lines 1 and 2 in Figures 3.2 and 3.3, respectively. To observe the seismic wave propagation across the basin, even at long distances, Green's functions are corrected for the geometrical spreading of surface waves as done by *Denolle et al.* (2014b) and *Viens et al.* (2015). Moreover, we taper the Green's functions to smooth the beginning of the signals.

For Line 1, three groups of waves traveling with different velocities are observed in the period range of 1 to 10 s for distances between the virtual source and the receivers shorter than 100 km (Figure 3.2b). By filtering the Green's functions in the period range of 1 to 3 s (Figure 3.2c), only dispersive waves traveling with a low group velocity of 0.35 km/s are recovered. The two other groups of arrivals, which include dispersive waves traveling with a group velocity of 0.7 km/s and nondispersive waves propagating with a velocity of 3 km/s, are clearly observed in the period range of 3 to 10 s (Figure 3.2d).

The seismic wave propagation along Line 2 is quite different from the one along Line 1. In the period ranges of 1 to 10 s and 3 to 10 s (Figures 3.3b and 3.3d), a clear propagation of seismic waves is observed. These seismic waves propagate with a group velocity of around 3 km/s and are clearly amplified at a distance of approximately 65 km away from the virtual source. This amplification is also observed in the period range of 1 to 3 s despite the fact that no clear wave propagation is observed.

3.3 Characteristics of Basin-Scale Green's Functions

To further investigate the characteristics of the waves propagating through the Kanto basin, we perform time-frequency analysis of Green's functions using the *S* transform (*Stockwell et al.*, 1996). The *S* transform allows computing high-resolution frequency content as a function of time and is defined as

$$G_{zz}(t,f) = \int_{-\infty}^{+\infty} G_{zz}(\tau) \frac{|f|}{\sqrt{2\pi}} e^{-\frac{(t-\tau)^2 f^2}{2}} e^{-i2\pi f\tau} \mathrm{d}\tau, \tag{3.2}$$

where G_{zz} is the vertical-to-vertical Green's function, f is the frequency, and t is the time.

3.3.1 Wave Propagation From the Eastern Part of the Basin: Line 1

We focus on 15 stations that are aligned along Line 1 and located between 18 and 62 km away from the TENNOD station (Figure 3.4a). A clear dispersion of the waves traveling with velocities of 0.35 and 0.7 km/s can be observed in the normalized *S* transforms in Figure 3.4b. This dispersion effect suggests the recovery of Rayleigh waves. We also observe in this time-frequency analysis the propagation of nondispersive waves at frequencies around 0.1 Hz. To confirm the nondispersive character of these waves traveling with a group velocity of approximately 3 km/s, we show the envelope of the Green's functions filtered in very narrow frequency bands for two stations (Figure 3.4c). Each envelope is normalized with respect to its maximum amplitude. This filtering shows the nondispersive waves at frequencies lower than 0.2 Hz and the dispersion of Rayleigh waves at higher frequencies. It suggests that these nondispersive waves, which were also observed by *Denolle* (2014), are the *S* waves propagating through the Kanto basin.

The time-frequency analysis also shows that the frequency content of the Green's functions strongly varies with distance to the virtual source. For interstation distances shorter than 30 km, a clear signal can be recovered up to 0.8 Hz. This upper frequency

limit decreases to approximately 0.5 Hz for larger interstation distances. Furthermore, the amplitude gradually increases with distance at frequencies below 0.2 Hz. This feature is likely to be related to the fact that the low-frequency waves need dozens of kilometers to develop and be observed in the Green's functions.

To study in more details the characteristics of the extracted Rayleigh waves, we generate synthetic Green's functions for a simple 1-D velocity profile (Figure 3.5a) using the normal mode summation module of *Herrmann and Ammon* (2002). The simplified velocity profile is similar to the one extracted from the JIVSM below these stations (Figure 3.5b), and the synthetic Green's functions only include the fundamental mode of Rayleigh waves. Synthetic and extracted Green's functions are shown in Figures 3.5c and 3.5d, respectively. Despite the simple velocity model used for the computation of the synthetics, a good agreement between seismic wave arrivals is observed. One can note that the amplitude of the waves propagating with a group velocity of 0.35 km/s is larger than the one propagating with a group velocity of 0.7 km/s for the synthetic Green's functions. This feature is likely to be related to the fact that the simple 1-D velocity model does not account for the shape of the basin edge.

We measure the group velocities of Rayleigh waves on the Green's function extracted between the TENNOD and E.HSDM stations. We show these group velocity measurements together with the theoretical dispersion curve of the fundamental mode Rayleigh waves in Figure 3.6a. We also present the theoretical dispersion curve of the first higher-mode of Rayleigh waves, if used for the computation of the synthetics, in this figure. The measured group velocities agree well with the theoretical dispersion curve of the fundamental mode of Rayleigh waves. Such a similarity indicates that only the fundamental mode is recovered on the Z-Z component for the stations located along Line 1 in the vicinity of the basin edge. Similar results were observed by *Savage et al.* (2013) for the Canterbury basin of New Zealand, where only the fundamental mode of Rayleigh waves

is recovered on the Z-Z component, whereas the fundamental and first higher modes are observed on the R-R component. Our results also emphasize the effect of the basin depth on the recovery of higher modes of Rayleigh waves on the Z-Z component, which have been recently observed by *Boué et al.* (2016) between pairs of stations located atop the deepest part of the Kanto basin.

To explain the two distinct group arrivals of Rayleigh waves, we compute the eigenfunctions of the Rayleigh wave fundamental mode derived from the 1-D velocity profile (Figure 3.6b). Figures 3.6c and 3.6d show the synthetic Green's function computed for a distance of 40.5 km and the corresponding extracted Green's function, respectively. Despite the simple velocity profile used for the computation of the synthetic Green's functions, the different groups of arrivals agree with the ones associated with our extracted Green's functions. Using ray tracing, we find that the S waves arrive at the receiver stations after traveling through the basement of the basin. We also conclude from the dispersion curve and the eigenfunctions (Figures 3.6a and 3.6c) that the fundamental mode of Rayleigh waves is sensitive to the shallowest layer of the basin at short periods (1–3 s) and to deeper layers at longer periods (3–10 s). This sensitivity to the first layer of the basin causes the large dispersion and the two groups of arrivals observed in Figure 3.2.

3.3.2 Wave Propagation From the Southern Part of the Basin: Line 2

We show the time-frequency analysis for 15 stations aligned along Line 2 in Figure 3.7. The propagation of seismic waves from the N.ITOH station, which is located outside the basin, to stations situated atop a basin depth that reaches 3 km, is different from the one observed for Line 1. The propagation of dispersed Rayleigh waves is observed despite a level of noise larger than that in Figure 3.4. The poorer quality of the Green's

functions might be explained by the location of the Sagami Bay between the virtual source and the receiver stations, which can create new sources of wave energy that violates the assumption of distant and dispersive ambient seismic field sources. Moreover, the late part of Rayleigh waves, which is sensitive to the first layer of the basin, and the *S* wave arrivals are not recovered. This feature might be related to the propagation of the waves through the thick accretionary prism of the Sagami Trough that low-pass filters the seismic waves before entering into the Kanto basin.

3.4 Earthquake Ground Motion Simulation using Basin-Scale Green's Functions

The M_w 4.9 and M_w 5.8 earthquakes have been well recorded by dense networks deployed in the Kanto basin. We show that the surface-to-surface Green's functions can be used to accurately simulate the ground motions of these two shallow events after amplitude calibration and by accounting for the fact that the earthquake hypocenter do not coincide exactly with the virtual source, as done by *Viens et al.* (2014, 2015).

3.4.1 M_w 5.8 Earthquake Simulation

We compare the calibrated Green's function and earthquake waveforms filtered in the period ranges of 1 to 10 s, 1 to 3 s, and 3 to 10 s in Figure 3.8a. In these three period ranges, waveforms have similar maximum peak ground velocities and strong ground motion duration. The best fit between Green's functions and earthquake waveforms is observed in the period range of 3 to 10 s. In this period range, *S* wave arrivals and Rayleigh waves of the Green's functions agree well with those of the earthquake, despite different raypaths due to the hypocenter location at a depth of 11 km. The well-dispersed part of the fundamental mode of Rayleigh waves is also retrieved in the period range of 1 to 3 s. However,

a small overestimation of the long-period ground motion is observed for stations situated at distances shorter than 30 km from the virtual source. Moreover, seismic waves arriving between the first *S* wave arrivals and Rayleigh waves cannot be recovered in the simulations for the three period ranges. Therefore, while the ambient seismic field is a powerful method to simulate long-period (≥ 1 s) Rayleigh waves at distances larger than approximately 30 km, it is limited in its capability to accurately simulate ground motions at short distances and at periods of primary engineering interest (e.g., 0.1–1 s). Nevertheless, the coupling of this technique with high-frequency modeling allows to simulate broadband ground motions as demonstrated by *Viens et al.* (2014).

The exceptional station coverage is a good opportunity to study the distribution of ground motion parameters. We present the distribution of the 5% damped pseudovelocity response at a period of 6 s computed from the M_w 5.8 earthquake records and the calibrated Green's functions in Figures 3.8b and 3.8c, respectively. These two maps have similar amplification patterns, with a large amplification close to the deepest part of the Kanto basin. The shape of this area of large amplification is, however, slightly greater for the Green's functions. This feature is likely to be related to the nonuniform distribution of the ambient seismic field sources that might slightly amplify the long-period ground motions in a direction perpendicular to the coast. We discuss this point in more details in Section 3.5. We also show the 5% damped pseudovelocity response maps at periods of 4 and 8 s in Figure 3.9. For these two periods, maps computed from the simulated and recorded waveforms agree also well, despite the fact that the same amplitude overestimation pattern is observed in the simulations.

We also present the pseudovelocity response spectra for three stations located close to the deepest part of the basin (Figure 3.10). For these three stations, the pseudovelocity response spectra computed from observed and simulated waveforms agree well. For the three stations, the largest amplitude of the spectra is observed around 3 s. Moreover, the

amplitude of the simulated and observed spectra at 6–7 s increases with the depth of the basin.

3.4.2 M_w 4.9 Earthquake Simulation

Calibrated Green's functions are also in good agreement with seismic waves generated by the M_w 4.9 earthquake for the stations aligned along Line 2 (Figure 3.11a). In the period range of 3 to 10 s, Rayleigh waves generated by the earthquake are well simulated for stations located at less than approximately 90 km away from the virtual source. At farther distances, the duration and the maximum amplitude of the simulated ground motions are very similar to the observed ones despite the fact that only a few phases remain coherent. This feature is also observed in the period ranges of 1 to 10 s and 1 to 3 s.

This earthquake occurred in December 2009 while the MeSO-net stations were under deployment. We show the distribution of the 5% damped pseudovelocity response at a period of 6 s computed from the earthquake and the calibrated Green's functions using only the stations that recorded this event in Figures 3.11b and 3.11c, respectively. As for the M_w 5.8 earthquake, amplification patterns generated by this event are well simulated, despite a smaller excitation of the ground motions caused by the smaller magnitude of this earthquake. Note that the maximum amplification is located in the western part of the Tokyo Bay for this event.

3.5 Discussion

The amplitude of the extracted Green's functions can be affected by a nonuniform distribution of the ambient seismic field sources. Such feature has been observed by *Stehly et al.* (2006), *Gerstoft and Tanimoto* (2007), and *Denolle et al.* (2014a) in California, where the ambient seismic field is mainly derived from the Pacific Ocean in the period

range of 4 to 10 s. They found that Green's functions extracted between pair of stations having an azimuth perpendicular to the coast have the largest amplitudes. Therefore, *Denolle et al.* (2014a) corrected the amplitude of the Green's functions with a calibration factor that depends on the azimuth, prior to simulate the ground motions of large M_w 7 class earthquake scenarios in California. For the Kanto basin, *Denolle et al.* (2014b) showed that the wave amplification caused by the basin effect overcomes the amplitude variations that may arise from a non-uniform distribution of the ambient seismic field sources. Moreover, the receiver stations in the Kanto basin are mainly concentrated in a narrow azimuth range (e.g., $\leq 90°$) for the two simulated earthquakes, which should also reduce the bias of the amplitude variations with the azimuth. For these two reasons, we do not use calibration factors that depend on the azimuth to correct the amplitude of the Green's functions. This probably leads to the small overestimation observed for the simulations in Figures 3.8c and S1. However, the effect might be greater if the method is applied to other regions, such as California, or if the receiver stations are distributed over a broader azimuth range.

The dense networks deployed in the Kanto basin allow to simulate the spatial distribution of earthquake ground motion parameters at high resolution as shown in Figure 3.8 for the M_w 5.8 event. However, the M_w 4.9 earthquake has only been recorded by approximately half of the MeSO-net stations and the station coverage close to the deepest part of the Kanto basin, where the maximum amplification is observed for the M_w 5.8 event, is quite spare. Therefore, areas of well-amplified ground motions might be missing in the maps shown in Figures 3.11b and 3.11c. To estimate the effect of the sparse station distribution, we compute the same map using Green's functions from all the stations available in the Kanto basin. We compare the map shown in Figure 3.11c to this new map in Figure 3.12. While both maps show generally similar amplification patterns, several differences can be observed. First, the location of the maximum amplification area is

slightly larger and shifted to the east when all the stations are used. Second, the amplification in the Tokyo Bay is smaller in Figure 3.12b due to a larger number of stations that better constrain this amplification area. Finally, a small area of stronger amplification is observed close to the deepest part of the basin. The use of all the receiver stations allows to better constrain the amplification patterns shown in Figure 3.11c. It also predicts that no strong amplification occurred close to the deepest part of the basin as for the M_w 5.8 event. The difference of location of the maximum amplification area for these two earthquakes supports the observations of *Denolle et al.* (2014b) that showed that the seismic wave amplification in the Kanto basin is strongly affected by the azimuth variations of the incoming seismic waves.

The sparse station distribution might have a greater effect on the maps computed for the M_w 5.8 earthquake. Indeed, only a few stations that recorded the M_w 4.9 event are located close to the deepest part of the basin, where the strongest amplification is observed. This feature is likely to lead to an underestimation of the size of the large amplification area. Therefore, the exceptional station coverage in the Kanto basin allows to observe and simulate earthquake ground motion at high resolution. Needless to say that denser networks, such as the one deployed in Long Beach, California, would increase the spatial resolution of these predictions.

In this study, we focus on the simulation of the long-period vertical ground motion generated by earthquakes. However, it has been observed during past events that the vertical motion can be less sensitive to sedimentary basins than horizontal motions. For example, *Campillo et al.* (1989) and *Sánchez-Sesma et al.* (1993) showed that the long-period vertical ground motion generated by the 1985 Michoacán and 1989 Guerrero earthquakes, respectively, were not significantly affected by the Mexico sedimentary basin. On the other hand, horizontal motions were well amplified by the basin. A similar feature has been observed by *Kato et al.* (1993) in the Kanto basin during the M_w 6.7 Izu-hanto-

toho-oki earthquake which occurred in June 1980 close the N.ITOH virtual source. As earthquake engineering mostly focuses on the horizontal motion generated by earthquakes for designing building codes, needless to say that the next step is to incorporate horizontal components in the simulations as done by *Prieto and Beroza* (2008), *Denolle et al.* (2013, 2014a), and *Viens et al.* (2014) for other regions.

3.6 Conclusions

We successfully extracted vertical-to-vertical Green's functions from the ambient seismic field recorded by hundreds of seismometers in the Kanto basin. Using seismometers aligned along straight lines, we first studied the characteristics of the extracted seismic waves that propagate through the multilayered basin. For the Green's functions extracted between stations along the east-west line using the TENNOD station as virtual source, we recovered the *S* waves propagating through the basement of the basin and the fundamental mode of Rayleigh waves, which is sensitive to the first layer of the basin in the period range of 1 to 3 s and to deeper layers at longer periods. For the south-north line using the N.ITOH station as the virtual source, low-frequency Rayleigh waves are recovered after propagating through a thick layer of sediment linked to the subduction of the Philippine Sea plate along the Sagami Trough.

We demonstrated that the calibrated Green's functions can accurately simulate seismic waves generated by two shallow earthquakes that occurred close to the virtual sources. Moreover, we showed that the pseudovelocity response at a period of 6 s of the calibrated Green's functions and the recorded earthquakes have similar amplification patterns. Such a comparison validates the use of the ambient seismic field recorded by dense networks, such as MeSO-net, to predict the ground motions of future earthquakes in metropolitan areas located over sedimentary basins. Deployments of such dense array over other

metropolitan areas under the threat of potentially large earthquakes, such as Los Angeles, would be very helpful to better characterize seismic hazard.

Table 3.1: Centroid moment tensor solutions of the two earthquakes.

Origin Time (JST [a,c])	M_w [b,d]	Latitude[c]	Longitude[c]	MT Depth[d]	Strike / Dip / Rake[d]
2012/03/14 21:05:04.32	5.8	35.748N	140.932E	11 km	165 / 52 / -122
2009/12/18 08:45:36.71	4.9	34.961N	139.129E	5 km	168 / 90 / 12

[a] Japan Standard Time (UT + 9:00)

[b] Moment magnitude

[c] Determined by JMA

[d] Determined by F-net of NIED

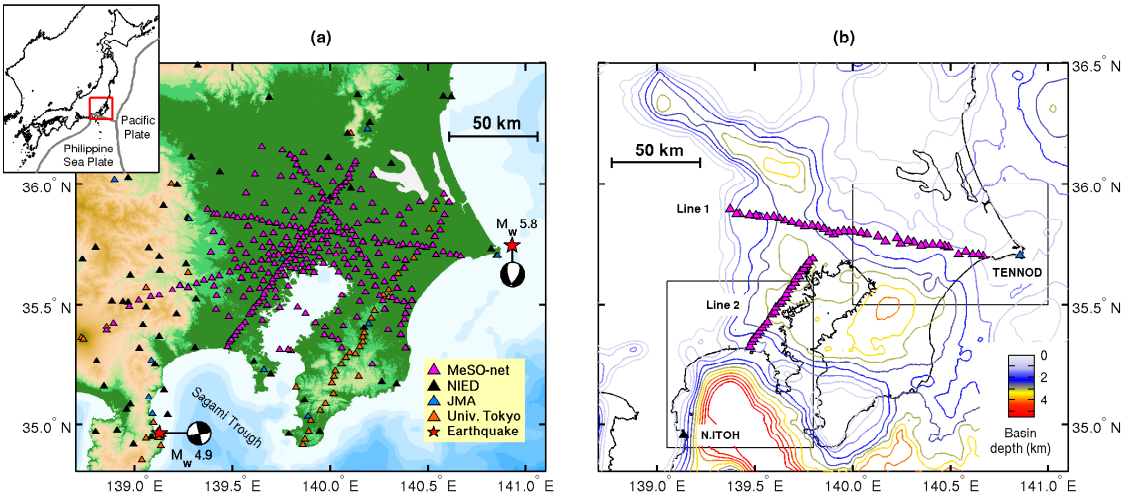

Figure 3.1: (a) Topographic map of the Kanto basin including the MeSO-net (purple triangles), Hi-net (black triangles), JMA (blue triangles), and University of Tokyo (orange triangles) stations. (b) Five hundred meter spaced basin depth contours determined from the JIVSM (*Koketsu et al.*, 2008, 2012), receiver stations aligned along Lines 1 and 2, and the two virtual sources (TENNOD and N.ITOH). Coastlines are represented by the black lines. The rectangles are the zoomed region which are presented in Figures 3.4 and 3.7. The upper left insert shows the Japanese Islands (black lines) and the plate boundaries (grey lines).

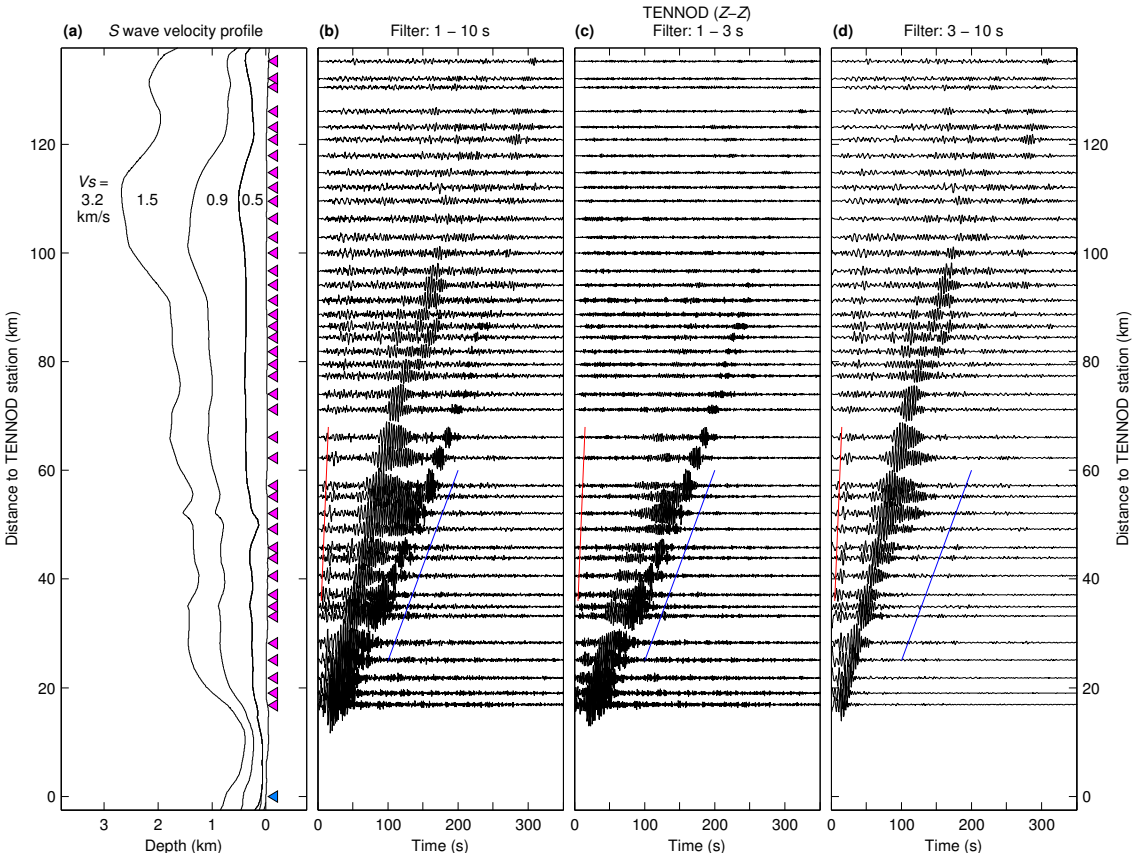

Figure 3.2: (a) Velocity profile extracted from the JIVSM beneath the stations aligned along Line 1. The *S* wave velocity of each layer is also shown. Vertical-to-vertical Green's functions extracted from the ambient seismic field, bandpass filtered between (b) 1–10 s, (c) 1–3 s, and (d) 3–10 s. The red and blue lines represent the 3.2 and 0.35 km/s moveouts, respectively.

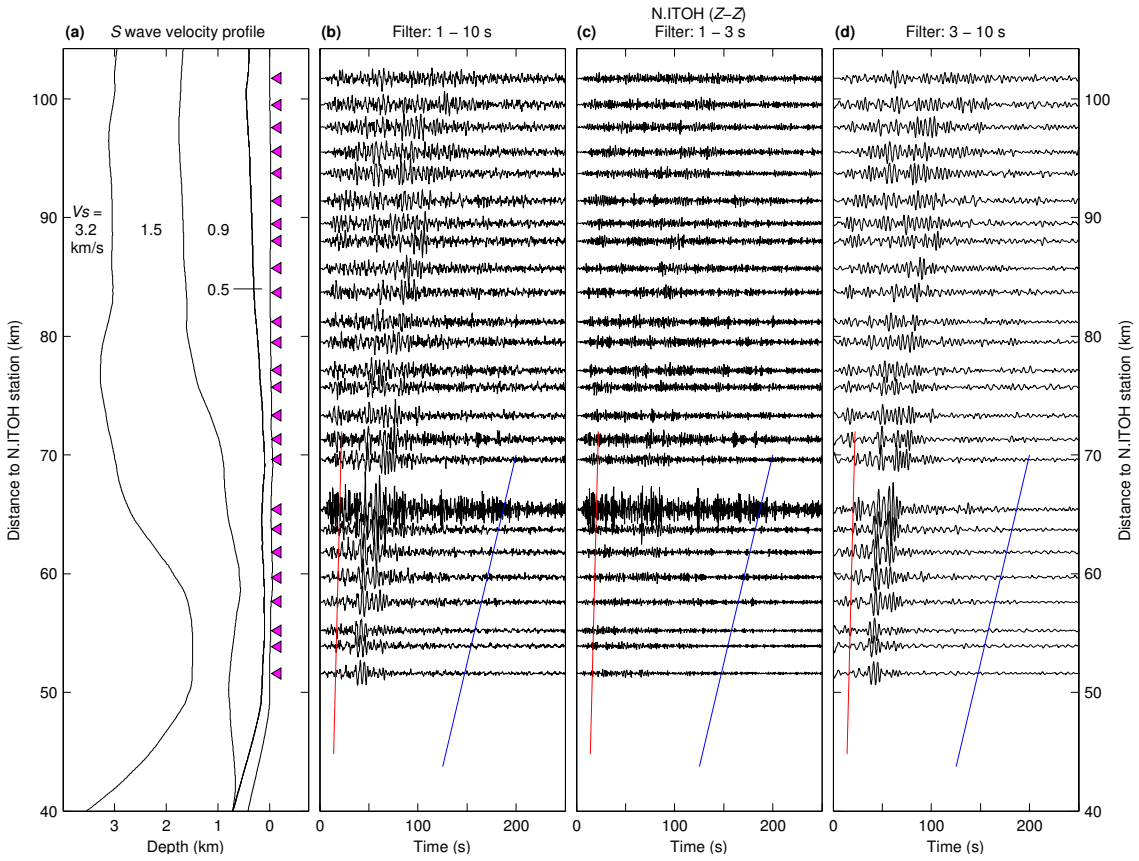

Figure 3.3: Same as Figure 3.2 for the stations aligned along Line 2.

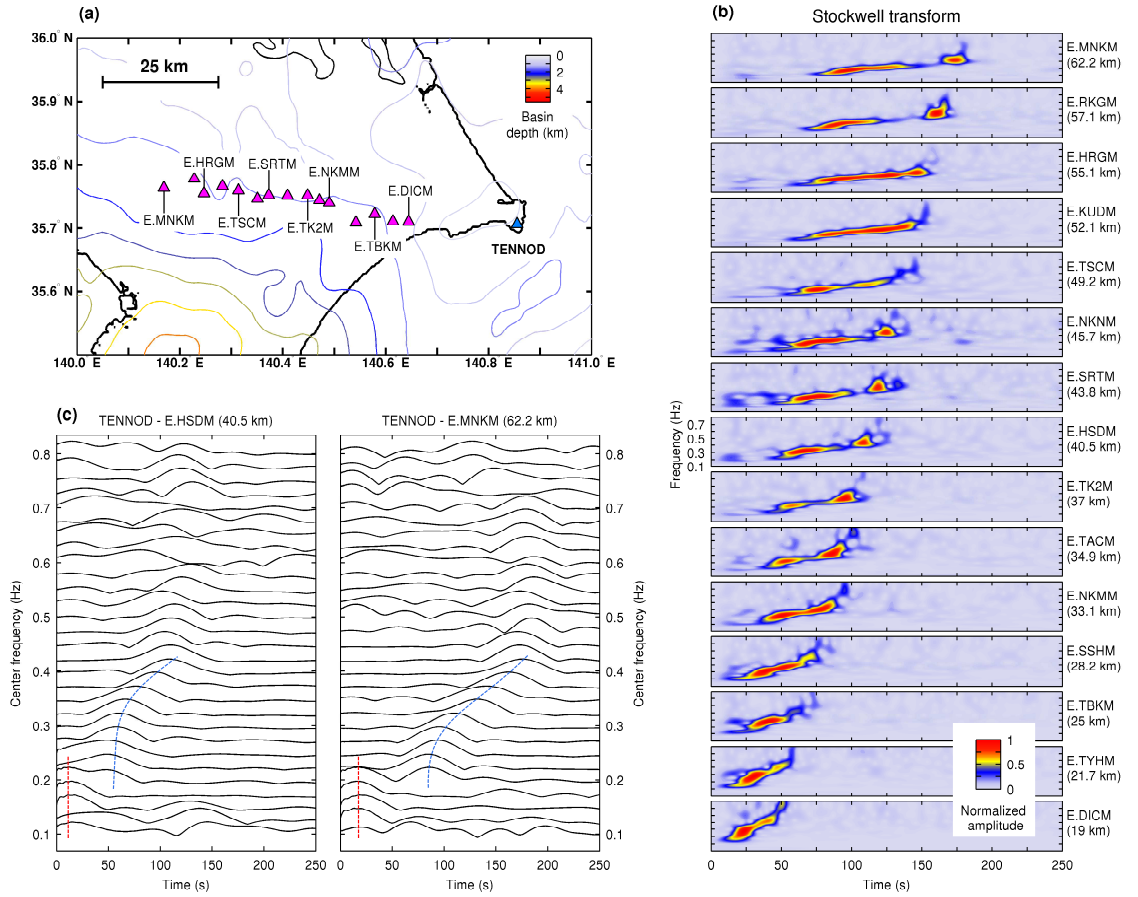

Figure 3.4: (a) Map of the basin depth including the virtual source (TENNOD) and 15 receiver stations aligned along Line 1. The same basin depth as in Figure 3.1 is indicated by the colored lines and the coastlines are represented by the black lines. (b) Time-frequency analysis of the Green's functions using the *S* transform. Each *S* transform is normalized with respect to its maximum amplitude. (c) TENNOD-E.HSDM and TENNOD-E.MNKM Green's functions bandpass filtered between different narrow frequency ranges. Each envelope is normalized with respect to its maximum amplitude. The red and blue dashed lines show the nondispersive *S* waves and the dispersion of Rayleigh waves, respectively. Distances to the virtual source are indicated between parentheses.

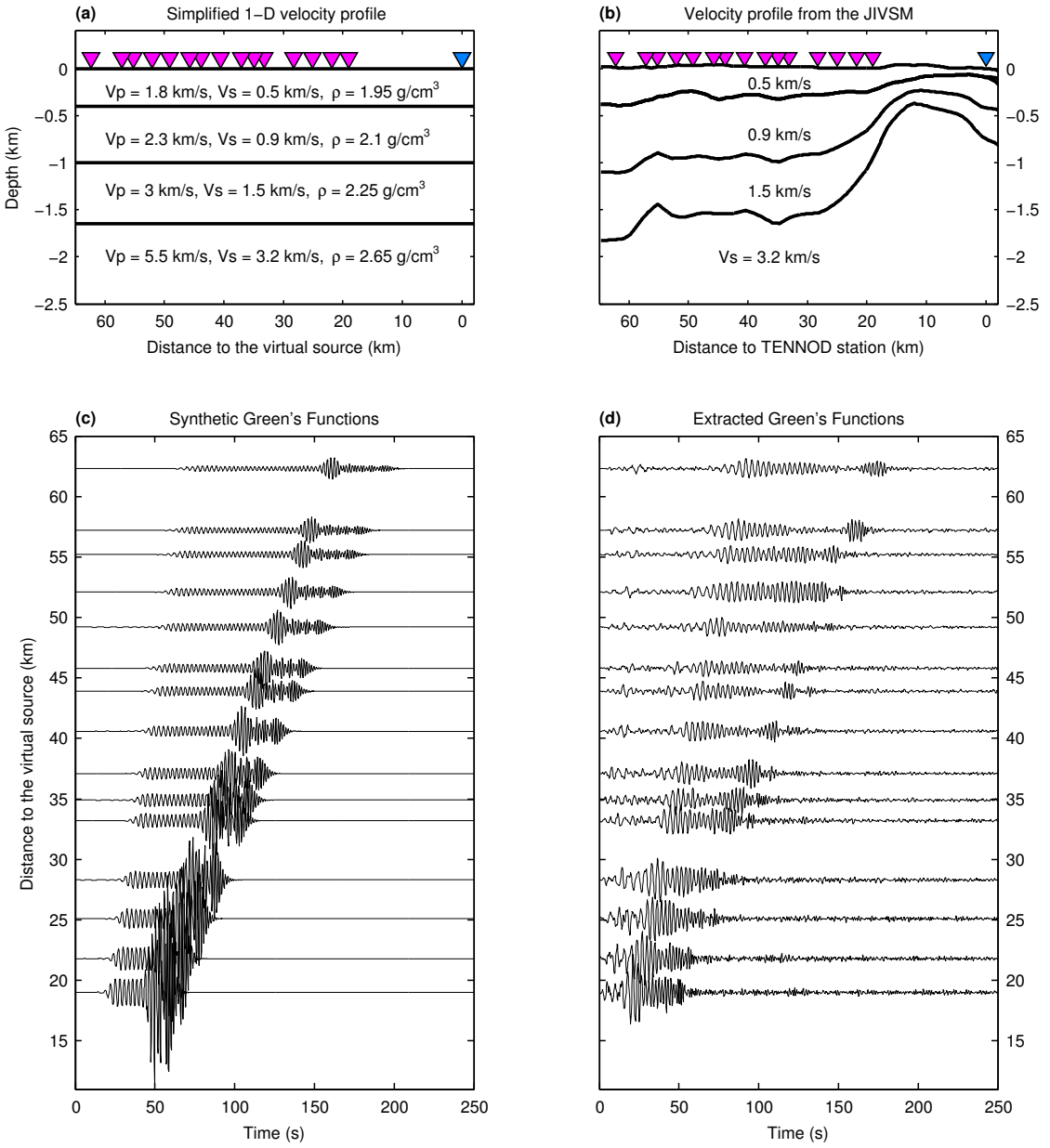

Figure 3.5: (a) Simplified 1-D velocity profile used to compute the synthetic Green's functions. (b) Velocity profile extracted from the JIVSM below the stations including *S* wave velocities. (c) Synthetic Green's functions computed using only the fundamental mode of Rayleigh waves for different distances. (d) Extracted Green's functions from the ambient seismic field using the TENNOD station as the virtual source. Waveforms have been filtered in the period range of 1 to 10 s and normalized with respect to their maximum value.

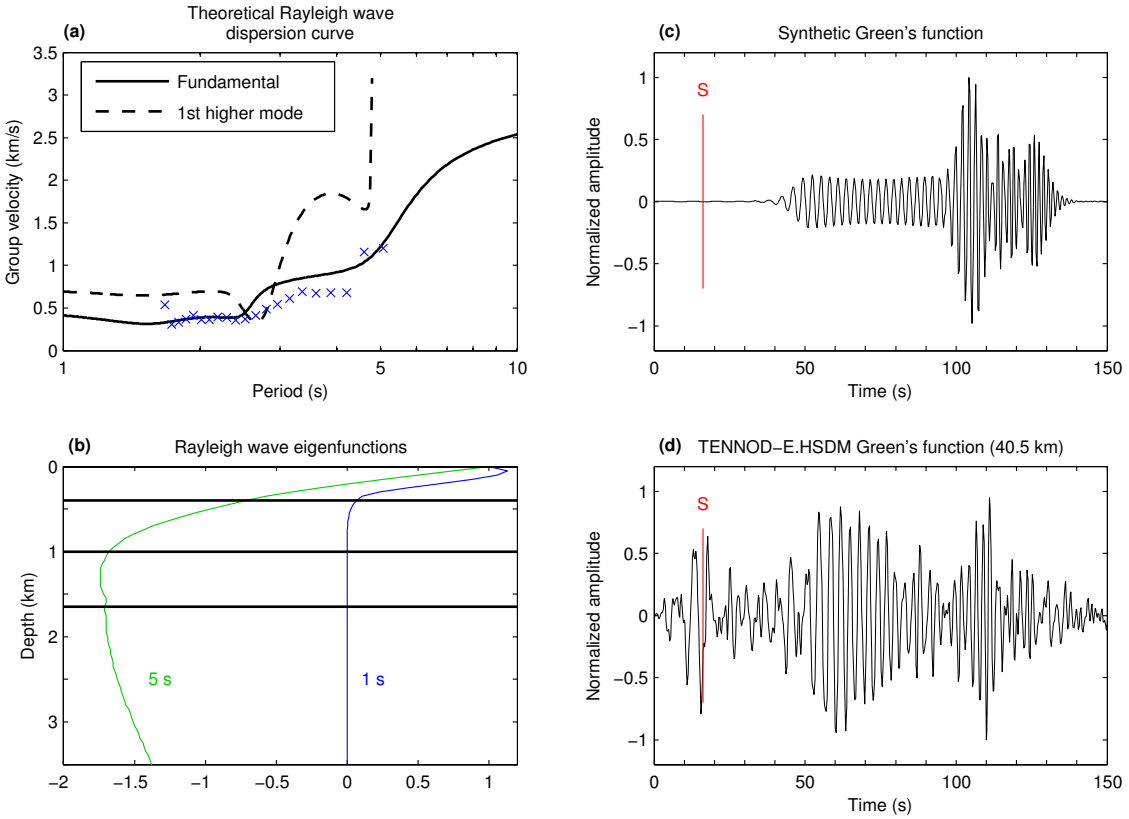

Figure 3.6: (a) Theoretical dispersion curve of the fundamental mode of Rayleigh waves (black line) computed from the synthetic Green's function shown in this figure. Blue crosses are the measured group velocities of Rayleigh waves on the Green's function extracted between the TENNOD and E.HSDM stations. The theoretical group velocity dispersion curve of the first higher mode, if included in the simulations, is shown by the dashed line. (b) Eigenfunctions of the Rayleigh wave fundamental mode at periods of 1 and 5 s are shown in blue and green, respectively. (c) Synthetic Green's function computed using only the fundamental mode of Rayleigh waves for an interstation distance of 40.5 km. (d) Extracted Green's function from the ambient seismic field between the TENNOD and E.HSDM stations. Waveforms have been filtered in the period range of 1 to 10 s and normalized with respect to their maximum value. Theoretical *S* wave arrival is also indicated by the red line.

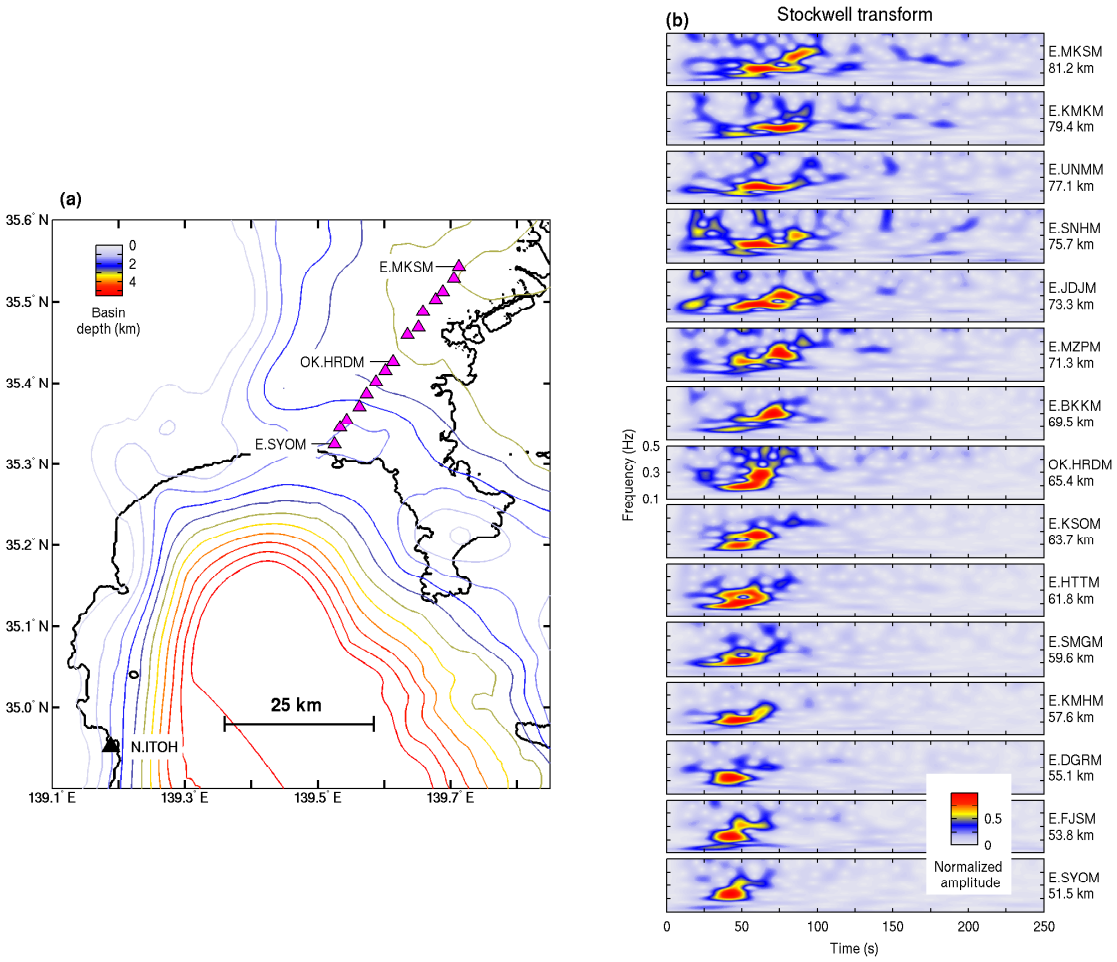

Figure 3.7: (a) Map of the basin depth including the virtual source (N.ITOH) and 15 receiver stations aligned along Line 2. The same basin depth as in Figure 3.1 is indicated by the colored lines, and the coastlines are represented by the black lines. (b) Normalized time-frequency analysis of the Green's functions using the *S* transform.

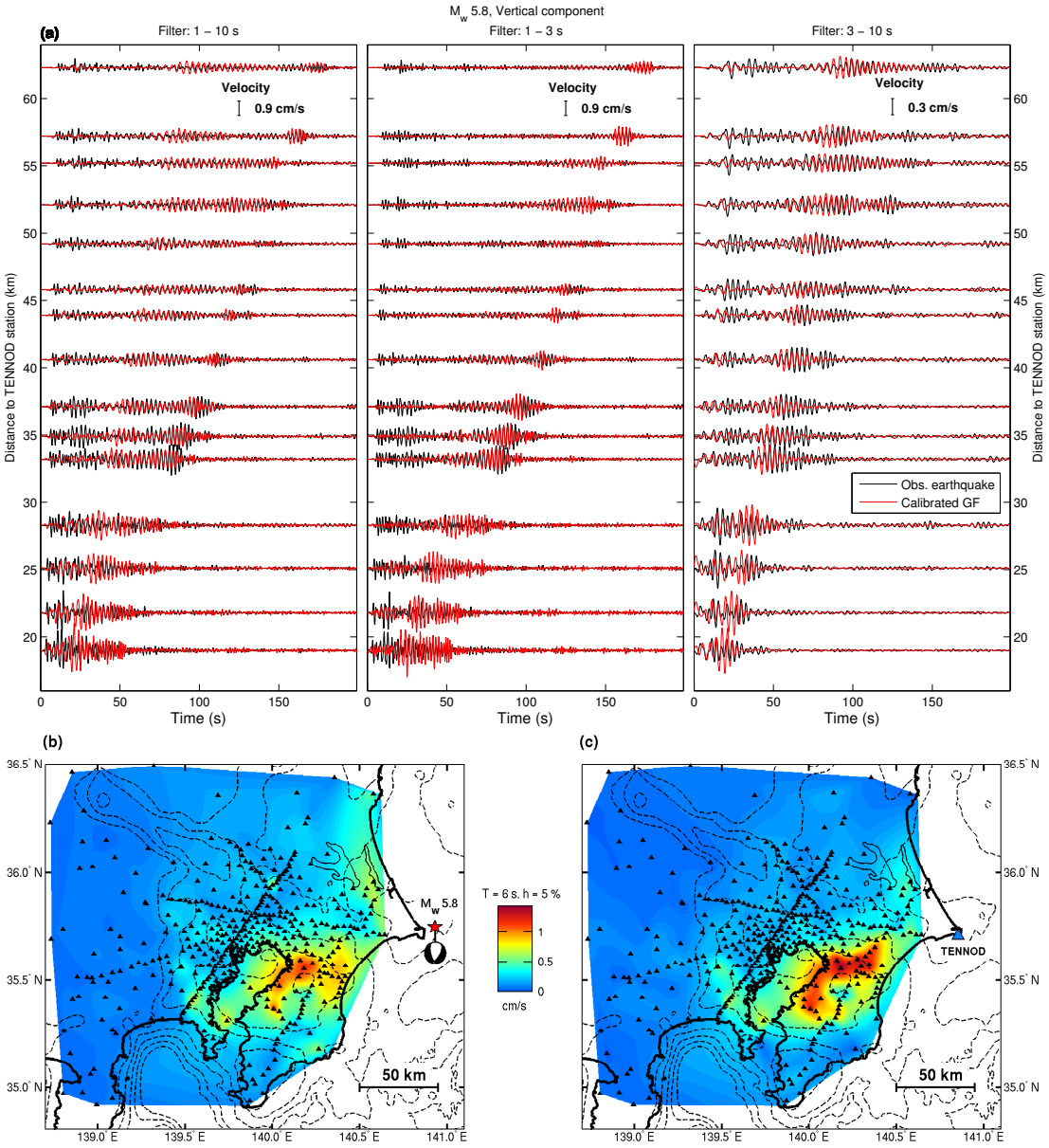

Figure 3.8: (a) Records of the M_w 5.8 earthquake (black lines) and simulations using Green's functions after calibration of the amplitude (red lines) for the same period ranges as shown in Figure 3.2. Waveforms are shown as a function of the distance from the virtual source (TENNOD) for the vertical components. Note that the scale is not the same in the period range of 3 to 10 s. Five percent damped pseudovelocity response at a period of 6 s computed from (b) records of the M_w 5.8 earthquake and (c) Green's functions after amplitude calibration. The basin depth contours spaced 1000 m apart are also indicated by the black dashed lines.

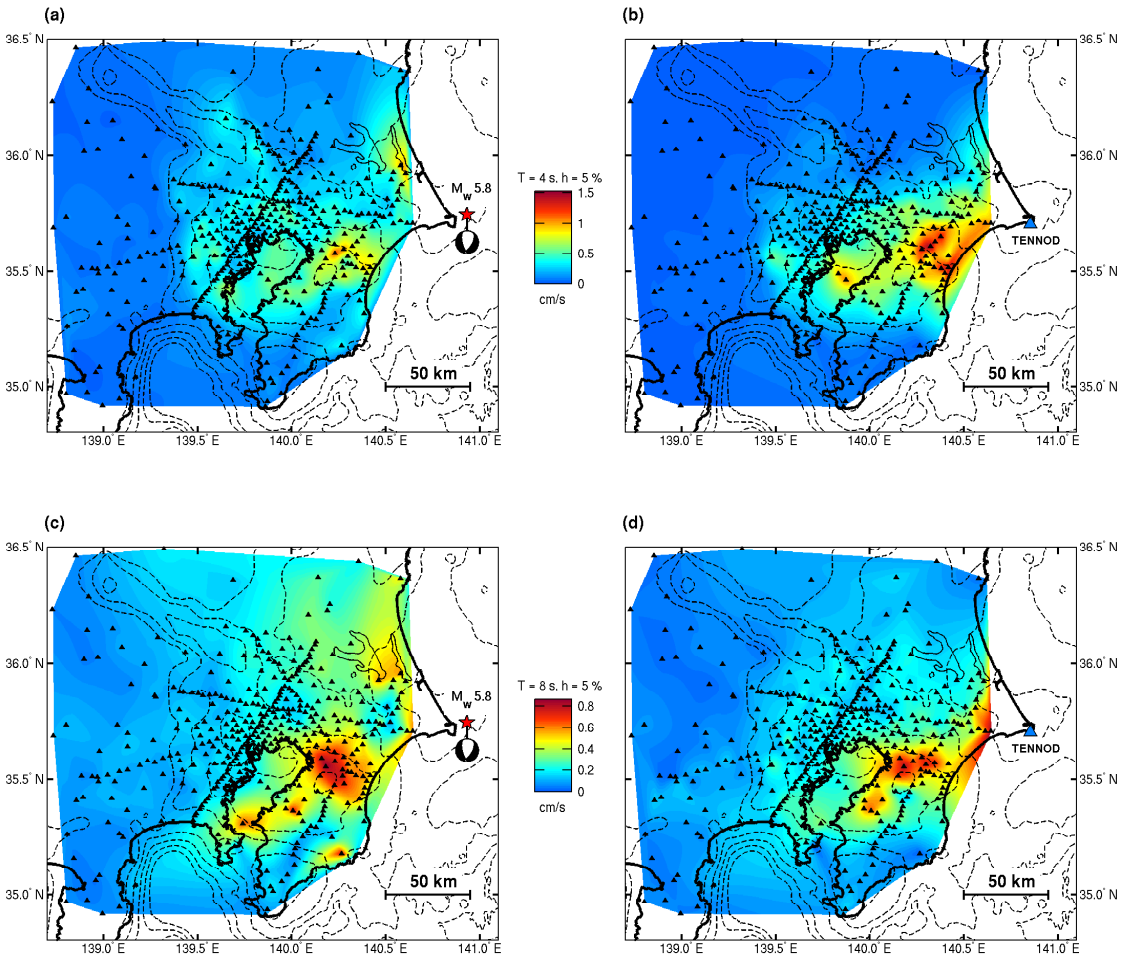

Figure 3.9: Five percent damped pseudovelocity response at periods of (up) 4 and (down) 8 s computed from (left) records of the M_w 5.8 earthquake and (right) Green's functions after amplitude calibration. The basin depth contours spaced 1000 m apart are also indicated by the black dashed lines.

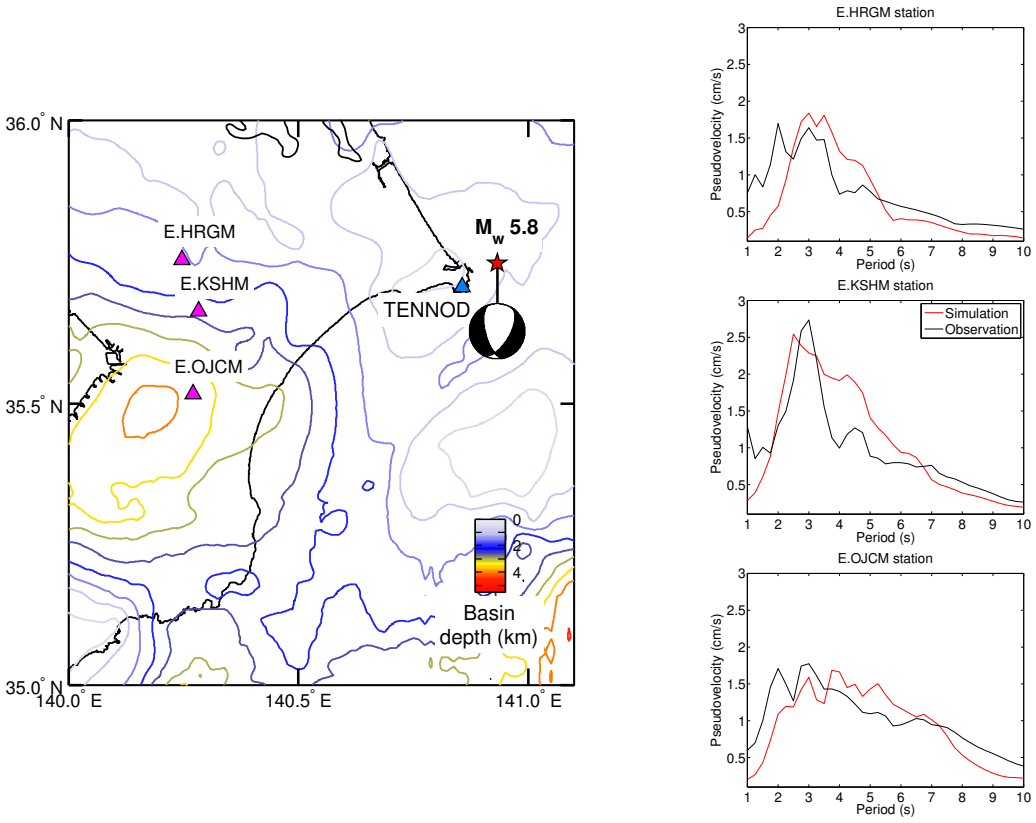

Figure 3.10: (left) Map of the Kanto basin including the location of the virtual source (TENNOD) and three receiver stations (e.g., the E.HRGM, E.KSHM, and E.OJCM stations). (right) Five percent damped pseudovelocity response spectra at the three stations computed from (black) the records of the M_w 5.8 earthquake and (red) the extracted Green's functions after amplitude calibration.

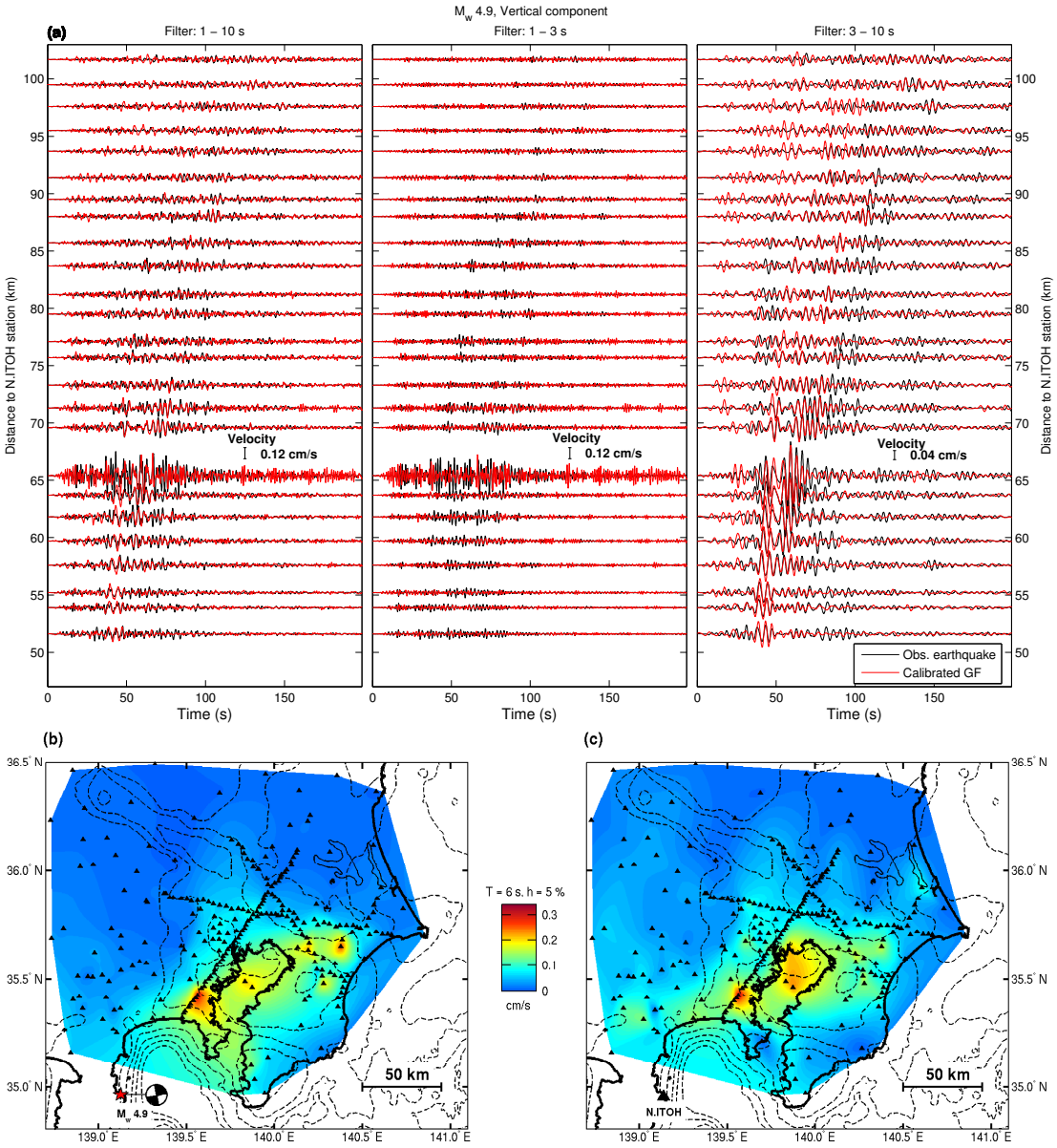

Figure 3.11: Same as Figure 3.8 for the M_w 4.9 earthquake. Note that the scales are different from the ones in Figure 3.8.

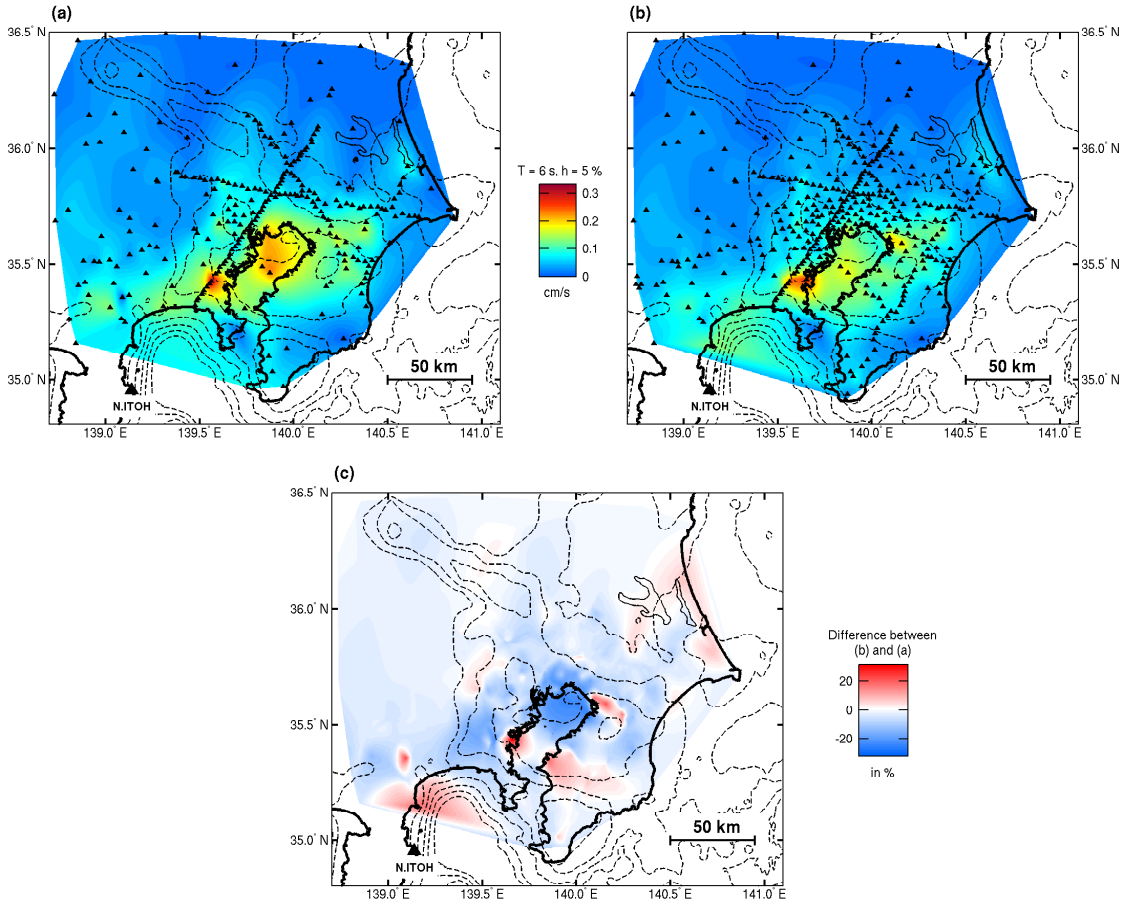

Figure 3.12: (a) Same as Figure 3.11c. (b) Five percent damped pseudovelocity response at a period of 6 s computed from all the Green's functions available in the Kanto basin. (c) Difference between the maps shown in Figures 3.12b and 3.12a in percent. The basin depth contours spaced 1000 m apart are also indicated by the black dashed lines.

Chapter 4

Long-period Ground Motion Simulations of a Large Earthquake using Finite Rupture Modeling and the Ambient Seismic Field

4.1 Introduction

Large ($M_w > 6$) earthquakes have the potential to generate strong long-period seismic waves that can be significantly amplified, even at large distances, by sedimentary basins. The prediction of these long-period ground motions (≥ 1 s) is critical to mitigate their impact on the ever-increasing number of large-scale structures, such as high-rise buildings and oil storage tanks. Physics-based methods, which simulate the whole earthquake process, have been developed to compute realistic long-period ground motions in earthquake prone regions, including the Los Angeles (*Graves et al.*, 2008; *Olsen et al.*, 2006, 2009) and Tokyo (*Furumura et al.*, 2008; *Miyake et al.*, 2008; *Takemura et al.*, 2015) metropoli-

tan areas. However, the complexity of the rupture process combined to the propagation of seismic waves through the three-dimensional Earth and local site effects makes difficult accurate predictions.

The ambient seismic field, also called seismic noise, continuously recorded by the increasing number of seismic networks has opened new insights into the prediction of long-period ground motions. The Green's function, which is the Earth response to a point force, can be extracted from the ambient seismic field recorded by a pair of stations using seismic interferometry. Point force Green's functions have been used to simulate the long-period component of the ground motions generated by crustal M_w 4–5 class earthquakes in California (*Prieto and Beroza*, 2008; *Denolle et al.*, 2013) and Japan (*Viens et al.*, 2014, 2016). *Viens et al.* (2015) showed that this method can also simulate the ground motions generated by an offshore M_w 5.0 subduction earthquake using an ocean bottom seismometer as virtual source. For large earthquakes, however, the point force hypothesis is no longer appropriate, and finite ruptures need to be taken into account.

To simulate ground motions of large earthquakes, *Denolle et al.* (2014a) extended the point source method to finite rupture modeling. Green's functions were extracted between seismometers situated atop the San Andreas fault in Southern California, which are considered as virtual sources, and receivers located in the surrounding area. The extracted Green's functions are then convolved with kinematic source time functions to simulate the long-period ground motions of several M_w 7 class earthquake scenarios. They found that parameters of the simulated ground motions, such as peak ground velocities (PGVs), agree generally well with those computed with the physics-based simulations of the CyberShake project (*Graves et al.*, 2011). However, it is still critical to verify the accuracy of this method with past large earthquakes.

The M_w 6.9 Iwate-Miyagi Nairiku earthquake occurred on 14 June 2008 (Japan standard time) in the central part of the Tohoku region in Northeast Japan. This reverse

faulting mechanism event generated strong accelerations that almost reached 4000 gal close to the hypocenter area (*Aoi et al.*, 2008; *Yamada et al.*, 2009), causing several casualties, collapse of houses and a bridge, and severe landslides (Figure 4.1). We choose this earthquake because of its shallow depth (6.5 km) and its location among dozens of three-component seismometers recording continuously the ambient seismic field. These sensors, which are shown in Figure 4.2, are a part of several networks including the Hi-net of the National Research Institute for Earth Science and Disaster Prevention (NIED) (*Okada et al.*, 2004; *Obara et al.*, 2005), Japan Meteorological Agency (JMA), and Tohoku University networks.

We first extract Green's functions from the ambient seismic field by regarding stations located in the vicinity of the mainshock fault plane as virtual sources and other stations as receivers. We show that after accounting for the non-uniform distribution of the ambient seismic field sources and surface wave radiation patterns of the earthquake, amplitude calibrated Green's functions extracted between the N.IW2H virtual source and receiver stations accurately simulate the long-period ground motions of a M_w 5.0 aftershock. Using empirical scaling relations between small and large earthquakes, we construct simple finite source models that are similar to those determined by source inversion studies to simulate the long-period ground motions of the mainshock.

4.2 Methods

4.2.1 Extraction of Green's Functions from the Ambient Seismic Field

We use the ambient seismic field continuously recorded by approximately 100 seismic stations which are shown in Figure 4.2. Most of the stations are short-period seismometers with natural periods of 0.5 or 1 s. In this study, we target the period range of 4 to 15 s that is below these two natural periods. However, the seismometers, which have a wide

dynamic range recording system, can also be used in this period range after instrument response correction.

We extract Green's functions from the ambient seismic field by regarding five stations situated in the vicinity of the mainshock fault plane (e.g., the N.IW2H, N.NRKH, N.KGSH, N.HNRH, and ICHINM stations in Figure 4.2) as virtual sources. Continuous data recorded during the whole year 2014 are first decimated from 100 Hz down to 4 Hz to speed up the computation process and earthquakes are removed from the data set. For each pair of virtual source and receiver, Green's functions are computed in the frequency domain ω using the deconvolution method (*Prieto and Beroza*, 2008; *Denolle et al.*, 2013; *Viens et al.*, 2014, 2015, 2016) as

$$G_{ij}(x_r, x_s, t) = \left\langle \mathfrak{F}^{-1} \left(\frac{\hat{u}_j(x_r, \omega)\, \hat{u}_i^*(x_s, \omega)}{\{|\hat{u}_i(x_s, \omega)|\}^2 + \xi} \right) \right\rangle. \tag{4.1}$$

$\hat{u}_i(x_s, \omega)$ and $\hat{u}_j(x_r, \omega)$ are Fourier-transformed 1 h time series that are computed using the multitaper method at the virtual source x_s and the receiver x_r, respectively. i and j are the ith component at the virtual source and the jth component at the receiver. A smoothing of the denominator $\{\,\}$ and a water level ξ are added to keep stable the deconvolution. $*$ is the complex conjugate and $|\ |$ represents the absolute value. The inverse Fourier-transform $\mathfrak{F}^{-1}$ of every 1 h hour deconvolutions are computed and stacked over 1 year, denoted by $\langle\rangle$, to retrieve Green's functions in the time domain t. Finally, causal and acausal parts of the Green's functions are summed up together and resampled to 10 Hz to increase the resolution of the waveforms.

We only compute the diagonal terms of the nine component Green's tensor, which are the vertical-to-vertical (Z-Z), north-to-north, and east-to-east components. The extracted Green's functions are then rotated from the East-North-Vertical (ENZ) coordinate system to Radial-Transverse-Vertical (RTZ). By rotating the Green's tensor, we suppose that the fundamental mode of Rayleigh waves is recovered on the vertical and radial components,

and that the one of Love waves is retrieved on the transverse component. This hypothesis is considered to be valid because the surface-to-surface Green's functions are mainly dominated by surface-wave fundamental modes in the period range of this study. As we only compute the diagonal terms of the Green's tensor, we simplify the notation for the components at the virtual source and the receiver (e.g., i and j) by only considering one of the two (i), which corresponds to Z,R, or T.

4.2.2 Amplitude Calibration and Simulation of a M_w 5.0 Aftershock

We first focus on the simulation of a M_w 5.0 aftershock by using the Green's functions extracted between the N.IW2H station which is regarded as the virtual source, and other stations. This aftershock occurred on 4 July 2010 close to the mainshock hypocenter with a similar reverse faulting focal mechanism. As shown by previous studies, the amplitude of extracted Green's functions needs to be calibrated with the records of the targeting earthquake. We use the same calibration factor as *Viens et al.* (2014) to calibrate the amplitude of all the Green's functions for the M_w 5.0 aftershock as

$$v_i(t) = G_i(t) \times \lambda_i, \tag{4.2}$$

where $v_i(t)$ is the amplitude calibrated Green's function, $G_i(t)$ is the extracted Green's function, and λ_i is the calibration factor that is the same for all stations, but different for each component i.

The primary sources of ambient seismic field in the Tohoku region are the Pacific Ocean and the Japan Sea. This non-uniform distribution of the ambient seismic field has a strong impact on the Green's function amplitudes. To quantify this effect, we correct the calibrated Green's functions for the surface wave geometrical spreading (e.g., $1/\sqrt{r}$, where r is the virtual source-receiver distance) and pick the long-period PGVs of the waveforms that are bandpass filtered between 4 and 15 s. These corrected long-period

PGVs are shown with those of the recorded earthquake with respect to the azimuth angle in Figure 4.3. The best fitting sinusoidal functions (in the least-squares sense) are also shown in this figure. For the R-R, T-T, and Z-Z components, Green's functions extracted between the virtual source and the stations located in along the east-west axis have larger corrected PGVs than those extracted between the stations aligned along the north-south direction. This azimuthal amplification pattern is caused by the non-uniform distribution of the ambient seismic field sources that are mainly derived from the Pacific Ocean and the Japan Sea. For the earthquake, the largest corrected PGVs are also observed in the east-west direction for the radial and vertical components. This feature can be explained by the Rayleigh wave radiation pattern effect of this reverse faulting event, which mainly excited Rayleigh waves in the east-west direction. For the transverse component, the azimuthal pattern is less clear, but amplifications can be observed in four different directions. This amplification pattern is coherent with the Love waves radiation pattern effect for a reverse faulting event. To account for the directivity of the ambient seismic field and the surface wave radiation patterns of the earthquake, we correct the amplitude of the Green's functions with an azimuth dependent factor that is computed from the ratio of the fitting sinusoidal functions of the earthquake and Green's function PGVs. This azimuth dependency factor is added to the amplitude calibration introduced in Equation 4.2 for each component i as

$$v_i(t) = G_i(t) \times \lambda_i \times \frac{f_i^{\mathrm{eq}}(\phi_{\mathrm{eq}})}{f_i^{\mathrm{G}}(\phi_{\mathrm{G}})}, \tag{4.3}$$

where f_i^{eq} and f_i^{G} are the best fitting sinusoidal functions for the earthquake and Green's function PGVs, respectively. ϕ_{eq} is the azimuth angle between the earthquake epicenter and each receiver, and ϕ_{G} is the one between the virtual source and each receiver.

The amplitude calibrated Green's function waveforms are shown together with the earthquake records in the period range of 4 to 15 s in Figure 4.4 for 12 receiver stations

aligned along a SW–NE axis. The location of these stations is indicated in Figure 4.2. To compare quantitatively the earthquake and calibrated Green's function phases, we compute correlation coefficients (CC) between 5 and 92.5 percent of the cumulative energy of both signals for each station. A correlation coefficient equal to 1 indicates that both waveforms are perfectly in phase and a coefficient equal to -1 indicates that the waveforms are out of phase by 180°. Note that we allow a free phase shift of 1.5 s when computing the correlation coefficient to account for possible uncertainties (e.g., hypocenter location, occurrence time, and theoretical surface wave velocity used to correct for the difference of location between the hypocenter and virtual source locations) as done by *Denolle et al.* (2013).

The simulated waveforms agree well with those of the recorded earthquake for the vertical and horizontal components. The highest correlation coefficients are observed for the vertical component. Despite the low correlation coefficient for some stations, the duration of the strong ground motions and long-period PGVs are similar for most of the stations. Moreover, local amplifications at the N.YNZH and N.YGTH stations, which are located in boreholes where the S wave velocity is slower than 1000 m/s, are also well simulated.

To compare quantitatively the difference between waveform amplitudes, we compute the ratio between simulated and observed long-period PGVs (e.g., $\mathrm{PGV_{sim}}/\mathrm{PGV_{obs}}$) and show the distribution of this ratio in Figure 4.5. For the vertical, radial, and transverse components, 88%, 80%, and 82% of the 122 calibrated Green's function PGVs are within the range of 0.5 to 2 times the ones of the earthquake (e.g., green triangles), respectively. To quantify the distribution of Green's function PGVs smaller than half or larger than twice earthquake PGVs (e.g., blue and red triangles), we also compute the residuals of long-period PGVs ($\log_{10}(\mathrm{PGV_{sim}}/\mathrm{PGV_{obs}})$) that are shown as a function of the distance to the virtual source in Figure 4.5. The means of the residuals are very close to 0 for

the three components and the standard deviations σ are equal to 0.187, 0.216, and 0.216 for the vertical, radial, and transverse components, respectively. Such results demonstrate that the long-period component of earthquake ground motions can be accurately simulated over the whole azimuth range only by using simple correction functions to calibrate the amplitude of the Green's functions.

4.2.3 Simulation of the 2008 M_w 6.9 Iwate-Miyagi Nairiku Earthquake

Several studies investigated the source process of the 2008 M_w 6.9 Iwate-Miyagi Nairiku earthquake (e.g., *Yokota et al.*, 2009; *Suzuki et al.*, 2010; *Cultrera et al.*, 2013). The source models retrieved by inversion suggest that the length and the width of the fault plane are approximately 40 and 18 km, respectively. We summarize several parameters obtained by the inversions in Table 4.1.

To simulate the mainshock, we construct three source models that are used together with the extracted Green's functions. The first model uses the point source hypothesis and is called Model P1. The second and third model are homogeneous finite source models that are used together with the Green's functions extracted using one (Model H1) and five (Model H2) virtual sources.

For each source model, two simulations are performed. In the first simulation, we only calibrate the amplitude of the Green's functions with a calibration factor that is independent from the azimuth as in Equation 4.2 for the M_w 5.0 aftershock. In the second simulation, which is denoted by an asterisk *, Green's functions are calibrated with a factor that depends on the azimuth. This factor is the ratio of the fitting functions obtained for the M_w 5.0 aftershock (Equation 4.3), which has a focal mechanism similar to the one of the mainshock.

Models P1 and P1*: Point Source Models

We first use a point source model to simulate the long-period ground motions of the mainshock. The amplitude of the Green's functions extracted by regarding the N.IW2H station as the virtual source is calibrated with the records of the mainshock as in Equation 4.2 for the aftershock. This simulation is refereed as Model P1. In Model P1*, we further correct the Green's function amplitudes for the non-uniform distribution of the ambient seismic field sources and surface waves radiation patterns using the $f_i^{\mathrm{eq}}(\phi_{\mathrm{eq}})/f_i^{\mathrm{G}}(\phi_{\mathrm{G}})$ term of Equation 4.3, which is obtained for the M_w 5.0 aftershock that has a similar focal mechanism to the one of the mainshock.

Models H1–H1* and H2–H2*: Homogeneous Finite-Source Models

To construct homogeneous finite-source models, we use empirical scaling relations of the source parameters between small and large earthquakes. These scaling relations, developed by *Kanamori and Anderson* (1975), can be summarized as

$$\frac{M_0}{m_0} = \frac{L}{l} = \frac{W}{w} = \frac{T}{\tau} = N^3, \tag{4.4}$$

where L, W, and T are the length, width, and rise time of the large earthquake and l, w, and τ are those of the small event. N is the ratio of the fault dimensions between the two earthquakes and is an integer. For the 2008 M_w 6.9 Iwate-Miyagi Nairiku earthquake, the inversion of *Suzuki et al.* (2010) showed that the length of the fault plane is 40 km along the strike direction (N209°E) and the width is 18 km along the dip direction (40°). As the Green's functions are calibrated with the M_w 5.0 aftershock, we compute the moment magnitude ratio ($M_0/m_0 = (2.73\times10^{19}\ \mathrm{Nm})/(4.13\times10^{16}\ \mathrm{Nm})$) and find that N is equal to 9. Therefore, we divide the fault plane into 9 by 9 subfaults having a length l and a width w of 4.44 and 2.0 km, respectively. The projection of the fault plane at the surface and

the distribution of the 81 subfaults are shown in Figure 4.6.

For each receiver station and each component, one Green's function for each subfault center $v_i^{mn}(t)$ is required. Therefore, we interpolate the amplitude calibrated Green's functions in the time domain as

$$v_i^{mn}(t) = \sum_{k=1}^{K} \alpha_{mnk} \times v_i^k(t - \frac{d_{mn} - d_k}{V_{\text{surf}}}), \tag{4.5}$$

where $v_i^k(t)$ is the amplitude calibrated Green's function extracted between the kth virtual source and each receiver station. K is the number of virtual source stations that are used (e.g., one in Model H1 and five in Model H2). Superscripts m and n are integers ranging from 1 to N and indicate the subfault position along the strike and dip angles, respectively. α_{mnk} is a weighting coefficient that is described below. The $(d_{mn} - d_k)/V_{\text{surf}}$ term in the equation accounts for the difference of travel time of surface waves V_{surf}, which is set to 3.0 km/s, between each virtual source and the receiver station d_k, and each subfault and the receiver station d_{mn}.

The weighting coefficient that is applied to the extracted Green's functions depends on the distance between each virtual source and each subfault center (r_{mnk}) and can be summarized as

$$\alpha_{mnk} = \left(r_{mnk} \times \sum_{k=1}^{K} \frac{1}{r_{mnk}} \right)^{-1}, \tag{4.6}$$

where the $\sum_{k=1}^{K} \frac{1}{r_{mnk}}$ term is a constant that keeps the sum of the α_{mnk} equal to 1 (e.g., $\sum_{k=1}^{K} \alpha_{mnk} = 1$). Note that α_{mnk} is equal to 1 for Model H1 because only one virtual source station is used. The different distances that are used to interpolate the Green's functions are summarized in Figure 4.7.

The ground motions of the large event are finally computed by summing the interpolated Green's functions over the fault plane and correcting for the difference of slip

over the fault plane between the small and large events. The computation of the ground motions generated by the large event is similar to the one introduced by *Hartzell* (1978) and *Irikura* (1983) that uses records of small earthquakes instead of Green's functions extracted from the ambient seismic field. Mathematically, the summation process can be written as

$$V_i(t) = \sum_{m=1}^{N} \sum_{n=1}^{N} \frac{\sqrt{d}}{\sqrt{d_{mn}}} F(t) * v_i^{mn}(t), \tag{4.7}$$

where $V_i(t)$ is the simulated waveform of the large earthquake and $v_i^{mn}(t)$ is the interpolated Green's function at each subfault. As we calibrate the amplitude of the Green's functions with a M_w 5.0 earthquake that occurred close to the N.IW2H station, we also add the $\sqrt{d}/\sqrt{d_{mn}}$ term to account for the distance difference between the considered subfault and each receiver (d_{mn}), and the distance between the N.IW2H station and each receiver (d). The square root of the distances is taken to consider the geometrical spreading of surface waves. $F(t)$ is a correction function that accounts for the difference of slip between the small and large events and is a sum of Dirac delta functions as

$$F(t) = \sum_{o=1}^{N} \delta(t - \frac{\xi_{mn}}{V_r} - (o-1)\tau), \tag{4.8}$$

where ξ_{mn} is the distance between the hypocenter and the considered subfault (Figure 4.7), and V_r is the rupture velocity. Following the empirical relation between slip duration and seismic moment of *Somerville et al.* (1999), we obtain a rise time for the M_w 5.0 event (τ) that is equal to 0.15 s. Therefore, the duration of the correction function $F(t)$ is set to 1.3 s, which corresponds to N times the rise time of the small event. As mentioned previously, the sampling rate of the Green's functions is 10 Hz. Therefore, we set the correction function $F(t)$ as sum of 13 Dirac delta functions that have their amplitudes calibrated for the integral of $F(t)$ from 0 to T being equal to N.

4.3 Ground Motion Simulation Results

4.3.1 Comparison of Point Source and Homogeneous Source Models

We compare the simulated ground motions of Models P1, P1*, H1, H1*, H2, and H2* to the observed velocity records at 3 stations in Figure 4.8. For the homogeneous source models, we use a rupture velocity of 1.8 km/s to compute the simulated waveforms (*Suzuki et al.*, 2010). All the waveforms are bandpass filtered between 4 and 15 s. For the 3 stations, which are shown in Figure 4.2, simulated ground motions agree quite well with the observed waveforms in terms of phases and long-period PGVs.

Several features need to be highlighted for these simulations. First, the azimuthal correction factor that is applied in Models P1*, H1*, and H2* only affects the amplitude of the simulated waveforms and does not modify the phase. Second, the simulated waveforms of Model H2 reproduce well the first surface wave arrivals but underestimate the amplitude of the later phases. Finally, the waveforms of Models P1 and H1 are very similar and are the ones that agree the most with the observed waveforms. However, Model P1 is computed after calibration of the amplitude with the waveforms of the mainshock, meaning that records of the large event are required to perform the simulations. The great advantage of finite source modeling is that the scaling is done using the ratio between the moment magnitude of the small and large earthquakes. Moreover, finite source modeling allows to separate several effect of the source process, such as the rupture velocity and the presence/absence of asperities in the source model, and determine their roles in the simulation of the ground motions.

4.3.2 Effect of Rupture Velocity

To study the effect of the rupture velocity on the simulated ground motions, we perform the simulations using different rupture velocities ranging from 1.7 to 2.4 km/s for the

homogeneous source Models H1, H1*, H2, and H2*. For each model, we compute the residuals of the long-period PGVs ($log_{10}(\mathrm{PGV_{sim}}/\mathrm{PGV_{obs}})$) for the three components and average the three values for each rupture velocity. Results are shown in Figure 4.9, in which negative values indicate that the simulated PGVs underestimate the observed ones. Rupture velocities that minimize the residuals of the average of the three components for Models H1, H1*, H2, and H2* are 1.95, 1.8, 2.15, and 2.0 km/s, respectively. The simulations that include the azimuth dependent factor have their residuals minimized for slower velocities. Moreover, the positive values of the residuals for all the models computed using rupture velocities higher than 2.2 km/s show that if the rupture velocity during this event was higher, the long-period PGVs would have been larger.

The rupture velocities that minimize the residuals for the four models are very close to the 1.8 and 1.8–2 km/s obtained by the inversion studies of *Suzuki et al.* (2010) and *Cultrera et al.* (2013), respectively. The inversion study of *Yokota et al.* (2009) uses a rupture velocity of 2.8 km/s for the first time window, which is significantly higher than 1.8 km/s. However, their results generally show a smaller rupture velocity of approximately 2.0 km/s. Therefore, the results obtained with the homogeneous source models are coherent with the three inversion results, which confirm the validity of the technique to simulate the ground motions of large seismic events.

4.3.3 Effect of Azimuthal Correction Factor and Virtual Source Selection

To compare the effect of the azimuthal calibration factor on the simulations, we show the residuals of the long-period PGVs for Models P1, P1*, H1, H1*, H2, and H2* as a function of the distance to the fault plane in Figure 4.10. For the homogeneous source models, simulations computed with the rupture velocities that minimize the residuals are

selected (e.g., Section 4.3.2). For the point source Model P1, the mean of the residuals is slightly lower than zero, meaning that the simulated PGVs underestimate the observed ones. Moreover, the residuals generally decrease with distance to the fault plane. The addition of the azimuthal calibration factor to the point source model in Model P1* allows to retrieve a mean closer to zero and to remove the decreasing trend. The standard deviation of the residuals drops from 0.271 to 0.227, which indicates that the azimuthal calibration factor improves the simulation of the long-period PGVs for the point source model. On the other hand, the addition of the azimuthal calibration factor leads to larger standard deviations for the homogeneous source models. Indeed, standard deviations increase from 0.242 to 0.275 for Model H1 and from 0.271 to 0.286 for Model H2. This feature might be explained by the extended size of the fault plane over dozens of kilometers that causes a change of azimuth angle for each subfault. Such small or large azimuth changes can lead to an over- or under-estimation of the long-period PGVs, respectively.

The standard deviation of the simulations computed with Model H2 is larger than the one of Model H1. As shown in Figure 4.8, waveforms computed with Model H1 are more similar to the observed ones than those computed with Model H2. The interpolation of the Green's functions extracted using virtual sources located quite far away from the fault plane (e.g., the N.HNRH and ICHINM stations) might have a negative impact on the interpolated Green's functions. For this reverse faulting earthquake, we observe that the use of one virtual source station located in the middle of the fault plane gives the best results. However, this feature cannot be generalized with the results of only one seismic event, and similar computations for several earthquakes having different focal mechanisms need to be performed.

In the following, we only consider the waveforms obtained with Model H1 and a rupture velocity of 1.95 km/s for which the best fit with the observed waveforms is obtained. We compare the simulated and observed waveforms of the mainshock in the period range

of 4 to 15 s in Figure 4.11 for the same stations as in Figure 4.4. As for the aftershock, the best fit between the waveforms is observed for the vertical components and local amplifications at the N.YNZH and N.YGTH stations are also well retrieved. However, the large amplification peaks on the transverse component for the stations located on the northern part of the fault plane (e.g., the N.TOUH and OHASAM stations) are not retrieved.

We also present the distribution of the simulated and observed long-period PGV ratios in Figure 4.12 for Model H1. For the vertical, radial, and transverse components, 82%, 81%, and 81% of the 103 stations have their simulated PGVs within the range of 50% to 200% of the recorded ones (e.g., green triangles), respectively. Note that the number of stations that recorded the mainshock is smaller than for the M_w 5.0 aftershock. In the middle panels of Figure 4.12, we present the distribution of residuals of the long-period PGVs against the closest distance to the fault plane. Residuals are distributed around zero and have standard deviations that are equal to 0.243, 0.245, and 0.239, for the vertical, radial, and transverse components, respectively. We finally compare the attenuation of the long-period PGVs with the increasing distance to the fault plane in the lower panels of Figure 4.12. The data are fitted with a $1/\sqrt{r}$ function (in the least-squares sense). The attenuation of simulated and observed long-period PGVs with the increasing distance agree well for most of the stations. Such results demonstrate that the simulations performed using a simple uniform source model can provide reliable parameters of the ground motions generated by a large event.

4.4 Discussion

Inversion studies of the source process of the 2008 M_w 6.9 Iwate-Miyagi Nairiku earthquake also showed that in addition to the parameters listed in Table 4.1, two patches of large slip occurred near the hypocenter area and close to the northern shallow part of the

fault plane (Figure 4.13). To investigate the effect that might have asperities on long-period ground motions, we modify the source model. First, we set the area of the fault covered by asperities to 22% of the total rupture area (*Somerville et al.*, 1999), which corresponds to 18 of the 81 subfaults that compose the fault plane. We show in Figure 4.14a the location of these subfaults, with 15 around the hypocenter and 3 close to the northern edge of the fault plane. The location of the asperities roughly corresponds to the location of the large slip areas found by *Yokota et al.* (2009) and *Suzuki et al.* (2010). Inversion studies also showed that the slip on the asperities is approximately four times larger than the one of the background. Therefore, we modify the correction function $F(t)$ to increase its contribution on the asperity to be four times the one of the background. As $M_0/m_0 = N^3$, the asperity area multiplied by the correction function summed to the background area multiplied by the correction function of the background area should by equal to N^3. The correction functions for the background and the asperities used in the computation of the waveforms are shown in Figures 4.14b and 4.14c.

We compare the waveforms obtained from Model H1 to those obtained with the asperity Model A1 in Figure 4.15 using a rupture velocity of 1.95 km/s. The waveforms of the asperity model are highly similar to the ones of the homogeneous model in terms of phases. The addition of asperities mostly affects the amplitude of the simulated waveforms which are higher than those of the homogeneous model for these three stations.

To compare the effect of the rupture velocity of the asperity model, we also compute the simulations for different rupture velocities also ranging between 1.7 and 2.4 km/s. We show the mean of residuals of the long-period PGVs for the three components in Figure 4.15. The rupture velocity that minimize the average of the residuals is 1.75 km/s which is very close to the one found by the inversion of *Suzuki et al.* (2010). However, the standard deviation of the long-period PGVs for the asperity model is 0.27, which is higher than the one of the Model H1 (0.242).

All the source models presented in this paper reproduce quite well the observed ground motions of the 2008 M_w 6.9 Iwate-Miyagi Nairiku earthquake. Among these models, the homogeneous finite source model H1 that is used together with the Green's functions with one virtual source (N.IW2H) and considering a rupture velocity of 1.95 km/s explains the most the long-period ground motions of this seismic event. Such result implies that the asperities are not a critical parameter in the simulation of the long-period ground motions for this event.

4.5 Conclusions

We extracted Green's functions from the ambient seismic field using seismic stations located close to the fault plane of the 2008 M_w 6.9 Iwate-Miyagi Nairiku earthquake as virtual sources and other stations as receivers. In the Tohoku region, the amplitude of the extracted Green's functions is strongly affected by the non-uniform distribution of the ambient seismic field sources. To simulate the ground motions of a M_w 5.0 aftershock having the same reverse faulting focal mechanism as the mainshock, we corrected the amplitude for the non-uniform distribution of the ambient seismic field sources and for the surface waves radiation patterns using an azimuth dependent calibration factor. Despite the simplicity of this calibration factor that only account to the first order for the amplitude variations with the azimuth, amplitude calibrated Green's functions well simulate the vertical and horizontal components of the long-period ground motions generated by this M_w 5.0 aftershock.

To simulate the 2008 M_w 6.9 Iwate-Miyagi Nairiku earthquake, we used three different source models together with the extracted Green's functions. We compared the differences between the models and the observed waveforms. Results show that the homogeneous finite source model constructed using scaling laws between small and large

earthquakes combined to the Green's functions extracted regarding the N.IW2H station as the virtual source explain well the observed waveforms in the period range of 4 to 15 s.

The simulations presented in this study validate the use of the ambient seismic field to estimate the long-period ground motions of large events using simple finite source models. This method combined to very dense networks, such as the Metropolitan Seismic Observation network (MeSO-net) that has been deployed in the Tokyo metropolitan area, could be a powerful tool to assess the seismic hazard related to the surrounding subduction zones.

Table 4.1: Source parameters of the M_w 6.9 Iwate-Miyagi Nairiku earthquake from several inversion studies.

Study	M_w (M_0 in Nm) Latitude Longitude Depth	Fault size $L \times W$ (km)	Rupture velocity (km/s)	Strike / Dip / Rake
Yokota et al. (2009)	6.9 (2.7×10^{19}) 39.028N 140.88E 6 km	42 × 18	Triggering value: 2.8	203 / 37 / 90 ± 45°
Suzuki et al. (2010)	6.9 (2.73×10^{19}) 39.027N 140.878E 6.5 km	40 × 18	1.8	209 / 40 / 104 ± 22.5°
Cultrera et al. (2013)	6.9 (3.65×10^{19}) 39.027N 140.878E 6.5 km	44.4 × 19	1.8–2.0	209 / 40 / 104 ± 20°

Figure 4.1: Pictures of (top) the collapsed Matsurube bridge and (bottom) a landslide that occurred close to the Aratozawa dam during the 2008 Iwate-Miyagi Nairiku earthquake (From *Joint reconnaissance Committee on the Iwate-Miyagi Nairiku Earthquake Disaster in 2008*, 2009).

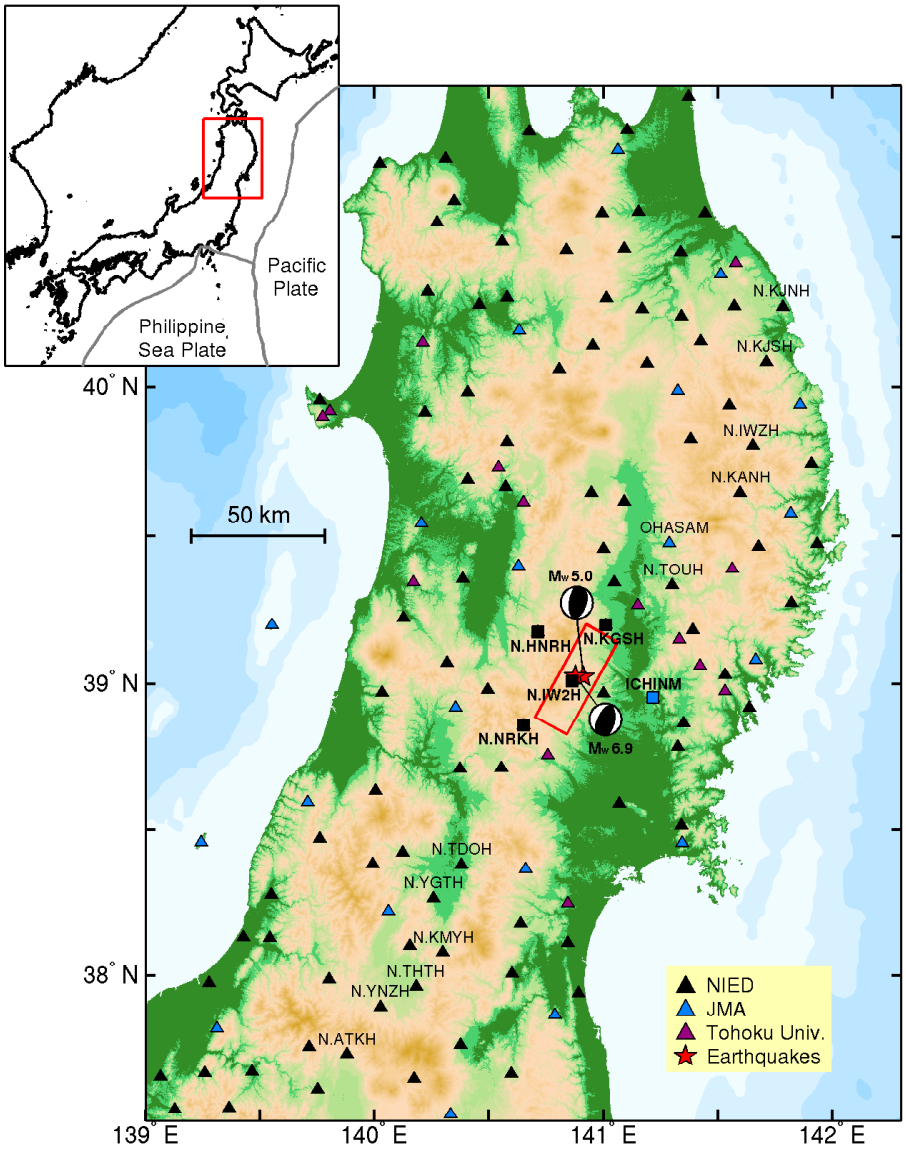

Figure 4.2: Topographic map of the Tohoku region including Hi-net (black triangles), JMA (blue triangles), and Tohoku University (purple triangles) stations that recorded the mainshock and the M_w 5.0 aftershock (red stars). Virtual source stations used to simulate the mainshock are indicated by the squares and their names are shown in bold. Names of the receiver stations for which waveforms are shown in the following figures are also indicated. The fault plane of the mainshock determined by *Suzuki et al.* (2010) is indicated by the red rectangle.

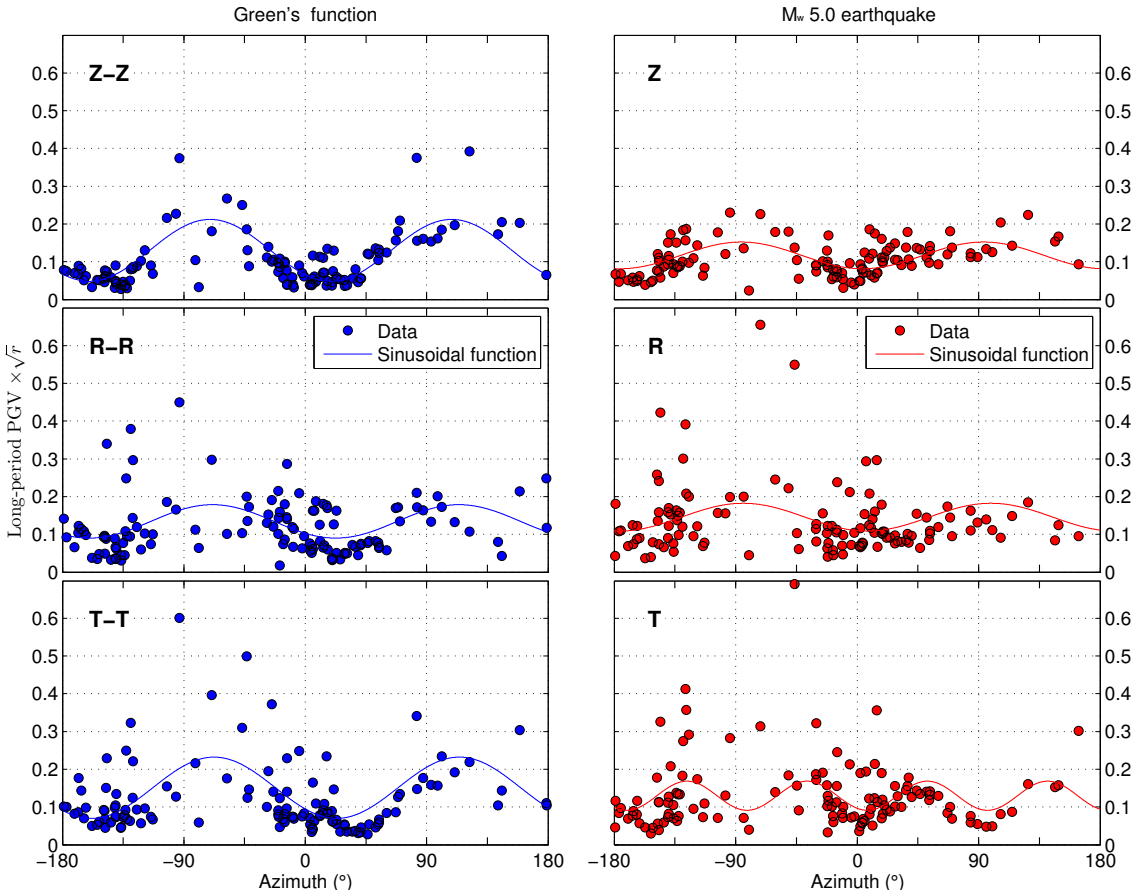

Figure 4.3: (Left panels) Z-Z, R-R, and T-T long-period PGVs of the extracted Green's functions corrected for surface wave geometrical spreading versus azimuth. The virtual source is the N.IW2H station. (Right panels) Z, R, and T long-period PGVs of the recorded M_w 5.0 earthquake also corrected for surface wave geometrical spreading versus azimuth. The zero azimuth angle is the north. For each panel, the best fitting sinusoidal function is shown.

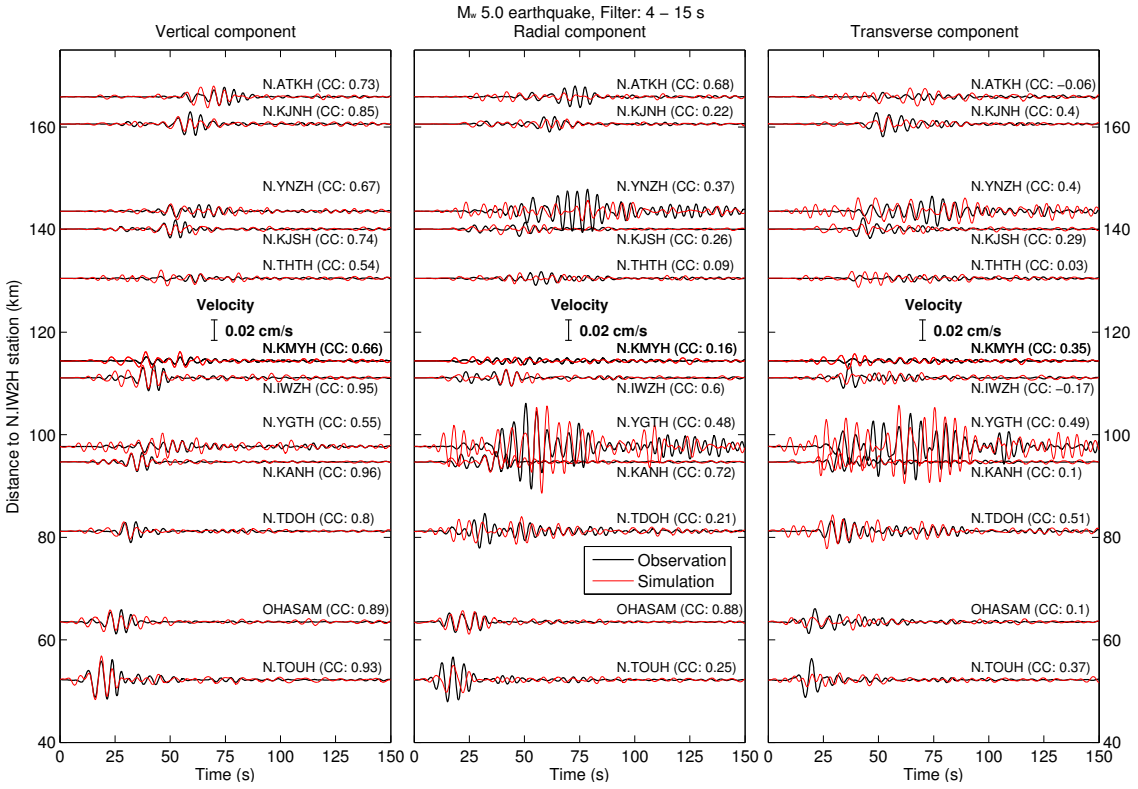

Figure 4.4: Simulated (red) and observed (black) long-period ground motions of the M_w 5.0 aftershock for the receivers shown in Figure 4.2. The waveforms of the vertical, radial, and transverse components are bandpass filtered between 4 and 15 s and are shown as a function of the distance from the virtual source (N.IW2H). Correlation coefficients (CC) are given in parentheses for each station.

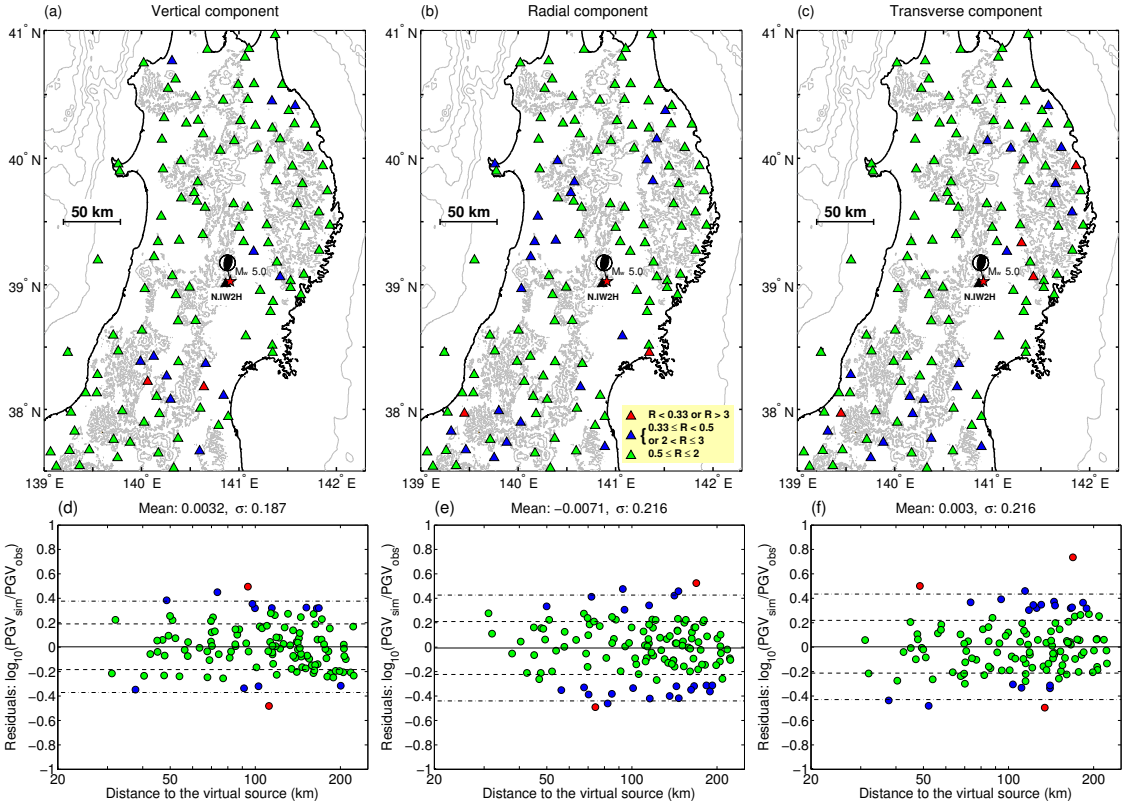

Figure 4.5: Distribution of the ratio between simulated and observed long-period PGVs of the 2010 M_w 5.0 aftershock (e.g., R = $\mathrm{PGV_{sim}}/\mathrm{PGV_{obs}}$) for the (a) vertical, (b) radial, and (c) transverse components. (d–e) Residuals ($\log_{10}(\mathrm{PGV_{sim}}/\mathrm{PGV_{obs}})$) versus distance to the fault plane. The mean of the data is shown by the solid line. The dashed and dash-dotted lines are the one and two standard deviations, respectively. Values of the mean and the standard deviation (σ) for each component are also indicated. The color of the circles corresponds to the one of (a–c) maps.

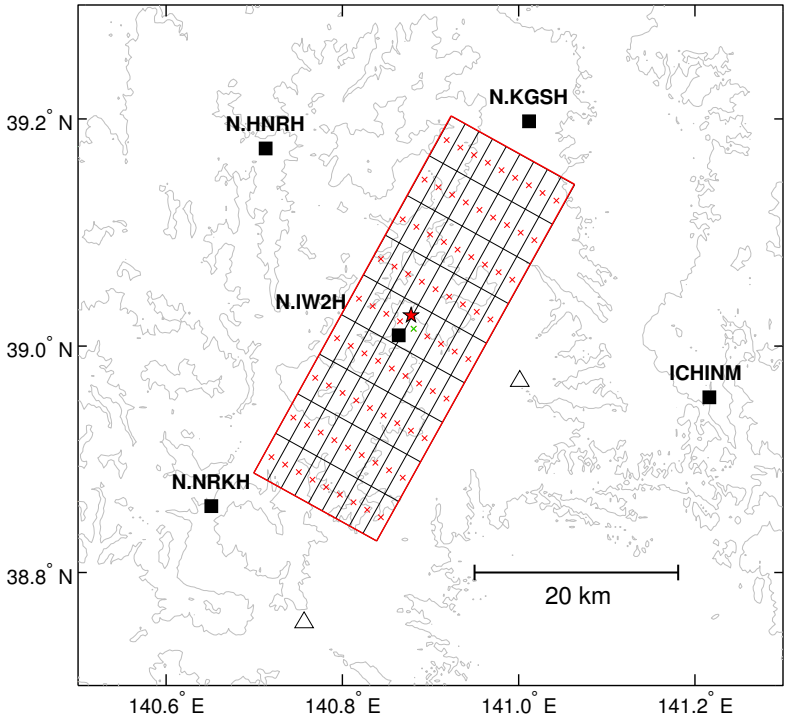

Figure 4.6: Map of the fault plane including the five virtual source stations (black squares). The center of each subfault is indicated by a red cross. The green cross indicates the subfault where the rupture is initiated. The true epicenter of the 2008 M_w 6.9 Iwate-Miyagi Nairiku earthquake is indicated by the red star. The stations shown by the white triangles are not taken into account in the computation of the Green's functions.

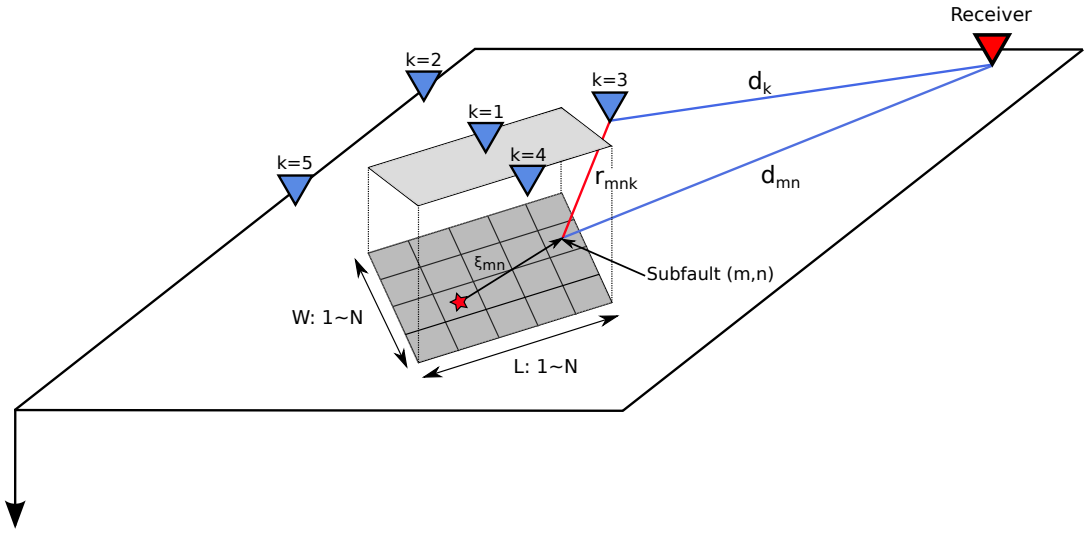

Figure 4.7: Schematic representation of the different distances used to interpolate the Green's functions for each subfault center. The virtual source stations are shown by the blue downward-pointing triangles and one receiver station is shown by the red downward-pointing triangle. The star represents the hypocenter of the simulated earthquake.

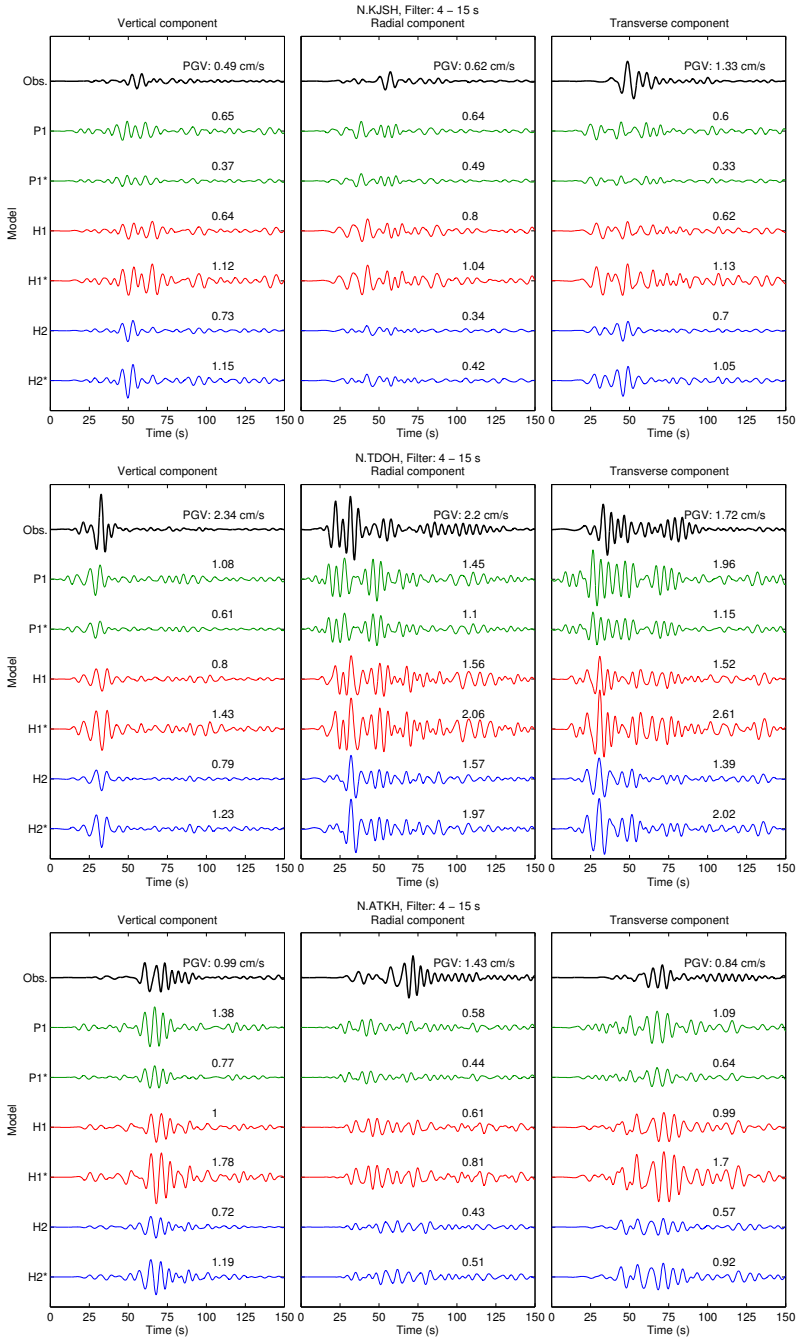

Figure 4.8: Comparison of the observed (black) and simulated (colored) waveforms of Models P1,P1*, H1, H1*, H2, and H2* for the 2008 M_w 6.9 Iwate-Miyagi Nairiku earthquake at three stations. The waveforms for the three components are bandpass filtered between 4 and 15 s and the long-period PGV is shown for each waveform.

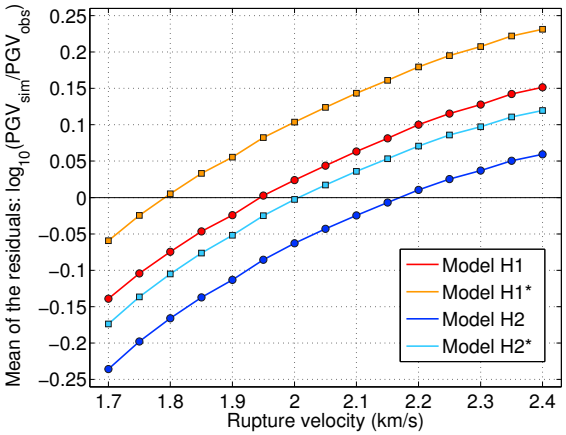

Figure 4.9: Average over the three components (e.g., vertical, radial, and transverse) of the mean of the residuals ($\log_{10}(\mathrm{PGV_{sim}}/\mathrm{PGV_{obs}})$ as a function of the rupture velocity for Models H1, H1*, H2, and H2*.

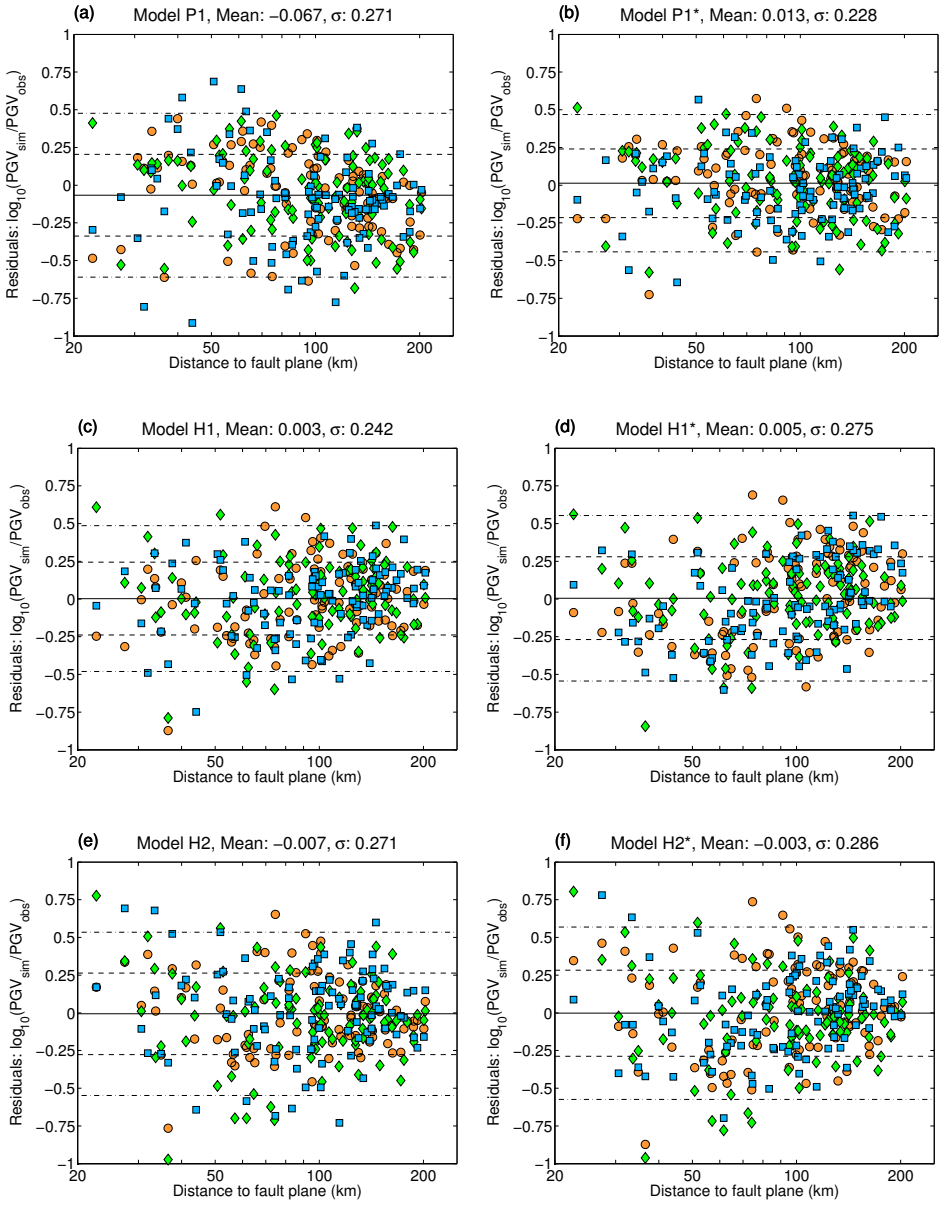

Figure 4.10: Residuals computed from the logarithm of the ratio of the simulated over observed long-period PGVs ($\log_{10}(\mathrm{PGV_{sim}}/\mathrm{PGV_{obs}})$) are shown as a function of the distance to the fault plane for the homogeneous models. The residuals of the three components are shown together for (a–b) the point source Models P1 and P1*, (c–d) the homogeneous Models H1 and H1*, and (e–f) the the homogeneous Models H2 and H2*. The four homogeneous models are those for which the rupture velocity minimize the mean of the residuals for the three components (Figure 4.9).

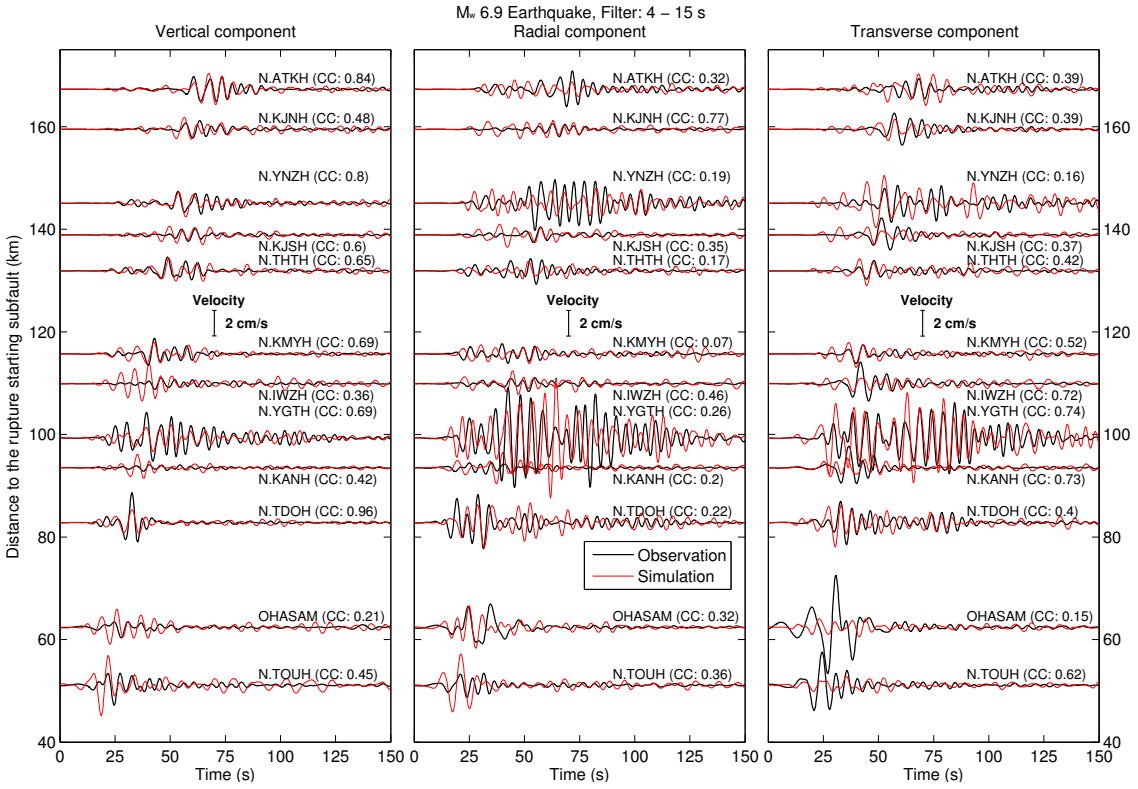

Figure 4.11: Simulated (red) and observed (black) waveforms bandpass filtered between 4 and 15 s of the 2008 M_w 6.9 Iwate-Miyagi Nairiku earthquake. Note that the velocity scale is different from Figure 4.4 and that the distance is taken from the rupture starting subfault.

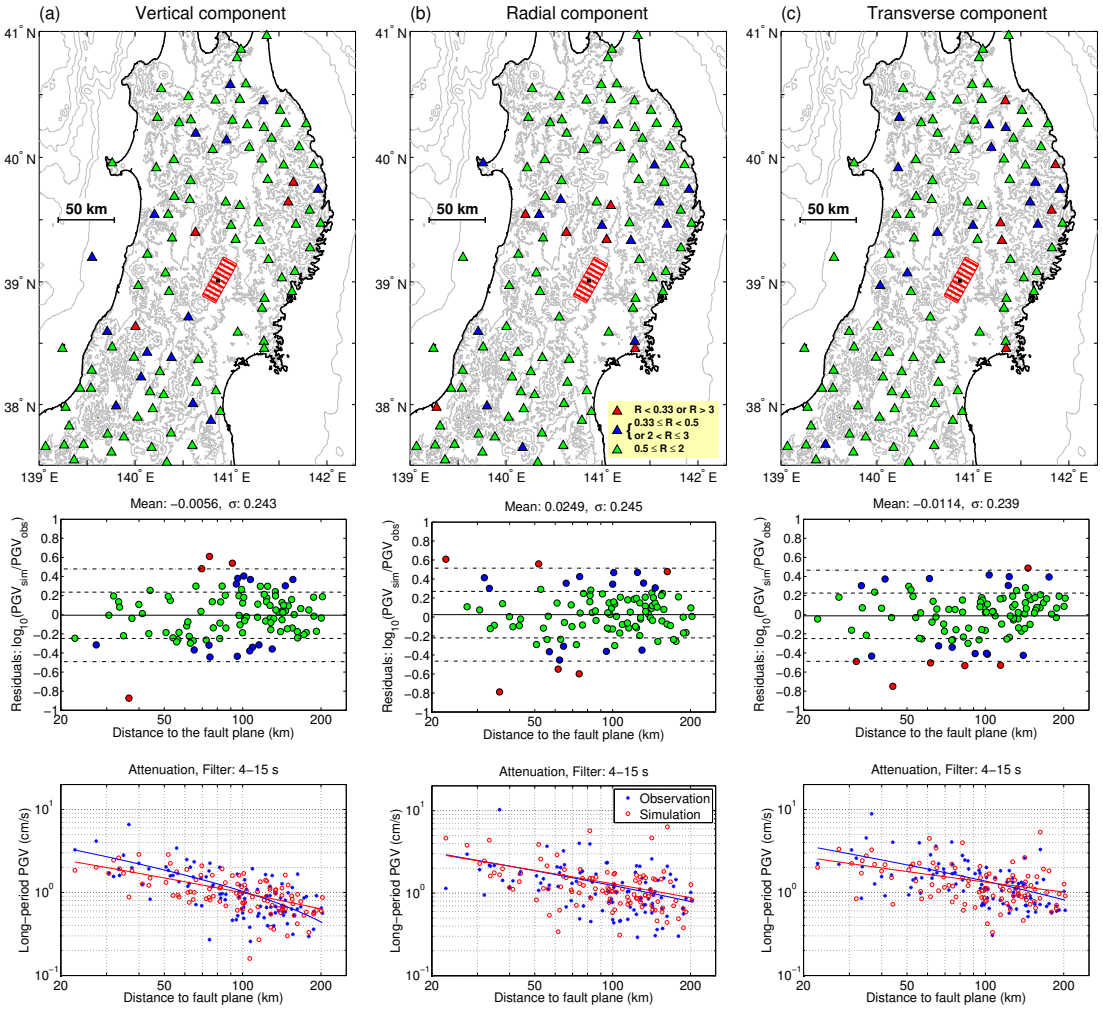

Figure 4.12: (Top panels) Distribution of the ratio between simulated and observed long-period PGVs of the 2008 M_w 6.9 Iwate-Miyagi Nairiku earthquake (e.g., $\mathrm{PGV_{sim}}/\mathrm{PGV_{obs}}$) for the (a) vertical, (b) radial, and (c) transverse components. Simulated PGVs are taken from the waveforms computed using the uniform source model and a rupture velocity of 1.95 km/s. (Middle panels) Residuals ($\log_{10}(\mathrm{PGV_{obs}}/\mathrm{PGV_{sim}})$ versus distance to the fault plane. (Bottom panels) Simulated (red) and observed (blue) long-period PGVs versus distance to the fault plane for the three components. The best fitting functions in least square sense are shown as lines.

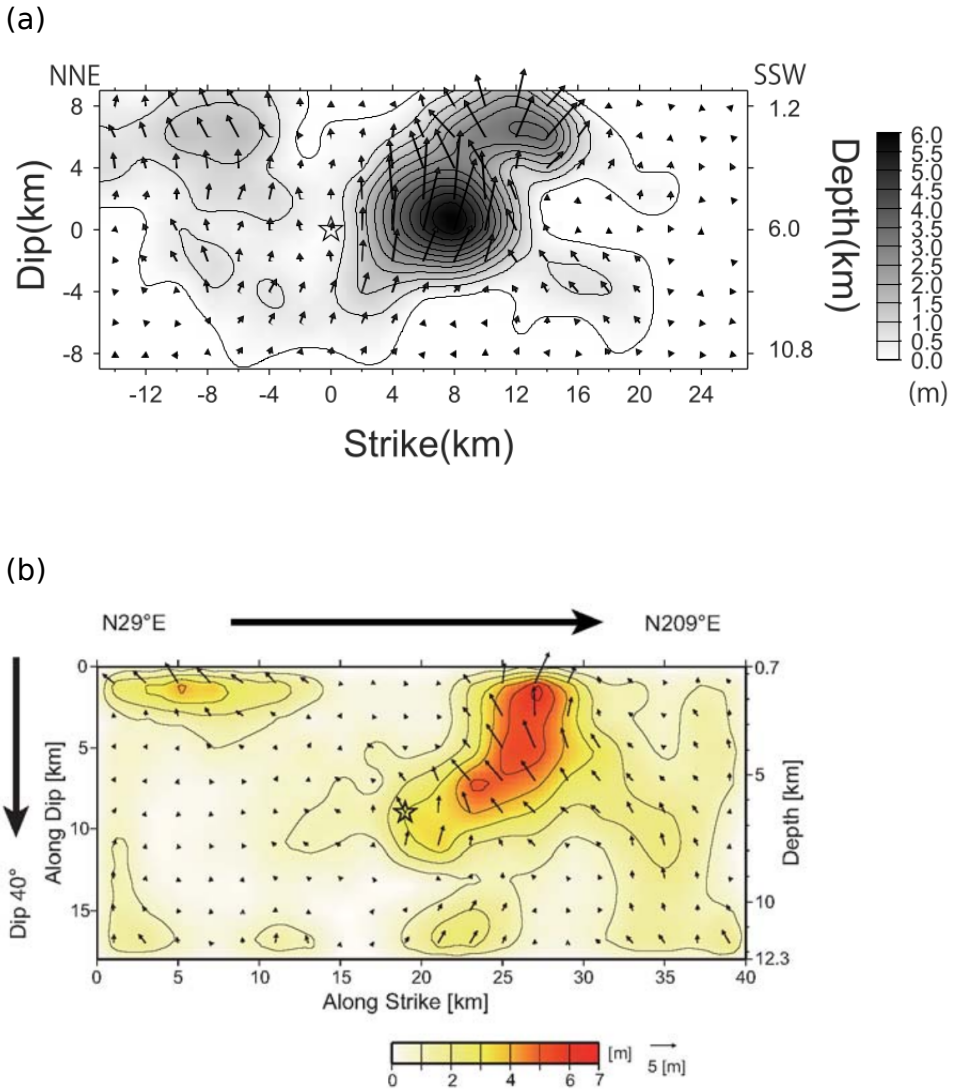

Figure 4.13: Slip distributions obtained from (a) the joint inversion of geodetic and strong motion data by *Yokota et al.* (2009) and (b) the near-source strong-motion inversion by *Suzuki et al.* (2010). Note that the length, the width, and the dip and strike angles of the fault planes are note the same.

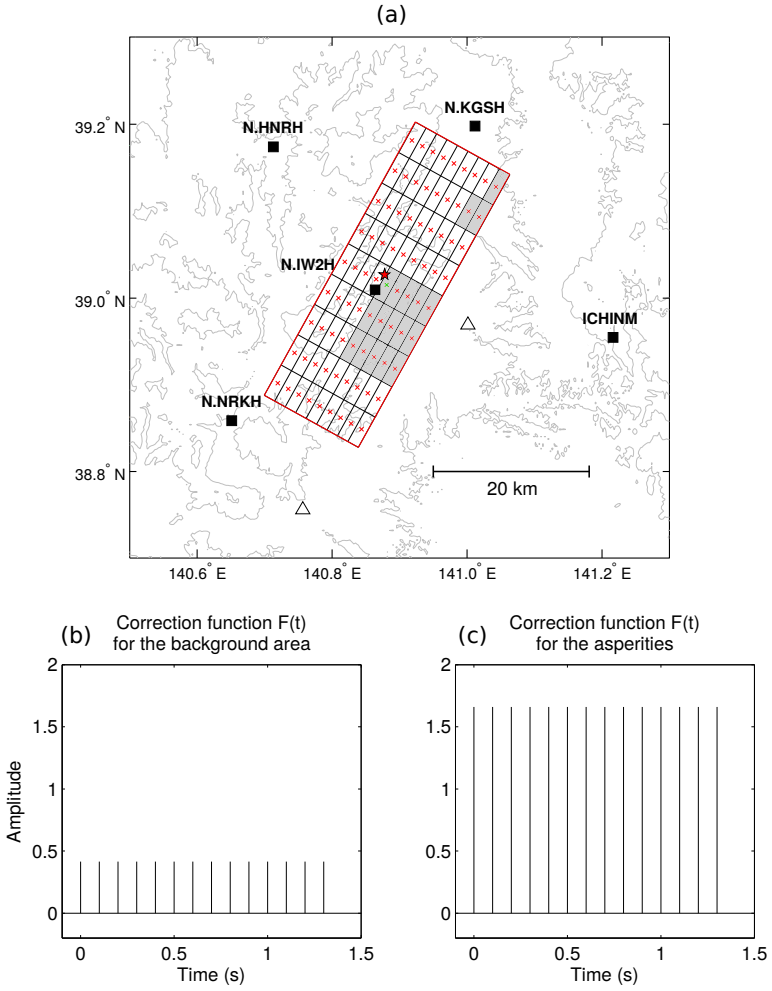

Figure 4.14: (a) Fault plane of the 2008 M_w 6.9 Iwate-Miyagi Nairiku earthquake including asperities (gray subfaults) and the five virtual source stations (black triangles). Correction function ($F(t)$) for the (b) background and (c) asperity subfaults.

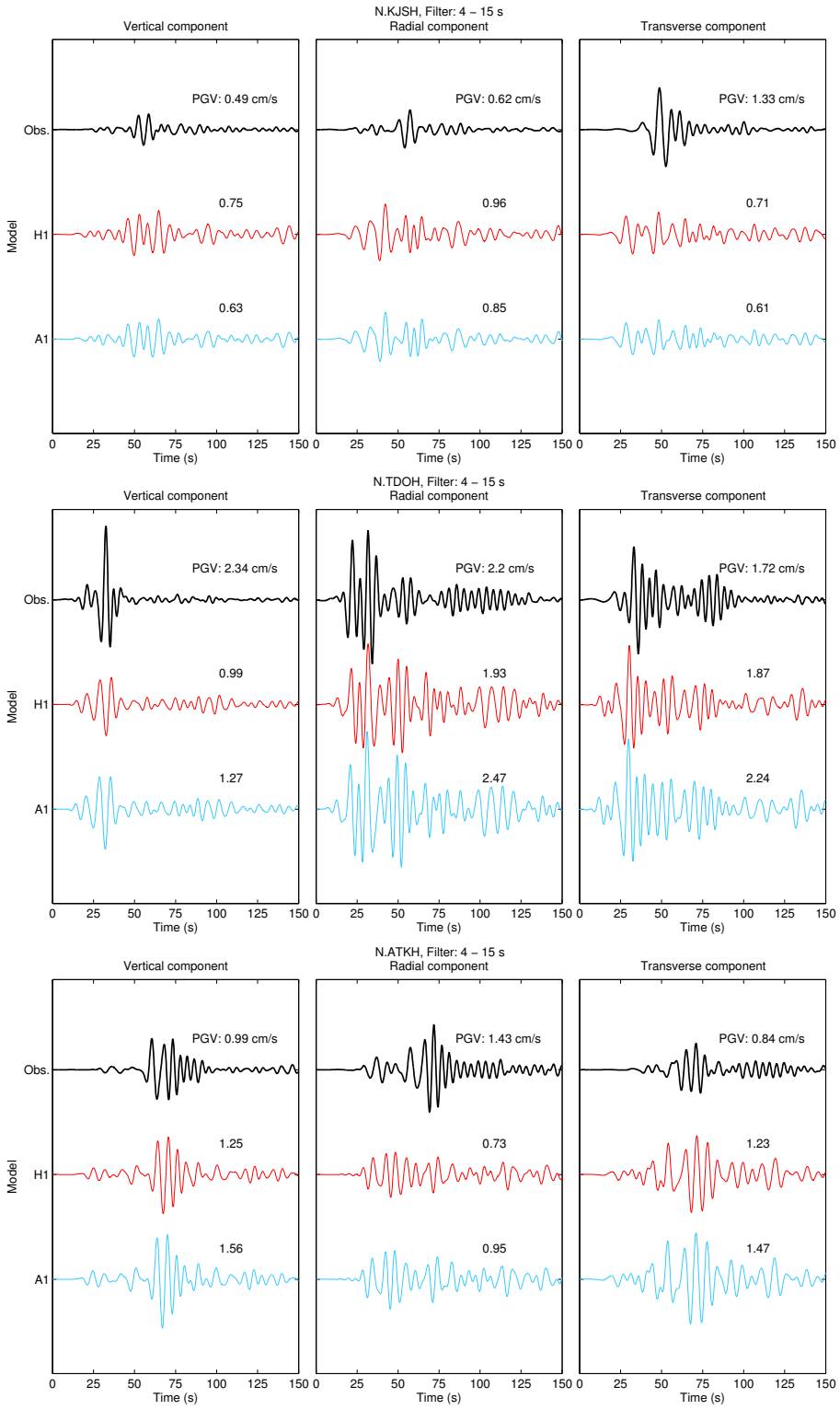

Figure 4.15: Comparison of the (black) observed and simulated waveforms for the 2008 M_w 6.9 Iwate-Miyagi Nairiku earthquake at three stations. The waveforms for the three components are bandpass filtered between 4 and 15 s and the long-period PGV is shown for each waveform.

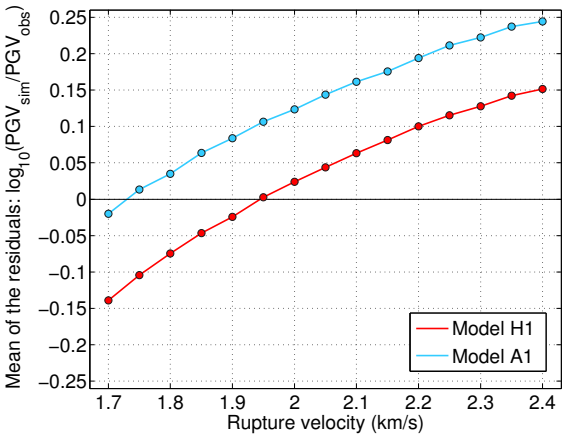

Figure 4.16: Average over three components (e.g., vertical, radial, and transverse) of the mean of the residuals ($\log_{10}(\mathrm{PGV_{sim}}/\mathrm{PGV_{obs}})$ as a function of the rupture velocity for Models H1 and A1.

Chapter 5

Large Subduction Earthquake Scenario in the Kanto Basin: From Source Modeling to Building Motion using the Ambient Seismic Field

5.1 Introduction

Seismic waves generated by earthquakes propagate from the source in all directions throughout the Earth. At a given site on which a building is situated, incoming seismic waves, which are the convolution of the source, path, and site effects, propagate inside the building causing the structure to vibrate. Therefore, it is critical to accurately predict the level of ground shaking that can be generated by future hypothetical earthquakes and determine how buildings will respond to such ground shaking to prevent disaster.

Over the last decade, seismic interferometry became widely used to reconstruct the elastic response of the Earth, which is also called Green's function, between a pair of

seismic stations (*Campillo and Paul*, 2003; *Shapiro and Campillo*, 2004). Several studies demonstrated that Green's functions extracted with the deconvolution method can be used to accurately simulate the long-period ground motions of moderate crustal (*Prieto and Beroza*, 2008; *Denolle et al.*, 2013; *Viens et al.*, 2014) and subduction (*Viens et al.*, 2015) earthquakes. The long-period ground motions generated by large earthquakes ($M_w > 6$), for which a finite rupture needs to be considered, can be also simulated with this technique as shown by *Denolle et al.* (2014a) and in Chapter 4 of this thesis.

The response of a building can also be extracted from the records of seismometers located at different heights of the structure using the deconvolution technique. This method was first applied to earthquake data (*Snieder and Şafak*, 2006; *Kohler et al.*, 2007; *Todorovska and Trifunac*, 2008; *Nakata et al.*, 2013) and then to ambient vibrations continuously recorded by seismic sensors (*Prieto et al.*, 2010; *Nakata and Snieder*, 2014). These studies showed that the *S* wave velocity in the structure, the attenuation of the waves, and the resonance frequencies can be determined from the building responses extracted from both data-set. *Prieto et al.* (2010) also showed that the shaking of buildings can be accurately predicted by convolving the records at the basement of a moderate earthquake with the building response.

The propagation of seismic waves can be significantly affected by local near-surface seismic velocity structures, such as sedimentary basins, that can trap and amplify the incoming waves. The Kanto basin, which is located beneath the Tokyo metropolitan area, is locally deeper than 4 km (Figure 5.1a) and is well known to have resonance periods of 7-10 s (*Kudo*, 1978, 1980; *Mamula et al.*, 1984). The basin is located in a highly seismically active area and is under the constant threat of moderate-to-large earthquakes, such as the M_w 7.9 1923 Kanto earthquake which occurred along the Sagami Trough. To mitigate the effect of future earthquakes on this highly populated area, the dense Metropolitan Seismic Observation network (MeSO-net), which shown in Figure 5.1b, has been deployed (*Kasa-*

hara et al., 2009; *Sakai and Hirata*, 2009). In addition to this network, approximately 120 short-period velocity seismometers have also been deployed in the basin and its surroundings by the National Research Institute for Earth Science and Disaster Prevention (NIED) (*Okada et al.*, 2004; *Obara et al.*, 2005), the Japan Meteorological Agency (JMA), the University of Tokyo, and the Hot Spring Research Institute of Kanagawa Prefecture. Recently, *Denolle et al.* (2014b) and *Viens et al.* (2016) demonstrated that Green's functions extracted between stations of these networks can be used to map the amplification of long-period seismic waves caused by the basin with a very high resolution. *Boué et al.* (2016) further explored the effects of the basin shape on the wave propagation using extracted Green's functions.

In addition to the dense networks deployed in the Kanto basin, several tall buildings of the Tokyo metropolitan area are equipped with three-component seismometers. The Hazawa Tower is one of these tall structures and is located in the Kanagawa prefecture (Figure 5.1a). This telecommunication tower is 57.5 m high and has a cylindrical shape as shown in Figure 5.2a. Strong motion sensors have been installed on the ground level and at 20, 40, and 55.5 m above the ground level (Figure 5.2b). All the sensors record continuous data with a sampling rate of 100 Hz.

In this study, we combine Green's functions extracted between stations in the Kanto basin and finite source modeling to predict the ground motions of a large M_w 6.5 earthquake scenario that could occur along the Sagami Trough. We also extract the impulse response functions of the Hazawa tower from earthquake records and ambient vibrations. We use the tower impulse response functions to study the velocity, attenuation, and frequency content of the waves propagating inside the structure. We finally couple the ground motion simulations with the tower impulse response functions to study the building motions during past moderate earthquakes and the M_w 6.5 earthquake scenario.

5.2 Methods

5.2.1 Ground Motion Simulation of a Moderate M_w 4.1 Earthquake

We extract Green's functions between seismic stations located on the southern edge of the basin, which are considered as virtual sources, and the MeSO-net stations inside the Kanto basin (Figure 5.1). Deconvolutions are computed using Equation 2.1 after removing earthquakes from the data recorded in October 2014 and integration of the MeSO-net data to retrieve the corresponding velocity.

A shallow M_w 4.1 earthquake occurred on 21 March 2011 in the Hakone region. We use the OK.KOM station, which is located in the vicinity of the earthquake hypocenter, as the virtual source and three MeSO-net stations in the Kanto basin as receivers (Figure 5.1b). The amplitude of extracted Green's functions are calibrated with the earthquake records following *Viens et al.* (2014). The distance between the virtual source and each receiver station is slightly different from the hypocenter-receiver distance due to the hypocenter location at 5 km depth. To account for this difference, we shift the arrival time of the earthquake seismic waves by the time corresponding to the ratio of the distance difference over a theoretical surface wave velocity that is set to 3 km/s. Observed and simulated waveforms are shown in Figure 5.3a after being bandpass filtered between 1 and 10 s. Note that the calibrated Green's functions are tapered to smooth the waves traveling faster than 3 km/s. For each station, both waveforms agree well in the time domain in terms of maximum velocity and strong motion duration. Fourier spectra of the signals (Figure 5.3b) show that simulated and observed waveforms have a similar frequency content in the frequency range of 0.1 to 1 Hz (1 to 10 s). The overestimation observed on the vertical component for the E.JDJM station, which is not observed for the two other stations, is probably caused by a problem in the ambient seismic field data recorded at the station that affects the deconvolution results.

5.2.2 Earthquake Scenario along the Sagami Trough

The subduction of the Philippine Sea plate beneath the Kanto basin makes the area under the threat of subduction events such as the 1923 M_w 7.9 Kanto earthquake. To simulate the ground motions of a large M_w 6.5 subduction earthquake scenario that could occur in this area, we follow the methodology that we presented in Chapter 4 of this thesis. To determine the size of the earthquake scenario, we use the empirical relations developed by *Blaser et al.* (2010) for reverse faulting subduction earthquakes. The size of the M_w 6.5 earthquake scenario, which has a seismic moment of 6.31×10^{18} Nm, is determined as

$$\log_{10}(L) = -2.81 + 0.62 \times M_w \tag{5.1}$$

$$\log_{10}(W) = -1.79 + 0.45 \times M_w. \tag{5.2}$$

These equations give a length (L) and a width (W) equal to 22.9 and 16 km, respectively. We set the location of the fault plane of the earthquake scenario on the shallow part of the Sagami Trough close to the western edge of the 1923 Kanto earthquake fault plane (Figure 5.4). We focus on this area because of the large number of seismic stations that can be used as virtual sources and the occurrence of the previously described M_w 4.1 earthquake that is used to calibrated Green's function amplitudes.

Scaling relations between small and large earthquakes have been developed by *Kanamori and Anderson* (1975) and can be summarized as $M_0/m_0 = N^3$. The seismic moment ratio of the observed M_w 4.1 event and the M_w 6.5 earthquake scenario gives that N, which is the ratio of the fault dimensions between the two earthquakes, is equal to 17. Therefore, we divide the fault plane into 17×17 subfaults having a length l and a width w equal to 0.98 and 0.8 km, respectively. As in Chapter 4, we follow the empirical relation between slip duration and seismic moment developed by *Somerville et al.* (1999) to determine the rise time of the M_w 4.1 event (τ), and obtain 0.05 s. The rise time of the large event

(T) is set to 0.8 s, which corresponds to N times the rise time of the small event. As the sampling rate of the waveforms is 10 Hz, the correction function $F(t)$ is set as a sum of 8 Dirac delta functions that have their amplitudes calibrated for the integral of $F(t)$ from 0 to T to be equal to N. The rupture velocity is set to 2.7 km/s and the Green's functions at each subfault are summed up following Equation 4.7 of Chapter 4 using the subfault located close to the hypocenter of the M_w 4.1 event as starting point.

The simulated waveforms at the E.BKKM, E.JDJM, and E.MZPM stations, which are located close to the Hazawa Tower, are shown in Figure 5.5. For the uniform source model, we obtain similar PGVs for the three stations and each component in the period range of 1 to 10 s. PGVs simulated for the two horizontal components are 2 to 3 times larger than those simulated for the vertical component.

5.2.3 Extraction of Tower Impulse Response Functions (TIRFs)

Seven accelerometers equipped with three-component sensors recording continuous waveforms have been installed in the Hazawa Tower. The acceleration records are first integrated once to retrieve the corresponding velocity and are bandpass filtered between 0.1 and 10 s. Figure 5.6a shows the velocity records of a M_w 5.0 earthquake that occurred on 12 September 2015 beneath the Tokyo Bay at a depth of 62 km (F-net of NIED solution). Long-period seismic waves are clearly amplified on the top floor of the tower. The Fourier spectrum of the waveforms shows that the tower has its primary and secondary resonance periods at 1.5 s (0.68 Hz) and 0.23 s (4.35 Hz), respectively. For this event, the amplitude of the fundamental mode is larger for the E-W component than for the N-S component, whereas the opposite is observed for the first higher-mode.

We extract the tower impulse response functions (TIRFs) from the records of this earthquake using the station located on the ground level (GL) as the virtual source as

$$\mathrm{TIRF}_{jj}(z, \mathrm{GL}, t) = \mathfrak{F}^{-1}\left(\frac{\hat{u}_j(z,\omega)\,\hat{u}_j^*(\mathrm{GL},\omega)}{\{|\hat{u}_j(\mathrm{GL},\omega)|\}^2 + \xi}\right), \tag{5.3}$$

where z is the height where the receiver sensor is located. t is the time, ω is the frequency, * is the complex conjugate, $\mathfrak{F}^{-1}$ is the inverse Fourier transform, and $\hat{u}_j$ is the Fourier transform of the velocity waveform computed with the multitaper method for one of the two horizontal component j (e.g., N-S or E-W). The denominator term is smoothed, which is represented by $\{\}$, and a water level ξ (1% of the average spectral power) is added.

We show the extracted waveforms that are bandpass filtered between 0.1 to 10 s in Figure 5.6c. The fundamental and first higher modes of the building clearly dominate the TIRFs in this period range. For the two resonance periods, we use the method proposed by *Snieder and Şafak* (2006) to determined the quality factor Q of the building. From this quality factor, the attenuation of the waves in the building ($1/Q$) can be also easily computed. We bandpass filter the TIRFs around the two resonance periods, compute the envelope of the signals, and show the neperian logarithm of the envelopes in Figure 5.7. The amplitude decay with time (slope) is directly related to the attenuation of seismic waves in the building as $Q = \pi f/(\text{slope})$, where f is the resonance frequency. We fit the waveforms showed in Figure 5.7 with straight lines (in the least-squares sense) and summarized the different values of the slopes in Table 5.1 for the fundamental and first-higher resonance periods. As the slopes have similar values for each height, we compute the quality factors from the average values of the slopes and show the averaged Q values in the bottom line of Table 5.1. For this earthquake, the attenuation ($1/Q$) is larger for the N-S component of the fundamental mode and for the E-W component of the first higher mode. As observed by *Nakata et al.* (2013), the attenuation is directly related to the amplitude of the resonant waves. We showed in Figure 5.6b that the amplitude of the fundamental mode is larger for E-W component than for the N-S component for

this event. This feature leads to less attenuation on the *E-W* component than on the *N-S* component for the fundamental mode. As the Tower has a cylindrical shape, the response on the *N-S* and *E-W* components is expected to be the same. One possible explanation of the difference between the two components is the difference of ground stiffness. Indeed, the construction of the highway located on the eastern side of the Tower can have made the soil less compact on the *E-W* axis and create this non-uniform response.

To obtain average values of the attenuation in the building, we stack the TIRFs extracted from the earthquakes that are listed in Table 5.2 and showed in Figure 5.8. The stacked TIRFs are shown in Figure 5.9. The waveforms of the *N-S* and *E-W* components of the TIRFs are more similar after stacking over several events, even if the fundamental mode is still more excited on the *E-W* component than on the *N-S* component. We also compute the logarithm of the envelopes in Figure 5.10 and find that the values of the slope are also more similar for the two components (Table 5.3).

We also extract the TIRFs from the ambient vibrations recorded in the building. One hour of these ambient vibrations is shown in Figure 5.11a for the two horizontal components of the sensors located in the tower. As for earthquake records, the amplitude of ambient vibrations is stronger for the seismometer located on the top of the tower. The Fourier analysis of the waveforms also shows the same resonance peaks as those found from earthquake records (Figure 5.11b). As we only have 14 h of ambient vibration records, we divide the data-set into 4 min time series, compute the deconvolutions using the station located on the ground level as the virtual source, and stack the results as

$$\mathrm{TIRF}_{jj}(z, \mathrm{GL}, t) = \sum_{k=1}^{K} \mathfrak{F}^{-1} \left(\frac{\hat{u}_j(z,\omega)\, \hat{u}_j^*(\mathrm{GL},\omega)}{\{|\hat{u}_j(\mathrm{GL},\omega)|\}^2 + \xi} \right). \tag{5.4}$$

where K is the number of 4 min time series (210 for the 14 h of ambient vibrations). The other variables are the same as in Equation 5.3.

The building responses reconstructed from the ambient vibrations recorded by the hor-

izontal components are shown in Figure 5.12. The fundamental and first higher modes of the building also clearly dominate the TIRFs in the period range of 0.1 and 10 s (Figure 5.12a). A narrower filtering between 0.1 and 1 s (Figure 5.12b) shows that the amplitude of the first-higher mode (0.23 s) is almost constant with the height. However, the fundamental mode (1.5 s) becomes larger with the height as shown in Figure 5.12c. The wave velocity of the first higher mode can be easily determined and is equal to approximately 400 m/s. However, the waveforms of the fundamental mode have simultaneous arrivals throughout the building height. This zero-phase shift, also pointed out by *Kohler et al.* (2007) for earthquake data, might result from processing artifacts and from the fact that all heights of a building are in phase when the structure is dominated by a single mode.

We also estimate the quality factor of the TIRFs using the method previously described. While Q values of the first higher mode are quite similar to the ones found from the TIRFs computed from earthquake data, Q values for the fundamental mode are much higher for the TIRFs computed from ambient vibrations than those computed from earthquakes. *Nakata and Snieder* (2014) showed that from a theoretical point of view, the decay of the amplitude does not only depend on the intrinsic attenuation in the building for the ambient vibration deconvolution, but also from losses due a coupling with the ground. This feature might be one explanation of the difference between the different values of the quality factor and more work is needed to understand this relationship.

We finally compute the deconvolution using the station located on the top floor as the virtual source (Figure 5.14). The response of the building becomes simpler than when the station located on the ground level is used as the virtual source, with only one upgoing wave and one downgoing wave as first shown by *Snieder and Şafak* (2006). Therefore, it is easier to determine the wave velocity inside the building, which is equal to approximately 400 m/s.

5.3 From Earthquake Source to Building Motion

Prieto et al. (2010) showed that the motions of a building generated by a moderate earthquake can be computed by convolving the Earth ground motions with the building impulse response functions retrieved from ambient vibrations. For the Hazawa Tower, this convolution can be written as

$$\mathrm{TM}_{\mathrm{av}}(z,t) = V_{\mathrm{eq}}(\mathrm{GL},t) * \mathrm{TIRF}_{\mathrm{av}}(z,\mathrm{GL},t), \tag{5.5}$$

where $V_{\mathrm{eq}}(\mathrm{GL},t)$ is the recorded earthquake at the ground level. $\mathrm{TIRF}_{\mathrm{av}}(z,\mathrm{GL},t)$ is the tower impulse response function in the time domain t computed from ambient vibrations (av), using the station on the ground level as virtual source and stations at different heights z as receivers. The convolution, which is denoted by the asterisk $*$, gives the simulated tower motion in velocity $\mathrm{TM}_{\mathrm{av}}(z,t)$ at each height z.

The convolution of the recorded Earth ground motions with the tower impulse response function computed from the stack of earthquakes ($\mathrm{TIRF}_{\mathrm{seq}}(z,\mathrm{GL},t)$) can also be computed as

$$\mathrm{TM}_{\mathrm{seq}}(z,t) = V_{\mathrm{eq}}(\mathrm{GL},t) * \mathrm{TIRF}_{\mathrm{seq}}(z,\mathrm{GL},t), \tag{5.6}$$

where $\mathrm{TM}_{\mathrm{seq}}(z,t)$ is the simulated tower motion in velocity at height z.

In the following, we only focus on the fundamental mode of the building by bandpass filtering all the waveforms between 1 and 10 s. We first convolve the records at the ground level of the tower of the M_w 5.0 earthquake, which occurred beneath the Tokyo Bay, with the TIRFs extracted from the stack of the earthquakes (e.g., Figure 5.9c) and ambient vibrations (e.g., Figures 5.12c). For each component, the TIRF of the ground level station is the deconvolution of the waveform by itself, which leads to a Dirac delta function. Therefore, the convolution of the Dirac delta function with the recorded waveform at

the ground level should give the same waveform. However, the water level added to the denominator of the deconvolution combined to the filtering of the TIRFs leads to a small underestimation of the amplitude. To account for this underestimation, we multiply the amplitude of the TIRF at the ground level by a factor to retrieve simulated waveforms having similar amplitudes to the observed ones. The TIRFs for the other heights are also multiplied by this empirical factor that is equal to 1.6.

The simulated building motions using TIRFs extracted from the stack of earthquakes, which are shown in Figure 5.15a, have similar amplitudes and are in phase with the recorded waveforms at each height. On the other hand, the simulated building motions using TIRFs extracted from the ambient vibrations (Figure 5.15b) have their seismic waves arriving before the observed ones. This is caused by the zero phase shift of the TIRFs extracted from ambient vibrations for the fundamental mode, as shown in Figure 5.12. Despite the fact that observed and simulated waveforms are not in phase, their amplitudes are very similar. As both simulations give tower motions that reproduce quite well the observed ones, we choose to only use the TIRFs computed from ambient vibrations in the following to obtain simulations that are fully computed from the ambient seismic field.

5.3.1 Prediction of the Tower Motion During the 2011 M_w 4.1 Hakone Earthquake

We showed in Figure 5.3 that calibrated Green's functions agree well with the records of the M_w 4.1 earthquake that occurred in March 2011 in the Hakone region in the period range of 1 to 10 s for the three MeSO-net stations located close to the Hazawa Tower. To obtain building motion fully simulated with the ambient seismic field, the next step is to convolve the amplitude calibrated Green's function instead of earthquake records with the TIRFs as

$$\mathrm{TM}_{\mathrm{sim}}(z,t) = V_G(\mathrm{GL},t) * \mathrm{TIRF}_{\mathrm{av}}(z,\mathrm{GL},t), \tag{5.7}$$

where $\mathrm{TM}_{\mathrm{sim}}(z,t)$ is the tower motion in velocity at height z computed using the calibrated Green's function at the ground level $V_G(t)$ as input ground motion. As this earthquake occurred before the installation of the seismometers in the Hazawa Tower, we do not have the records of this event. Moreover, the short length of the ambient seismic field time series recorded at the ground level of the tower (e.g., 14 h) does not allow to extract Green's functions between the virtual source and the station located on the ground level of the Hazawa Tower. Therefore, we suppose that the calibrated Green's function at the three stations located close to the tower (e.g., the E.BKKM, E.JDJM, and E.MZPM stations) can be used as input waveforms of the tower.

To confirm that the three MeSO-net stations can be used as input ground motions in the period range of 1 to 10 s, we compare the waveforms recorded at the station located on the ground level of the tower, and the ones recorded at the three MeSO-net stations for the 2015 M_w 5.0 earthquake which occurred beneath Tokyo Bay. The waveforms, which are shown in Figure 5.16, are quite similar in the period range of 1 to 10 s. The main difference is the long-period peak on the N-S component that is observed at the ground level of the tower, but not clearly observed at the MeSO-net stations. This difference might be caused by the incapacity of the sensor located on the ground level of the tower to accurately record long-period seismic waves. Nevertheless, such long-period peak does not impact much the tower motion because of its period (e.g., 3 s) that is approximately twice longer than the fundamental period of the tower. We convolve the waveforms of the M_w 5.0 earthquake recorded at the three MeSO-net stations with the $\mathrm{TIRF}_{\mathrm{av}}$, and show the results in Figure 5.17. Note that we do not shift the earthquake waveforms to account for the difference of location between the MeSO-net stations and the Hazawa Tower, and only discuss the amplitude differences. The best fit in terms of amplitude is found

when the records at the E.BKKM and E.JDJM stations are used as input motions. The tower motion computed with the records at the E.MZPM station slightly overestimates the motion on the E-W component but better reproduce the amplitude on the N-S component. Nevertheless, these results show a good agreement with the observed tower motions even when the ground motions recorded at the MeSO-net stations are used as input ground motions in the period range of 1 to 10 s.

We showed that earthquake ground motions recorded by the three MeSO-net stations can be used as input motions to study the tower motion. The next step is to study the effect of the calibrated Green's functions if used as input motions. We show in Figures 5.18–5.20 the simulated tower motions at each height computed from the convolution of both the records of the 2011 M_w 4.1 Hakone earthquake and the calibrated Green's function waveforms, with the TIRFs. For the three MeSO-net stations, the simulated building motion using the extracted Green's functions as inputs agree well with the one computed from the records of earthquakes in terms of maximum velocity and strong motion duration. Moreover, the Fourier analysis of the waveforms shows a similar excitation level of the fundamental mode of the tower for each component and each height. The similar shapes of the Fourier spectra over the period range of 1 to 10 s indicates that the ambient seismic field can be used to simulate the whole source process of a moderate earthquake from the source to building motions.

5.3.2 Prediction of the Tower Motion During a M_w 6.5 Earthquake Scenario

To predict the tower motion in case of the M_w 6.5 earthquake scenario previously described, we use the waveforms shown in Figure 5.5 as input ground motions. As the sampling rate of these waveforms is 10 Hz, we resample the waveforms to 100 Hz. The

simulated ground motions are finally convolved with the TIRFs after being bandpass filtered between 1 and 10 s. The tower motions during this hypothetical event are presented in Figure 5.21 for the two horizontal components using the simulated waveforms at the three MeSO-net stations. The simulated building motions are quite similar for the simulated waveforms at the three stations. As expected, the motion at the top floor of the tower is much higher than during the smaller event presented previously. Moreover, the ground motions with periods longer than 4 s, which dominates the ground motion simulations, are filtered by the convolution with the building because such periods are too large to affect the tower. Such small impact of the long-period waves as been also observed during the smaller event presented previously and such waves are expected to do not impact much a structure that has a fundamental resonance period of 1.5 s. In the following section, we further discuss these results more in details.

5.4 Discussion

Viens et al. (2016) showed that the calibrated Green's functions can simulate the ground motions of moderate M_w 4-5 class earthquakes in the Kanto basin in the period range of 1 to 10 s for the vertical component. In this study, we show that the Fourier spectra of the calibrated Green's functions for the three components agree well with the observed ones of the M_w 4.1 earthquake that occurred in the Hakone region. However, such comparison should be estimated for more stations ensure that the ground motions of the two horizontal components can also be simulated in the period range of 1 to 10 s in the Kanto basin. Moreover, the studies of *Denolle et al.* (2014a) and Chapter 4 of this thesis only showed that the finite source modeling combined with extracted Green's functions is feasible at periods longer than 3 and 4 s, respectively. Therefore, more work is needed to estimate the accuracy of the simulated waveforms for a large event in the period range of 1 to 10 s.

The TIRFs used to simulate the building motions are extracted from 14 h of ambient vibrations. *Prieto et al.* (2010) showed that a few days of records are generally required to retrieve stable building response functions. Therefore, the extracted building responses used in this study might be slightly different from the stable ones. This feature is probably one of the reasons of the mismatch between the simulated and observed building motions that we computed. Moreover, the TIRFs extracted from ambient vibrations and moderate earthquakes allows to investigate the parameters of a structure in a linear regime (*Prieto et al.*, 2010). In case of a large seismic solicitation, the response of a structure can become non-linear. At long-periods, the effect of non-linearity is usually not significant. However, the implementation of this effect to the linear response is an important future research direction.

In this study, we only investigated the effect of seismic waves on the fundamental mode of the Hazawa Tower. However, the building motion caused seismic waves is a combination of all the modes. Moreover, we showed in Figure 5.6 that the first-higher mode of the tower can be excited even more than the fundamental mode. Therefore, the simulated building motion for the earthquakes presented in this study is not complete and needs to be further investigated.

A M_w 4.1 earthquake occurred on 25 October 2015 in the Yamanashi region which is close to the source area of the simulated M_w 6.5 scenario earthquake. During this event, the tower was already shaking before the arrival of seismic waves as shown in Figure 5.22. Such shaking, which is caused by the wind, mainly excited the fundamental mode of the tower. Moreover, the earthquake did not really change the motion of the fundamental mode of the tower. As it is difficult to separate the effect of the wind to the effect of the shaking due to the earthquake, we did not use this event to validate the method presented in this Chapter. However, the effect of strong wind coupled with the ground motions caused by a large earthquake could cause even more, or less, shaking of

the tower. Therefore, such coupling needs also to be addressed in future studies.

5.5 Conclusions

We showed that Green's functions extracted from the ambient seismic field can be used to simulate a M_w 4.1 earthquake which occurred in the Hakone region. We constructed a finite source model of a M_w 6.5 earthquake scenario that could occur on the shallow part of the Sagami Trough based on scaling relations between small and large earthquakes. We combined the finite source model and the extracted Green's functions to simulate the ground motions of this earthquake scenario in the Kanto basin.

We extracted the response of the Hazawa Tower using earthquake and ambient vibration waveforms recorded at different heights of the structure. We first determined that the tower has its fundamental and first-higher modes equal to 1.5 s and 0.23 s, respectively. From the tower impulse response functions, we also determined that seismic waves propagate with a velocity of approximately 400 m/s in the structure. The quality factor (Q) of the fundamental and first-higher modes in the tower is more difficult to estimate because of its dependency to the input motion. The Q value computed from the TIRFs retrieved from ambient vibrations are quite different for the fundamental mode, which might be caused by a coupling with the ground of the response.

We finally convolved the TIRFs extracted from ambient vibrations to the ground motion records of a M_w 5.0 earthquake that occurred beneath the Tokyo Bay in March 2015. The simulated tower motions agree well with the observed ones for this event for the fundamental mode of the tower. We then predicted the fundamental mode tower motion for the M_w 4.1 earthquake that occurred in the Hakone region before the installation of the sensors in the Hazawa Tower. Using the recorded and simulated waveforms of this event at three MeSO-net stations located in the vicinity of the tower, we computed the tower

motion for this event. Both waveforms agree quite well in terms of amplitude and strong motion duration. We finally computed the tower motion that could occur during the M_w 6.5 earthquake scenario. We found that PGVs larger than 40 cm/s could be recorded at the top floor of the tower in case of such event.

Table 5.1: Slope values of the fundamental and first-higher resonance periods and average values of the factor Q computed from the TIRFs recovered from an M_w 5.0 earthquake that occurred in September 12, 2015 beneath the Tokyo Bay. The height of the sensors is taken from the ground level.

Sensor	Fundamental		First-higher	
	N-S	E-W	N-S	E-W
Top (60 m)	-0.1255	-0.0563	-0.2032	-0.2582
40 m	-0.1138	-0.0506	-0.1922	-0.2702
20 m	-0.1189	-0.0502	-0.1901	-0.2712
Average Q	18.08	41.23	69.99	51.24

Table 5.2: Centroid Moment Tensor Solutions of the Earthquakes shown in Figure 5.8.

Date	Latitude	Longitude	Depth	M_w	Approximate location
2015/02/07, 15:19:06.03	35.7888	140.0698	68	4.3	N Chiba Pref.
2015/05/13, 06:12:58.45	38.8628	142.1502	44	6.8	E Off Miyagi Pref.
2015/05/25, 14:28:10.37	36.0543	139.6387	59	5.2	E Saitama Pref.
2015/05/30, 20:23:02.28	27.8608	140.6825	680	7.9	W Off Ogasawara
2015/07/10, 01:15:13.83	36.0687	139.8530	50	4.4	SW Ibaraki Pref.
2015/09/12, 05:49:07.15	35.5545	139.8292	62	5.0	Tokyo Bay region

Table 5.3: Slope values of the fundamental and first-higher resonance periods and average values of the factor *Q* computed from the TIRFs recovered from the stack of the earthquakes listed in Table 5.2.

Sensor	Fundamental		First-higher	
	N-S	E-W	N-S	E-W
Top (60 m)	-0.1143	-0.0827	-0.1578	-0.2073
40 m	-0.1055	-0.0781	-0.1444	-0.2057
20 m	-0.1036	-0.0768	-0.1437	-0.2042
Average Q	20.04	27.26	91.90	66.39

Table 5.4: Slope values of the fundamental and first-higher resonance periods and average values of the factor *Q* computed from the TIRFs recovered from ambient vibrations.

Sensor	Fundamental		First-higher	
	N-S	E-W	N-S	E-W
Top (60 m)	-0.0223	-0.0170	-0.1934	-0.1528
40 m	-0.0193	-0.0166	-0.1936	-0.1587
20 m	-0.0187	-0.0163	-0.1842	-0.1578
Average Q	107.4496	129.7970	71.7391	87.3000

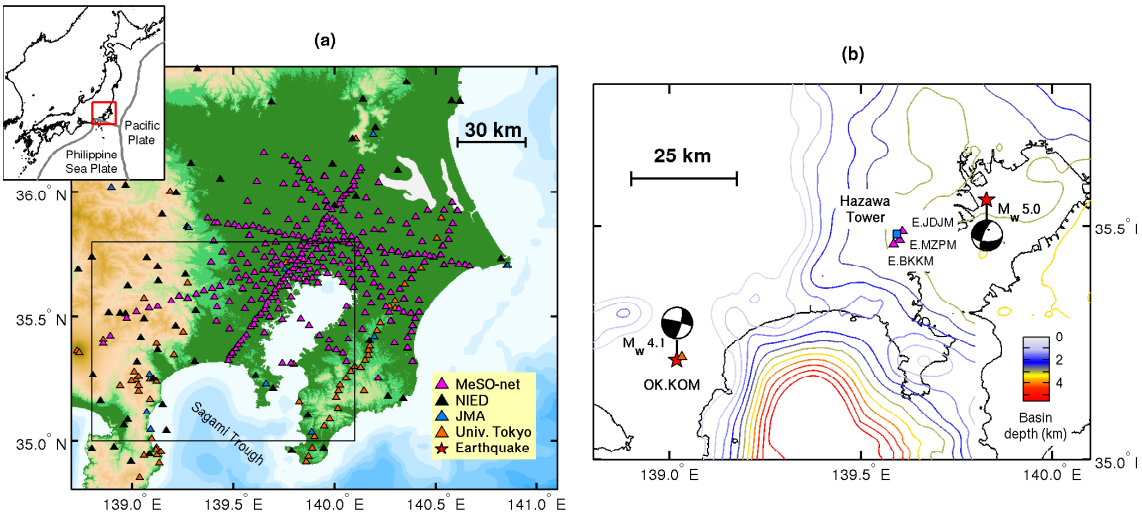

Figure 5.1: Topographic map of the Kanto basin including the MeSO-net (purple triangles), Hi-net (black triangles), JMA (blue triangles), and University of Tokyo (orange triangles) stations. (b) Zoomed region of the rectangle shown in (a). Five hundred meters spaced basin depth contours determined from the JIVSM (*Koketsu et al.*, 2008, 2012) are shown by the colored lines and coastlines are represented by the black lines. The location of the Hazawa Tower is indicated by the blue square and the closest three MeSO-net stations are shown by the purple triangles. The location of the M_w 4.1 which occurred in 2011 in the Hakone is also indicated.

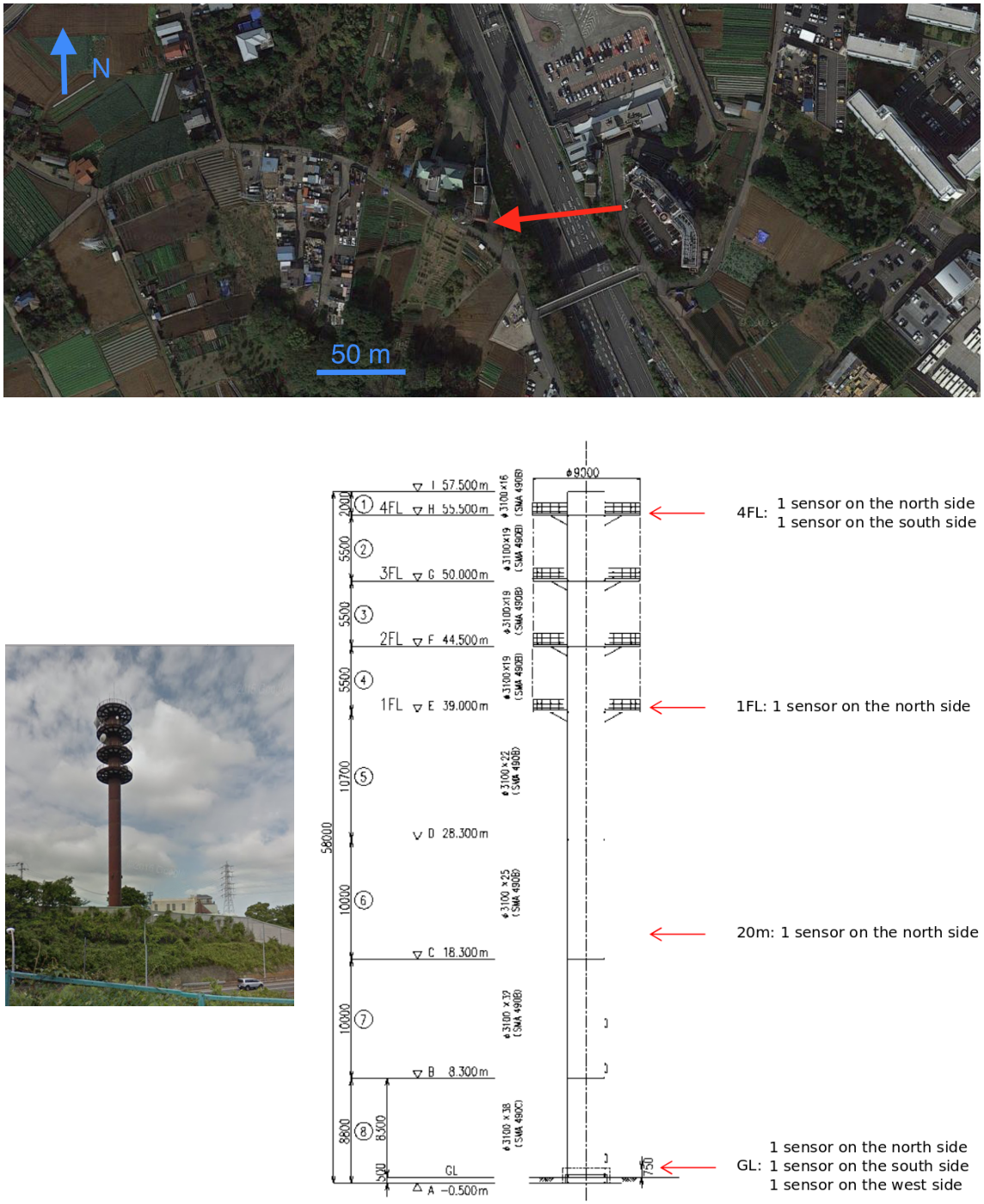

Figure 5.2: (Top) Google Maps view of the Hazawa Tower. The arrow is drawn from the place where the picture of the tower shown below is taken, to the tower. (bottom left) Picture of the Hazawa Tower (from Google Maps - street view). (Bottom right) Dimension and shape of the Hazawa tower. The location of the 7 seismometers is also indicated.

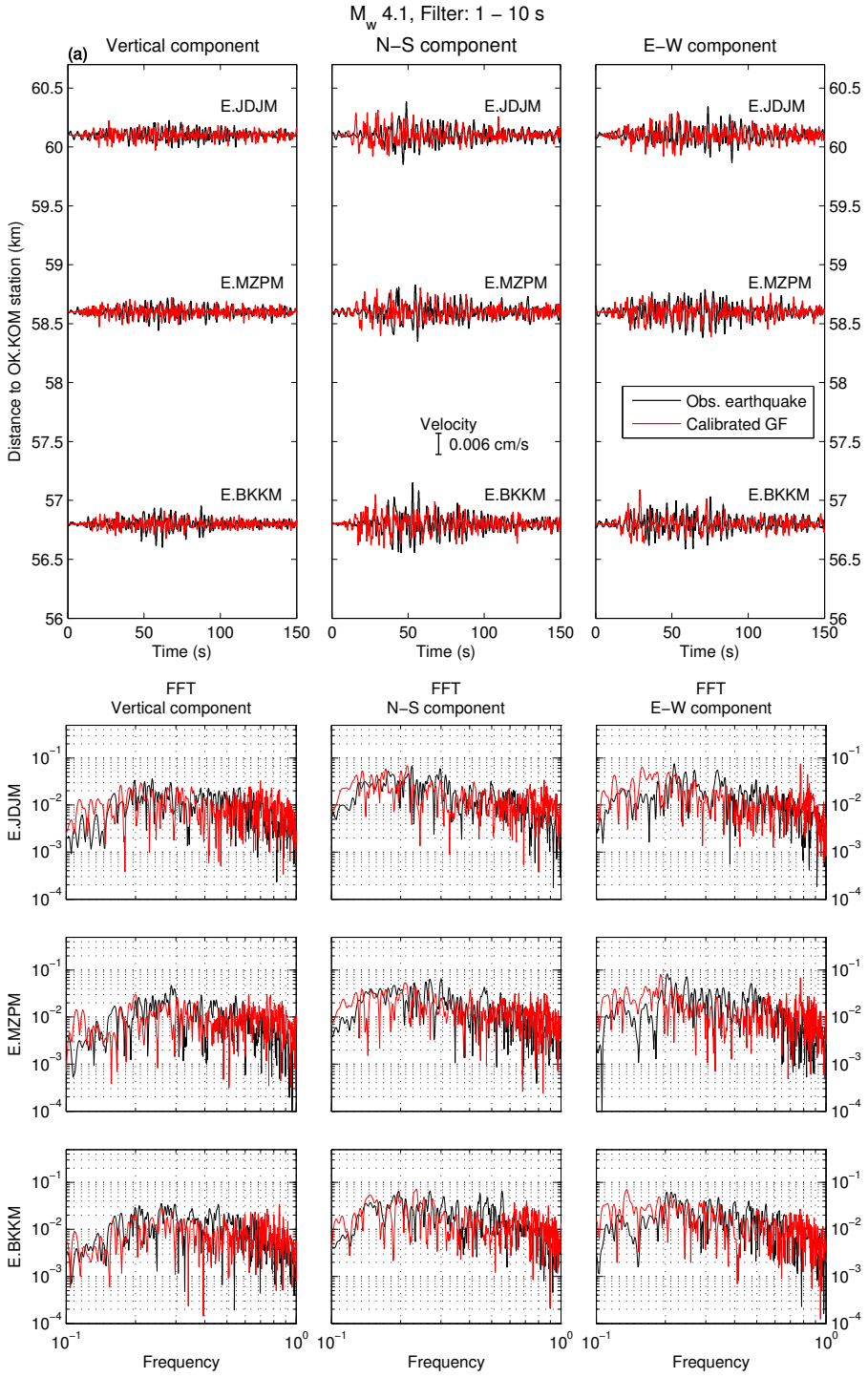

Figure 5.3: (a) Records of the M_w 4.1 earthquake (black lines) and calibrated Green's functions (red lines) for the three stations located in the vicinity of the Hazawa Tower shown in Figure 5.1b. Waveforms are shown as a function of the distance from the virtual source (OK.KOM) for the three components. (b) Fourier transform of the observed (black) and simulated (red) waveforms for the three stations and the three components.

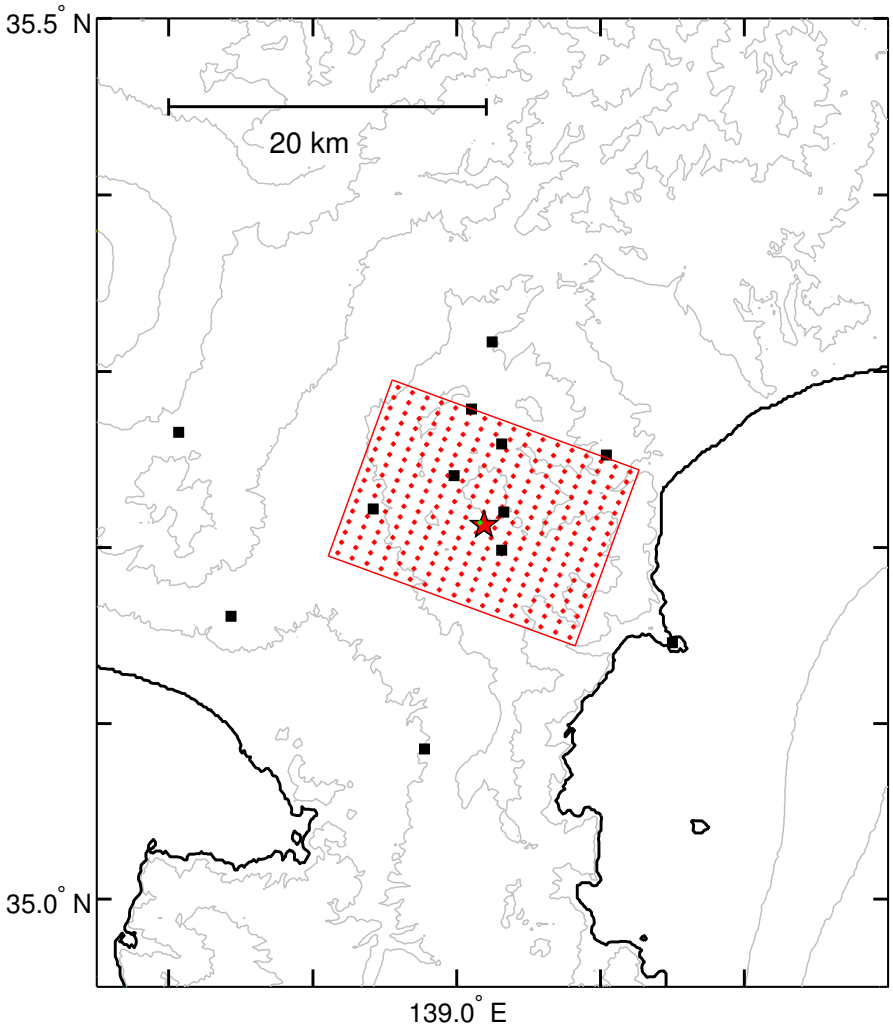

Figure 5.4: Source area of an hypothetical M_w 6.5 including the 11 stations that are used as virtual sources (black squares). The center of each subfault is indicated by a red asterisk and the rupture starts from the subfault indicated by the green asterisk. The location of the M_w 4.1 earthquake is indicated by the star.

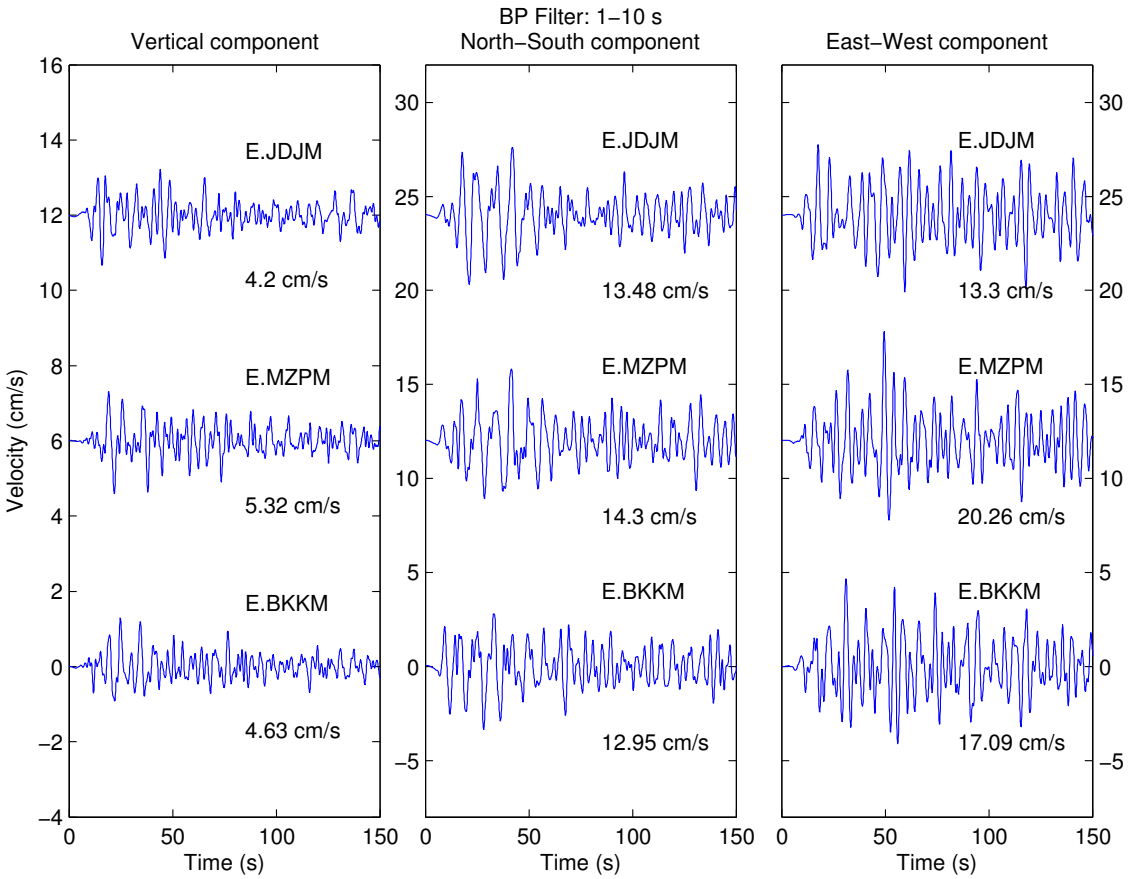

Figure 5.5: Simulated waveforms of the M_w 6.5 earthquake scenario at the E.BKKM, E.MZPM, and E.JDJM stations. The waveforms are bandpass filtered between 1 and 10 s and are shown from left to right for the vertical, *N-S*, and *E-W* components. The name of the stations and the PGVs are also indicated for each trace. Note that the velocity scale is different between the vertical and the two horizontal components.

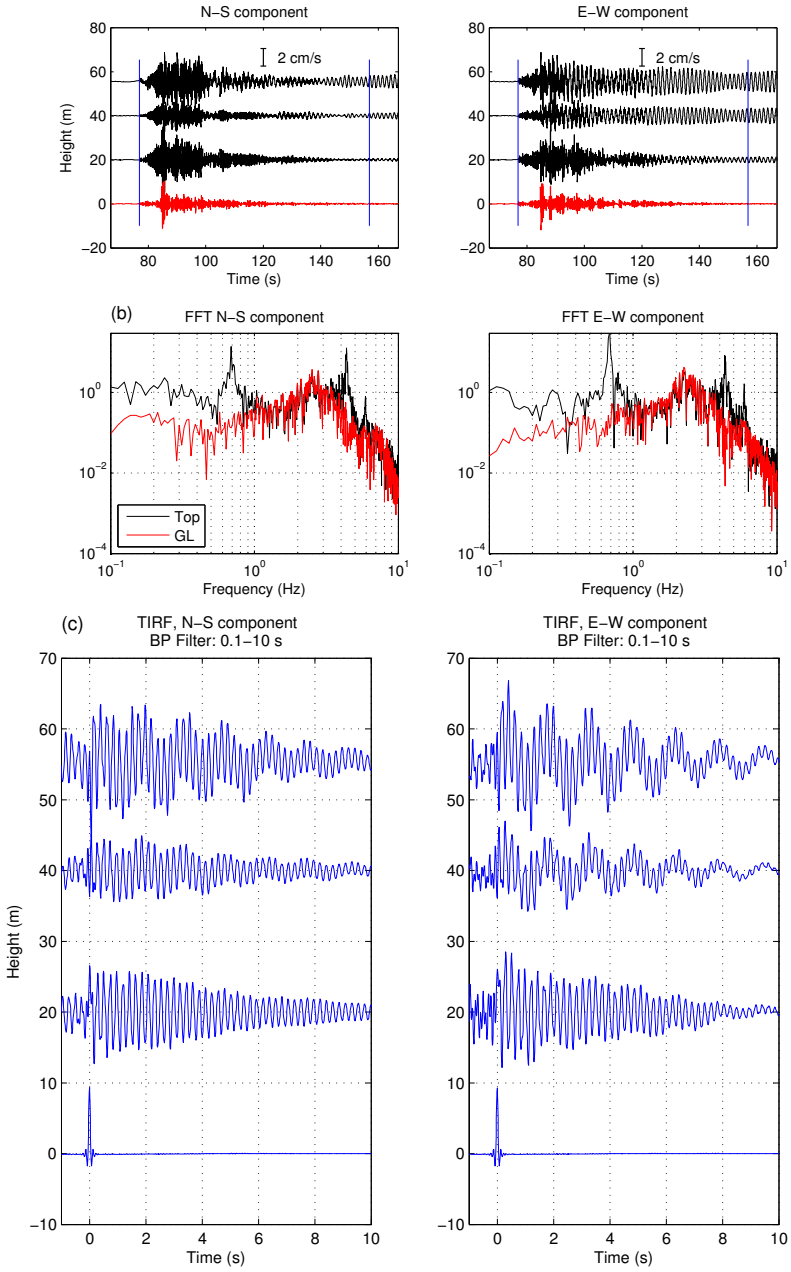

Figure 5.6: (a) Waveforms of the M_w 5.0 earthquake that occurred beneath the Tokyo Bay on September 12, 2015 recorded at different heights of the Hazawa Tower for (left) the *N-S* component and (right) the *E-W* component. The waveforms are bandpass filtered between 0.1 and 10 s. (b) Fourier spectra of the records at the ground level (red trace) and the top floor (black trace). The Fourier spectra are computed between the two vertical blue lines in (a). (c) TIRFs extracted from the records in (a) by regarding the station located on the ground level as the virtual source for the two horizontal components.

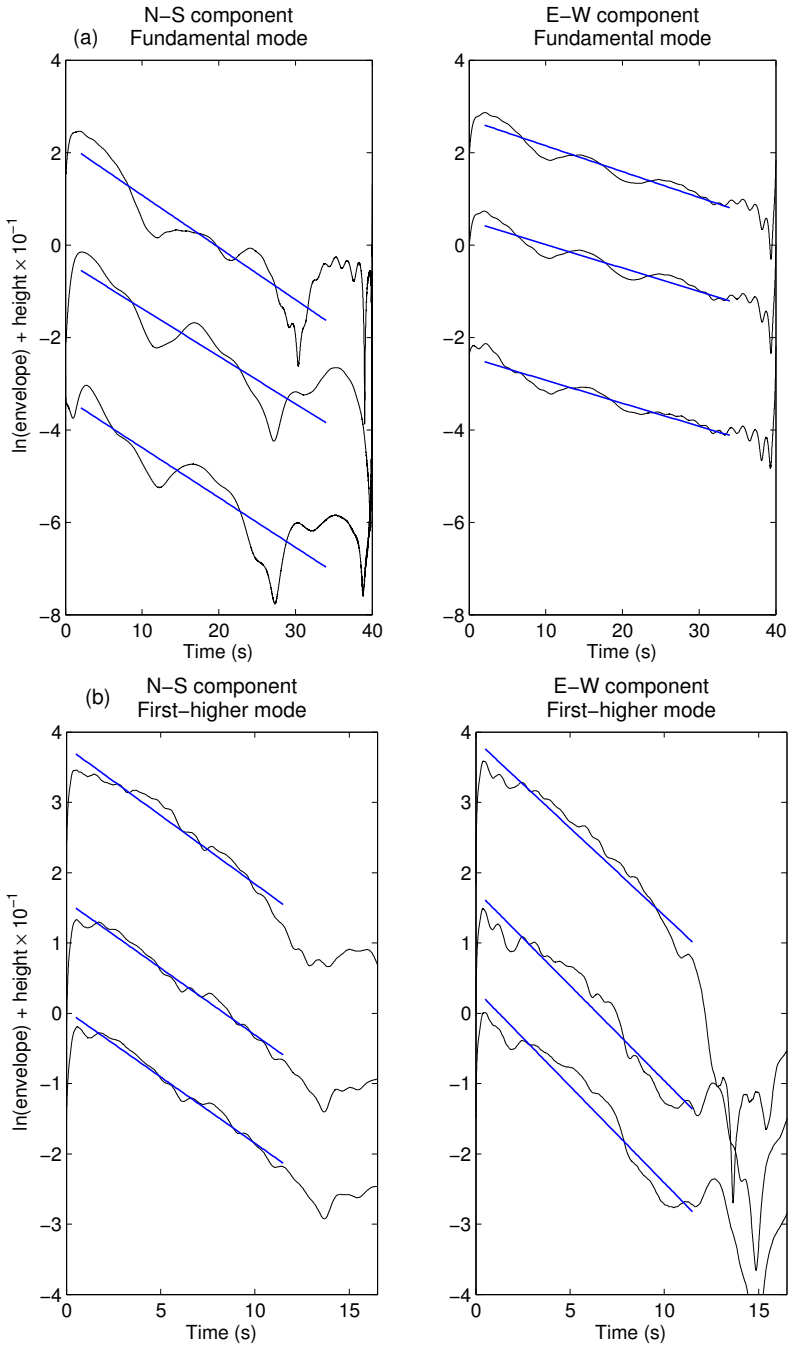

Figure 5.7: Neperian logarithm of the envelopes of the TIRFs shown in Figure 5.6c after filtering with a narrow bandpass filter around the (a) fundamental and (b) first-higher mode frequencies. To separate the waveforms, we added a factor that is a function of the height of the sensor to each curve. Note that this factor do not modify the decrease with time of the waveforms. For each curve, the best-fitting straight line is shown by a blue line.

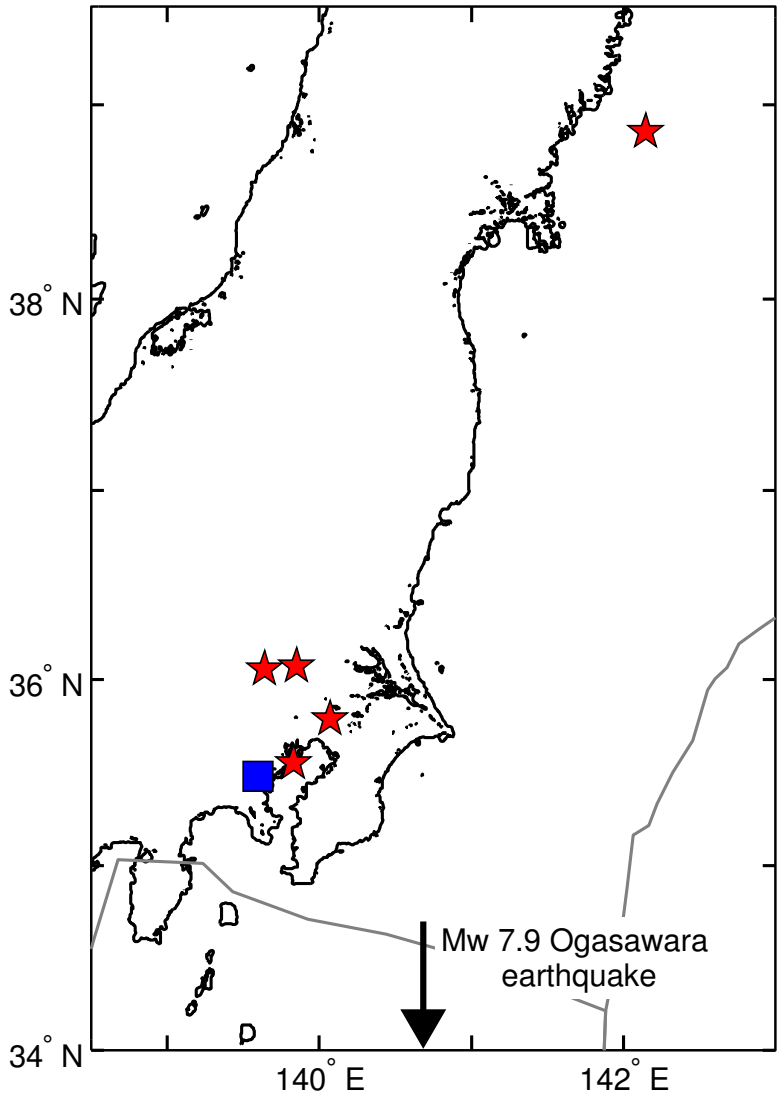

Figure 5.8: Map of the earthquakes listed in Table 5.2 which are used for the computation of the stacked TIRFs. The location of the tower is shown by the blue square.

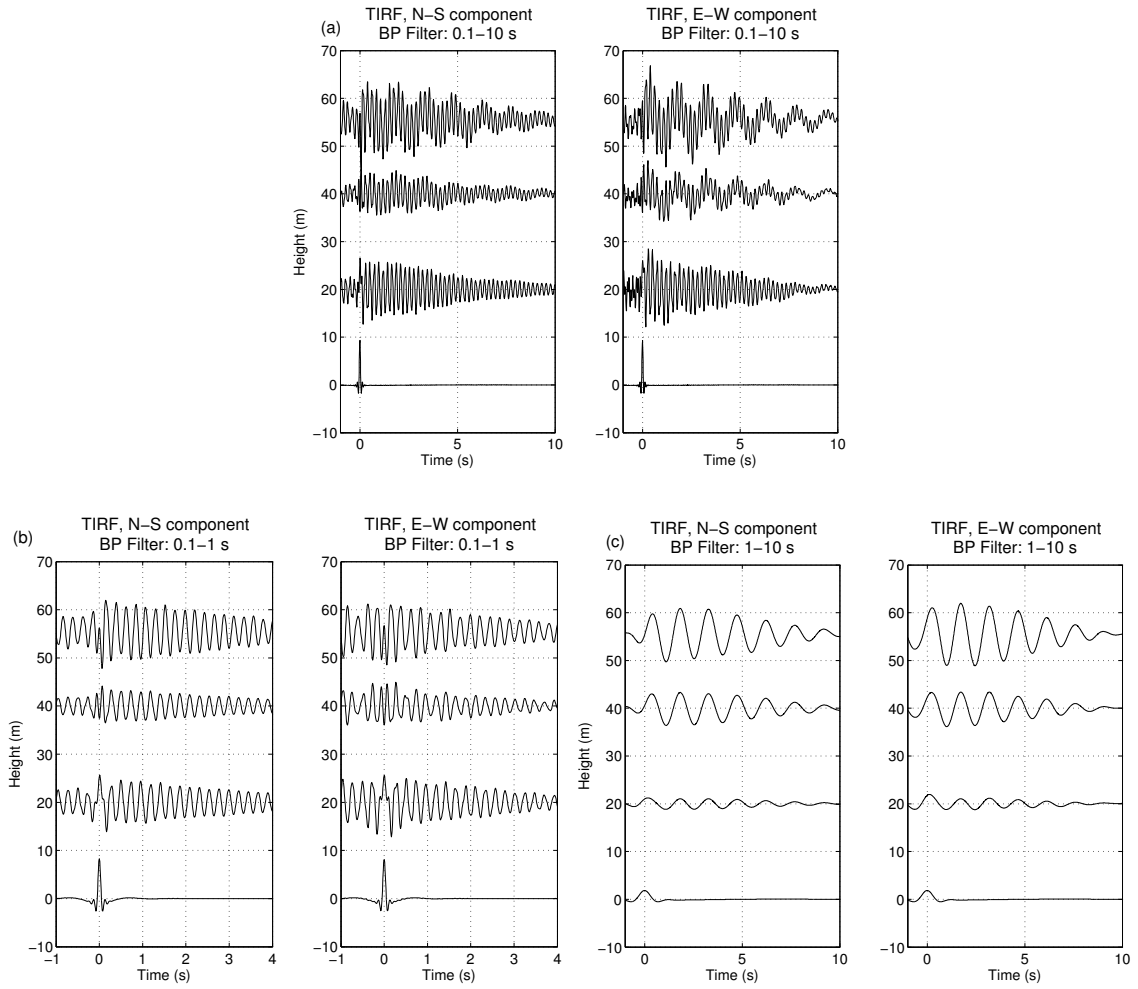

Figure 5.9: TIRFs computed after the stack of the earthquakes listed in Table 5.3 and shown in Figure 5.8. The station located on the ground level is used as virtual source and waveforms are bandpass filtered between (a) 0.1 and 10 s, (b) 0.1 and 1 s, and (c) 1 and 10 s. Note that the amplitude of the waveforms in (c) is twice the one of (a) and (b).

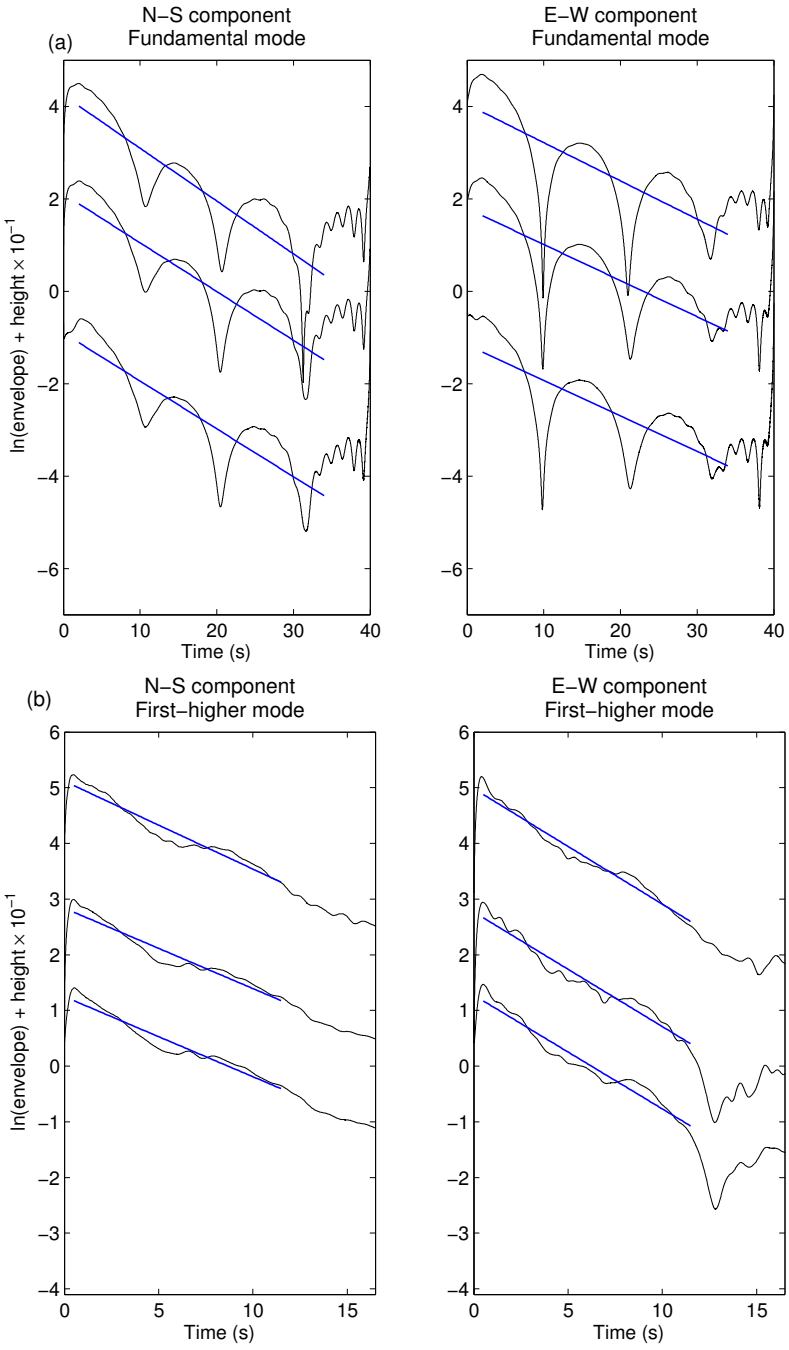

Figure 5.10: Neperian logarithm of the envelope of the TIRFs shown in Figure 5.9a after filtering with narrow bandpass filters around the (a) fundamental and (b) first-higher mode frequencies.

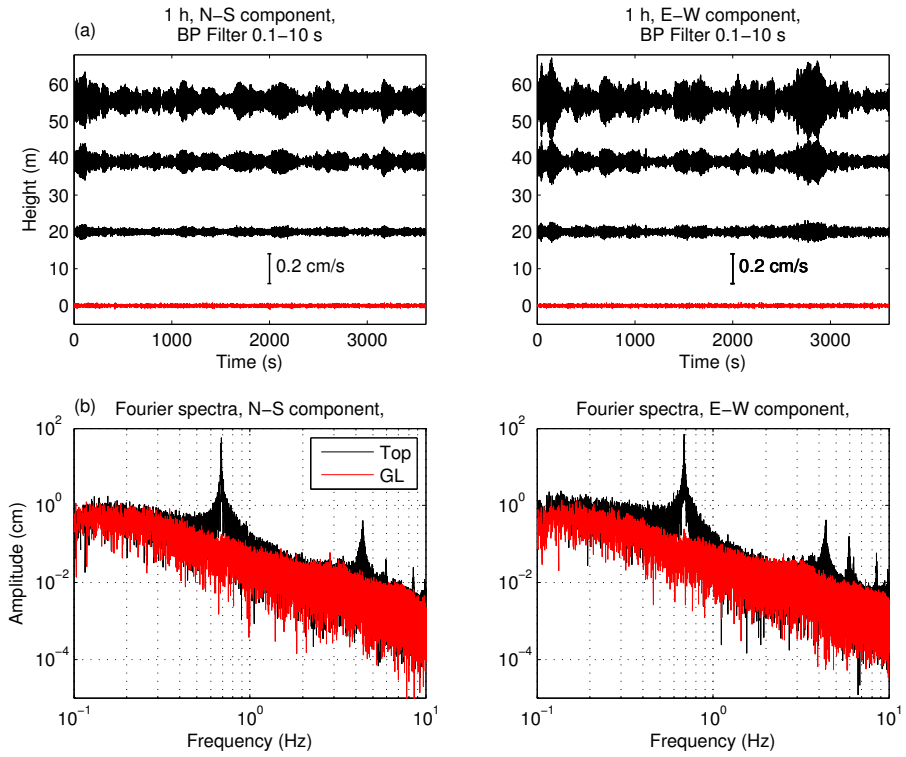

Figure 5.11: (a) One hour of ambient vibration recorded by (left) the *N-S* component and (right) the *E-W* component of the seismometers in velocity. Waveforms are bandpass filtered between 0.1 and 10 s. (b) Fourier transform of the record on the ground level (red) and the one of the top floor (black) for (left) the *N-S* and (right) *E-W* components.

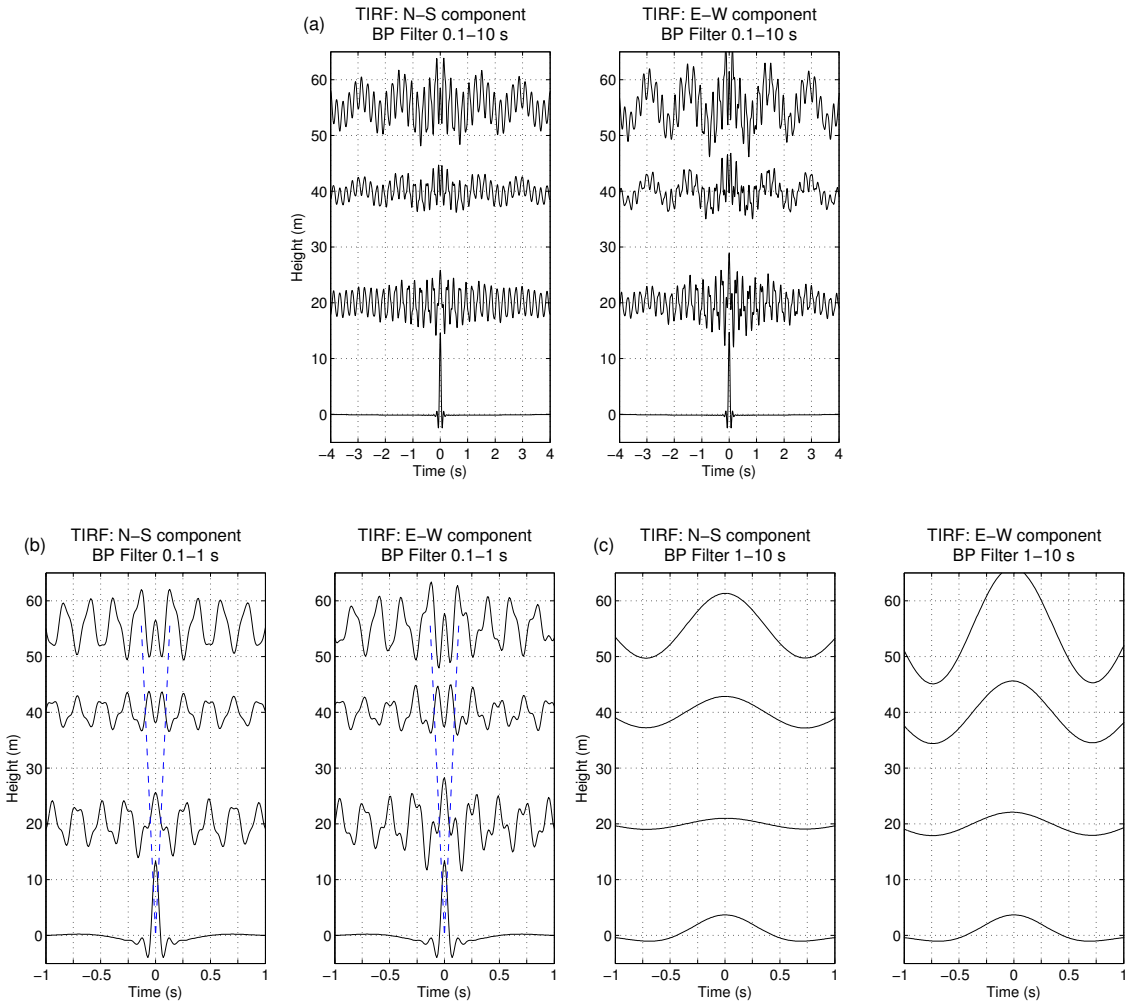

Figure 5.12: (a) TIRFs extracted from the 14 h of ambient vibration recorded by the (left) *N-S* and (right) *E-W* components, bandpass filtered between 0.1 and 10 s. (b) Same waveforms as in (a) but bandpass filtered between 0.1 and 1 s. The dashed blue lines represent a wave velocity of 400 m/s. (c) Waveforms bandpass filtered between 1 and 10 s. The amplitude of the waveforms in (c) is twice larger than the one in (a) and (b). The waveforms are only shown between -1 and 1 s in (b) and (c).

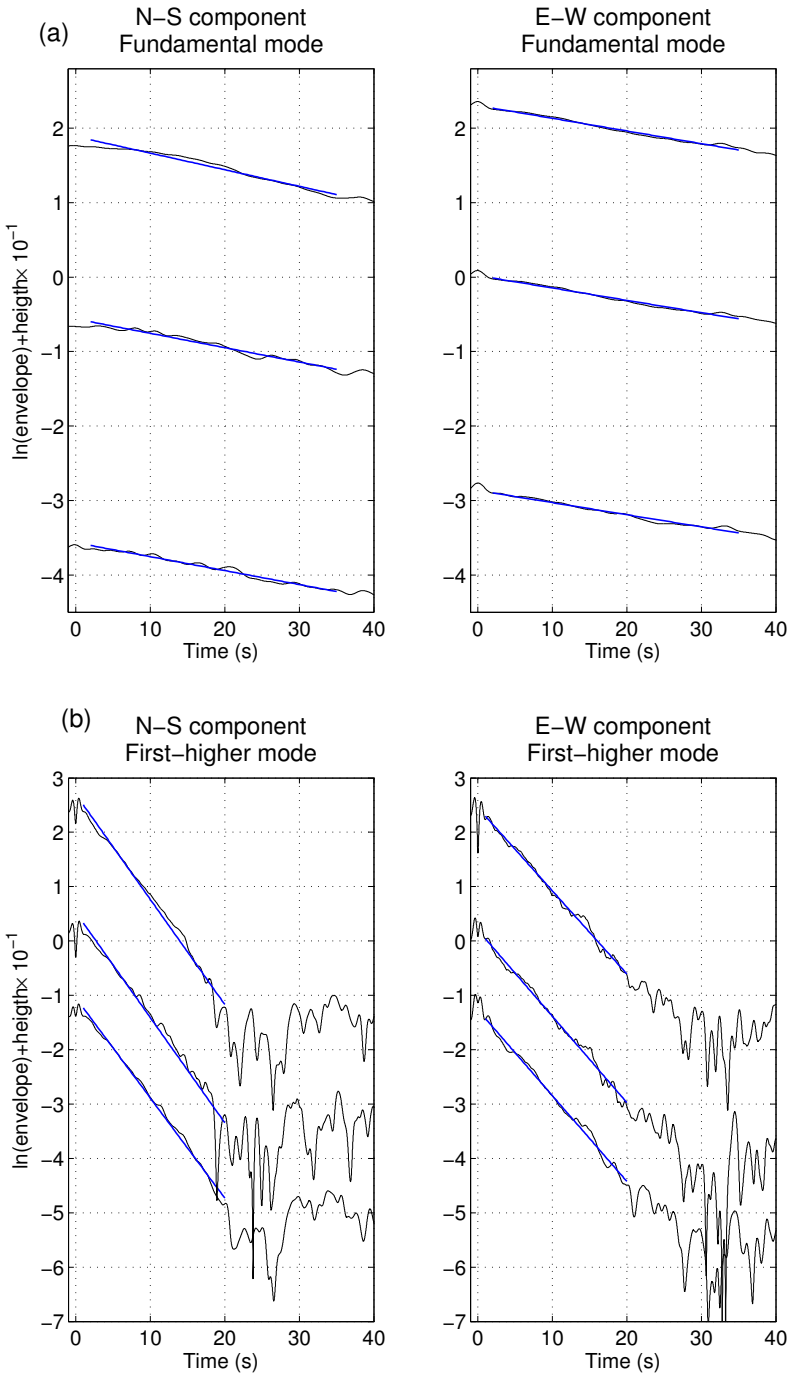

Figure 5.13: The natural logarithm of the envelope of the deconvolved waves in Figure 5.12a after applying a bandpass filter between (a) 1 and 2 s (fundamental mode) and (b) 0.1 and 0.3 s (First-higher mode). To separate the waveforms, we added a factor that is a function of the height of the sensor to each curve. For each curve, the best-fitting straight lines is shown by blue lines.

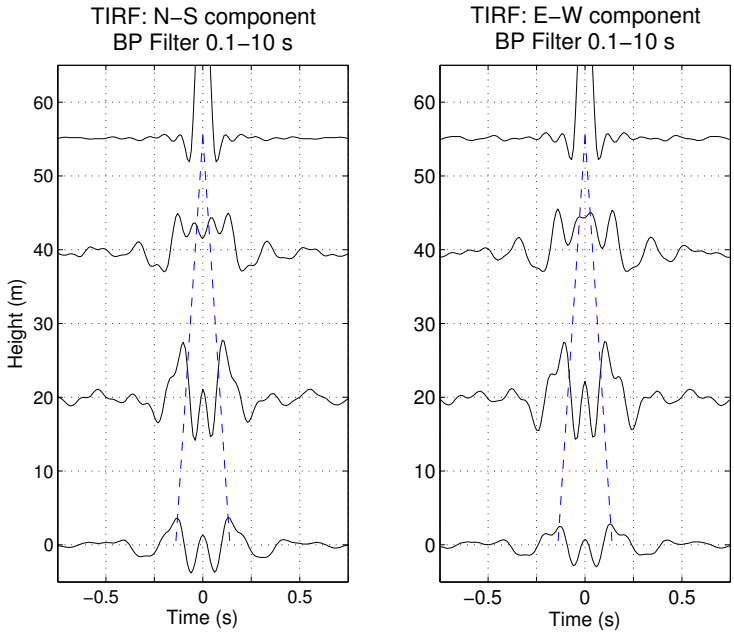

Figure 5.14: Deconvolved waves from the 14 h of ambient vibrations using the sensor located on the top floor as virtual source. The waveforms are bandpass filtered between 0.1 and 10 s. The dashed blue lines represent a wave velocity of 400 m/s.

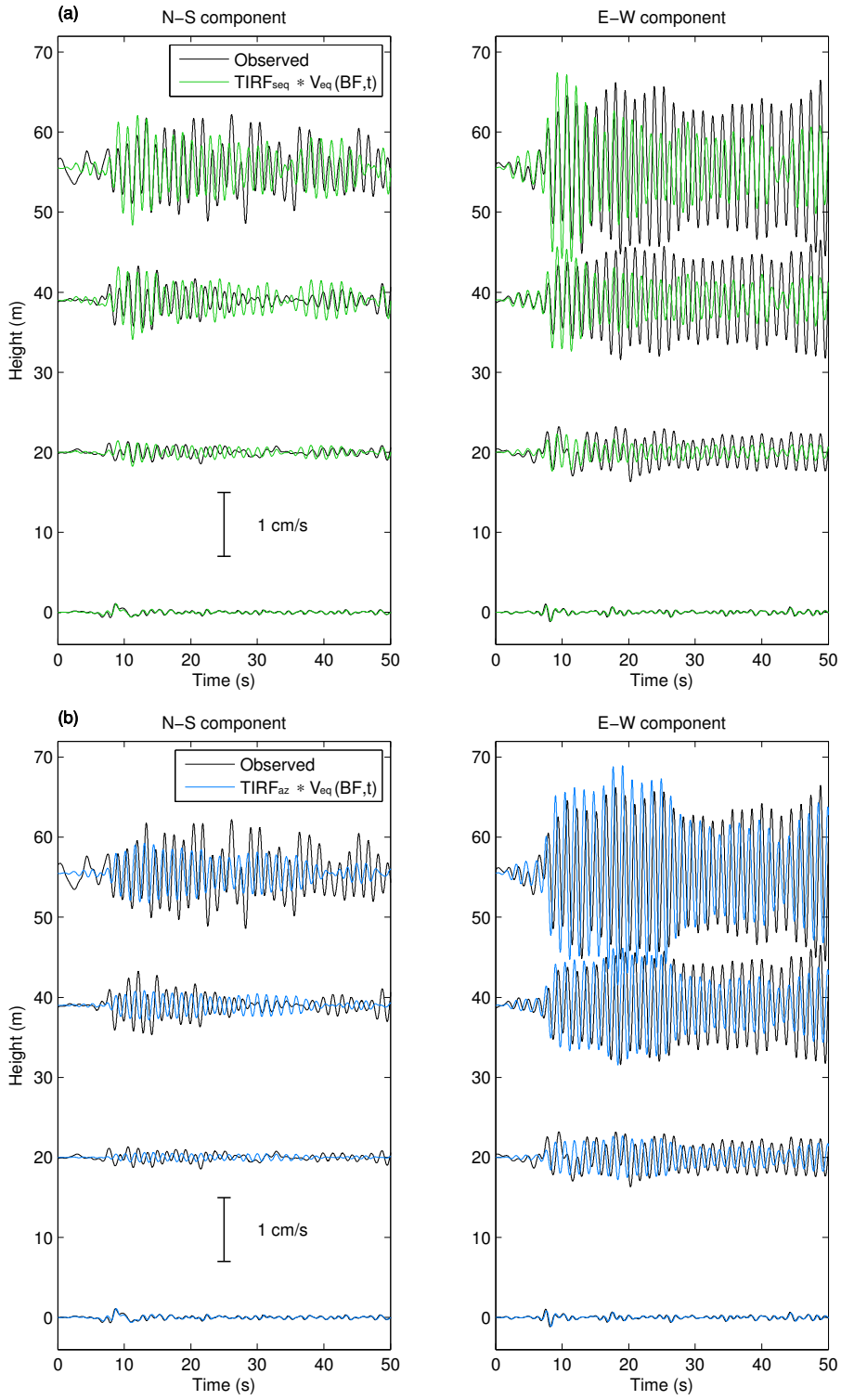

Figure 5.15: Simulated waveforms obtained from the convolution of the records at the ground level of the M_w 5.0 earthquake, which occurred beneath the Tokyo Bay, with the tower response computed from (a) the stack of earthquakes (green) and (b) ambient vibrations (blue). Recorded waveforms at each height are shown in black. All the waveforms are bandpass filtered between 1 and 10 s.

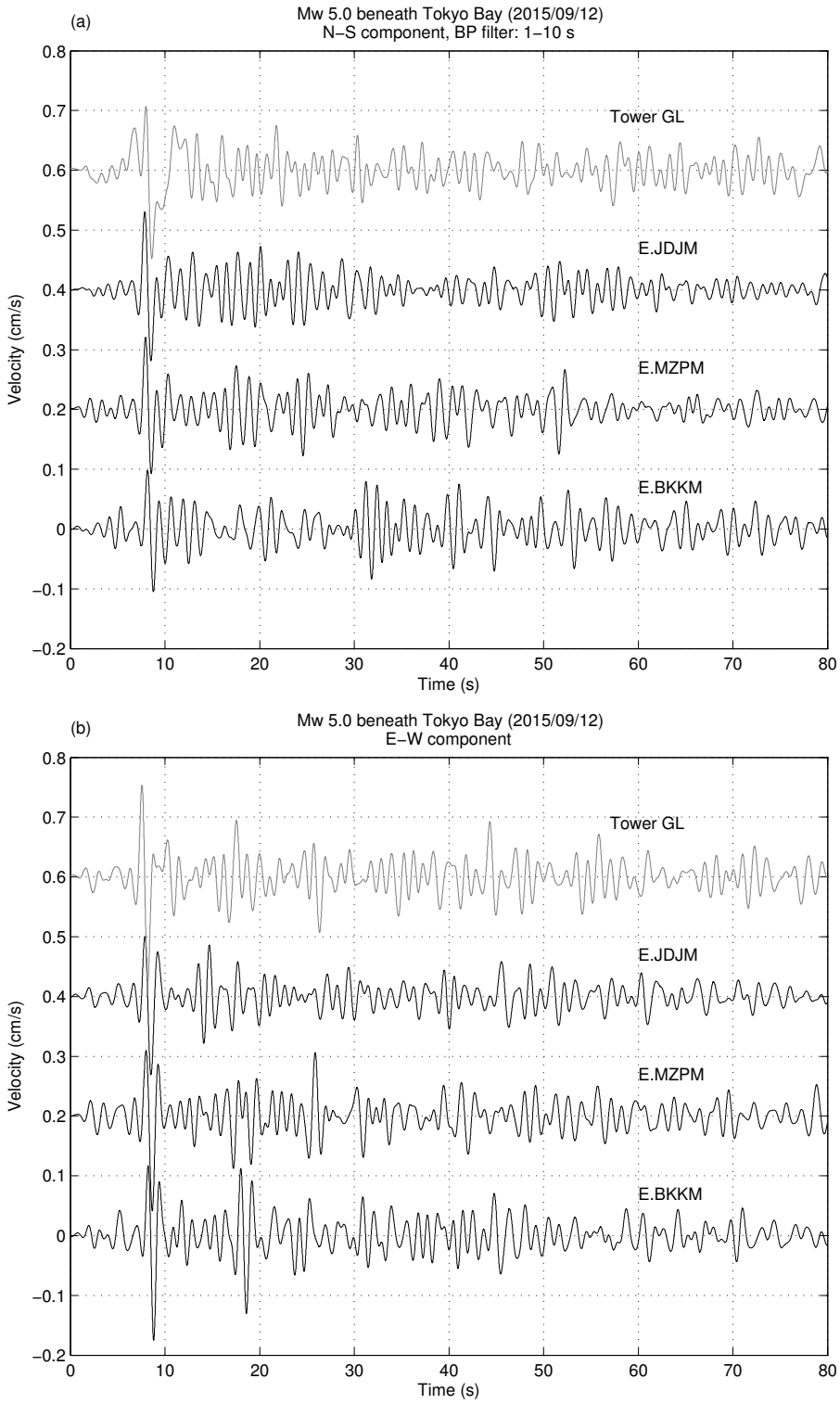

Figure 5.16: Comparison between the records of the M_w 5.0 earthquake at the tower ground level (gray) and at the E.BKKM, E.MZPM, and E.JDJM stations (black) for (a) the *N-S* and (b) *E-W* components. Waveforms are bandpass filtered between 1 and 10 s.

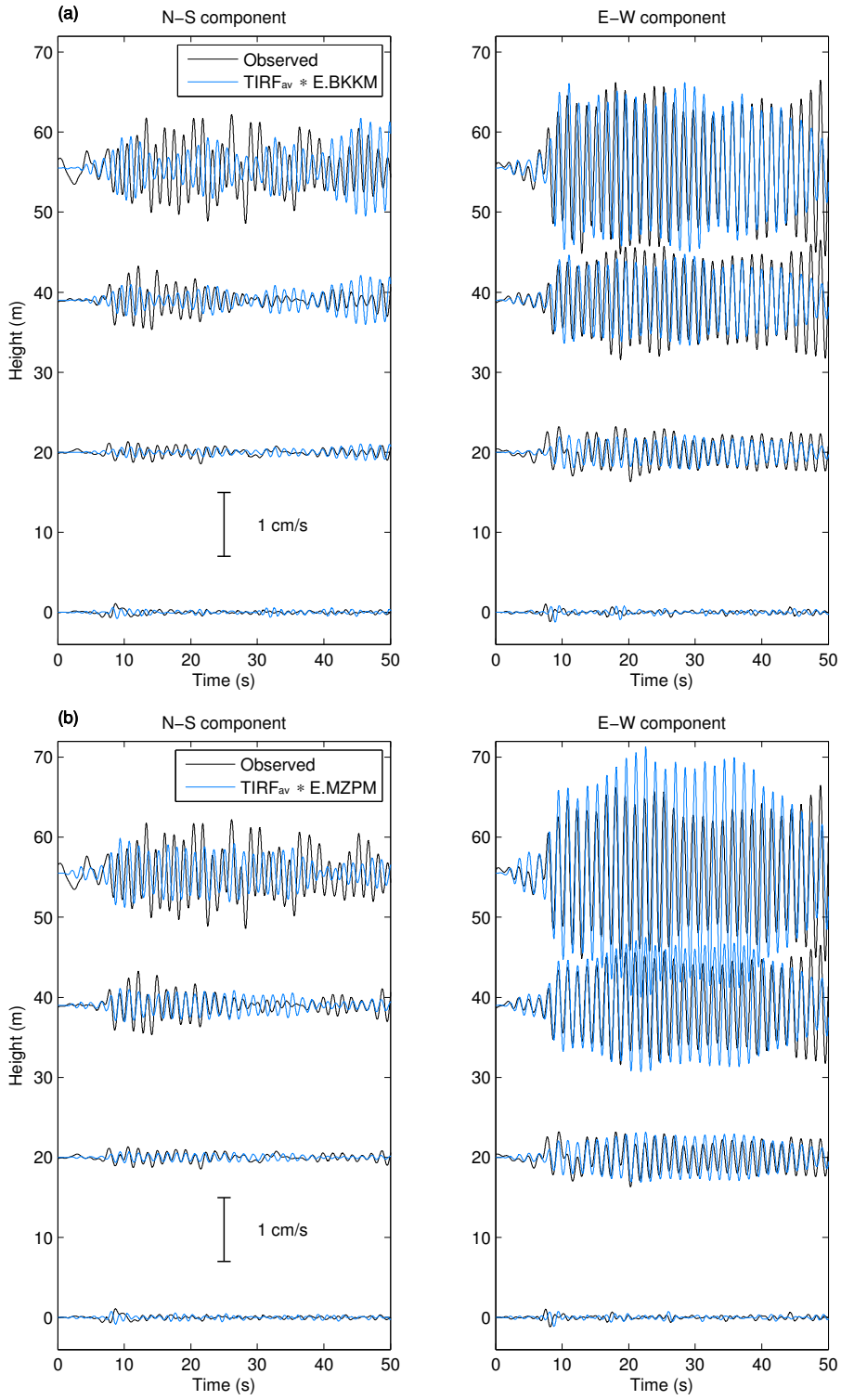

Figure 5.17: Comparison between the records of the M_w 5.0 earthquake at each height of the tower (black) and the simulated building motions computed from the convolution of the TIRF_{av} with the recorded earthquake (blue) at the (a) E.BKKM, (b) E.MZPM, and (c), E.JDJM stations. Waveforms are bandpass filtered between 1 and 10 s to only focus on the fundamental mode.

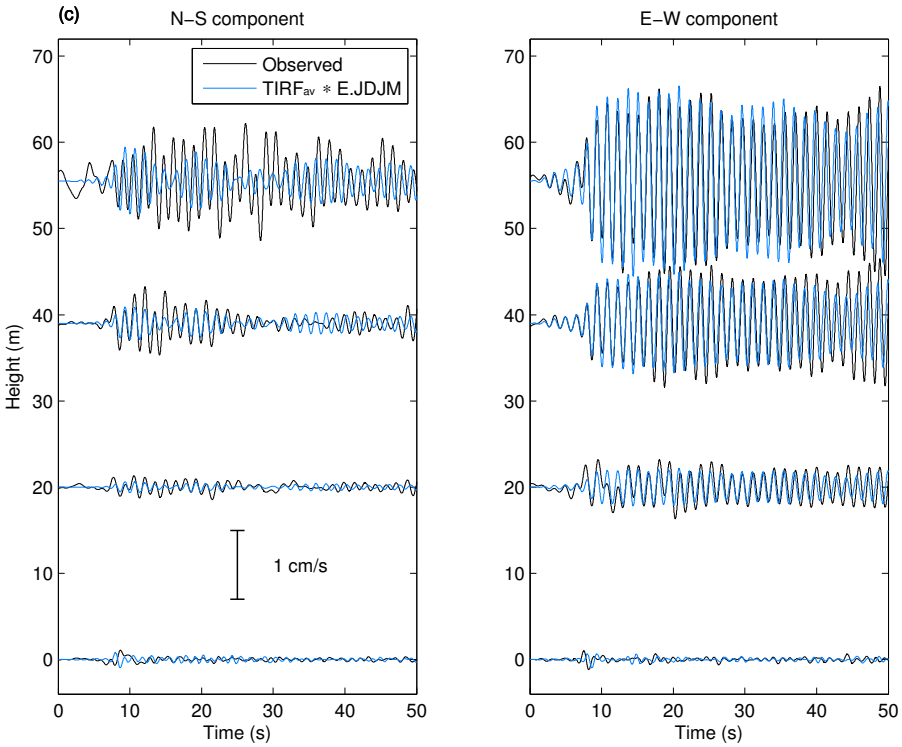

Figure 5.17: (Continued)

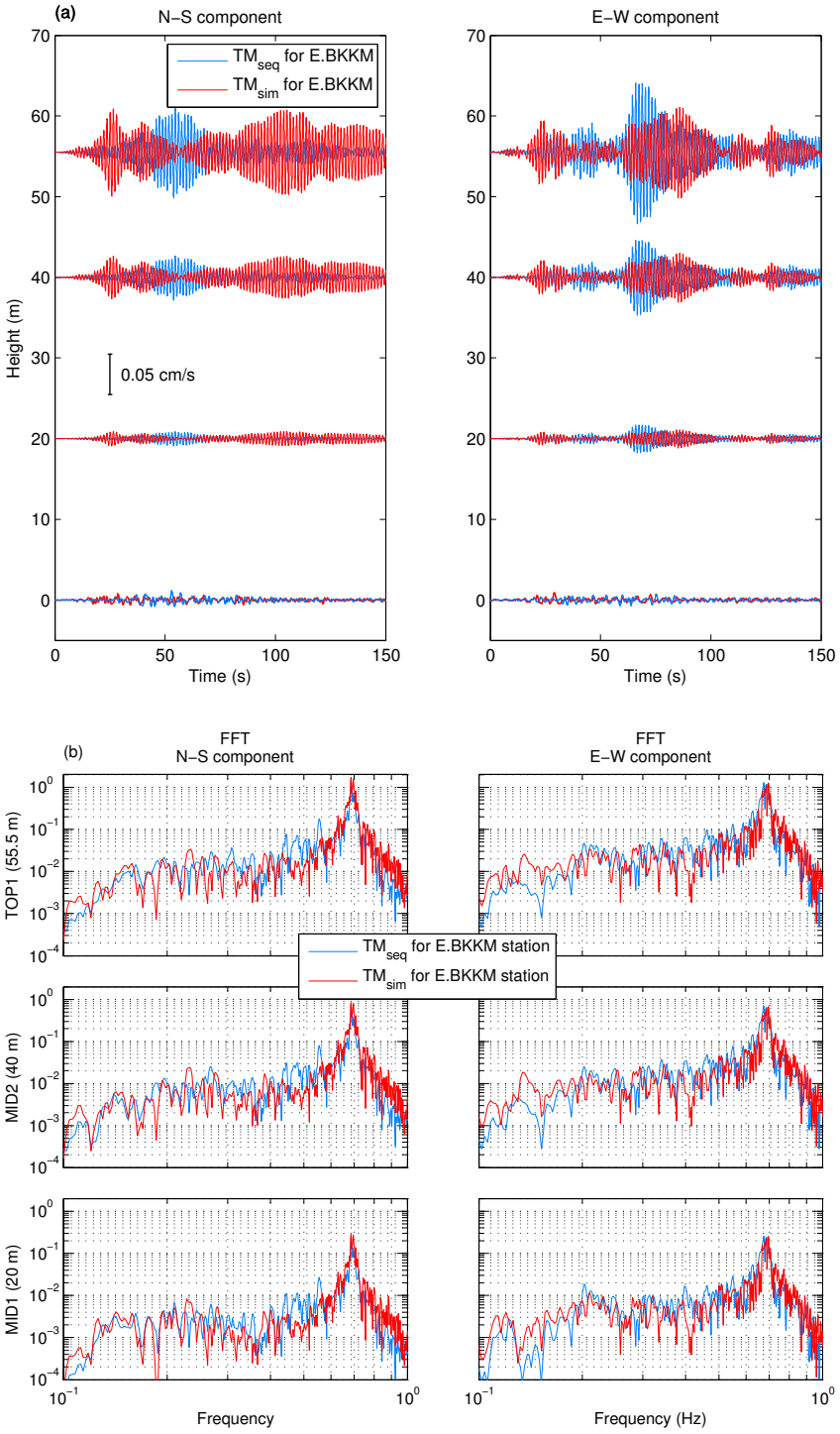

Figure 5.18: (a) Prediction of the tower motion from the convolution of the $\mathrm{TIRF_{av}}$ with the calibrated Green's functions ($\mathrm{TM_{sim}}$) (red) and with the records of the 2011 M_w 4.1 Hakone earthquake ($\mathrm{TM_{av}}$) (blue) at the E.BKKM station. Waveforms are bandpass filtered between 1 and 10 s to only focus on the fundamental mode. (b) Fourier spectra of the waveforms shown in (a).

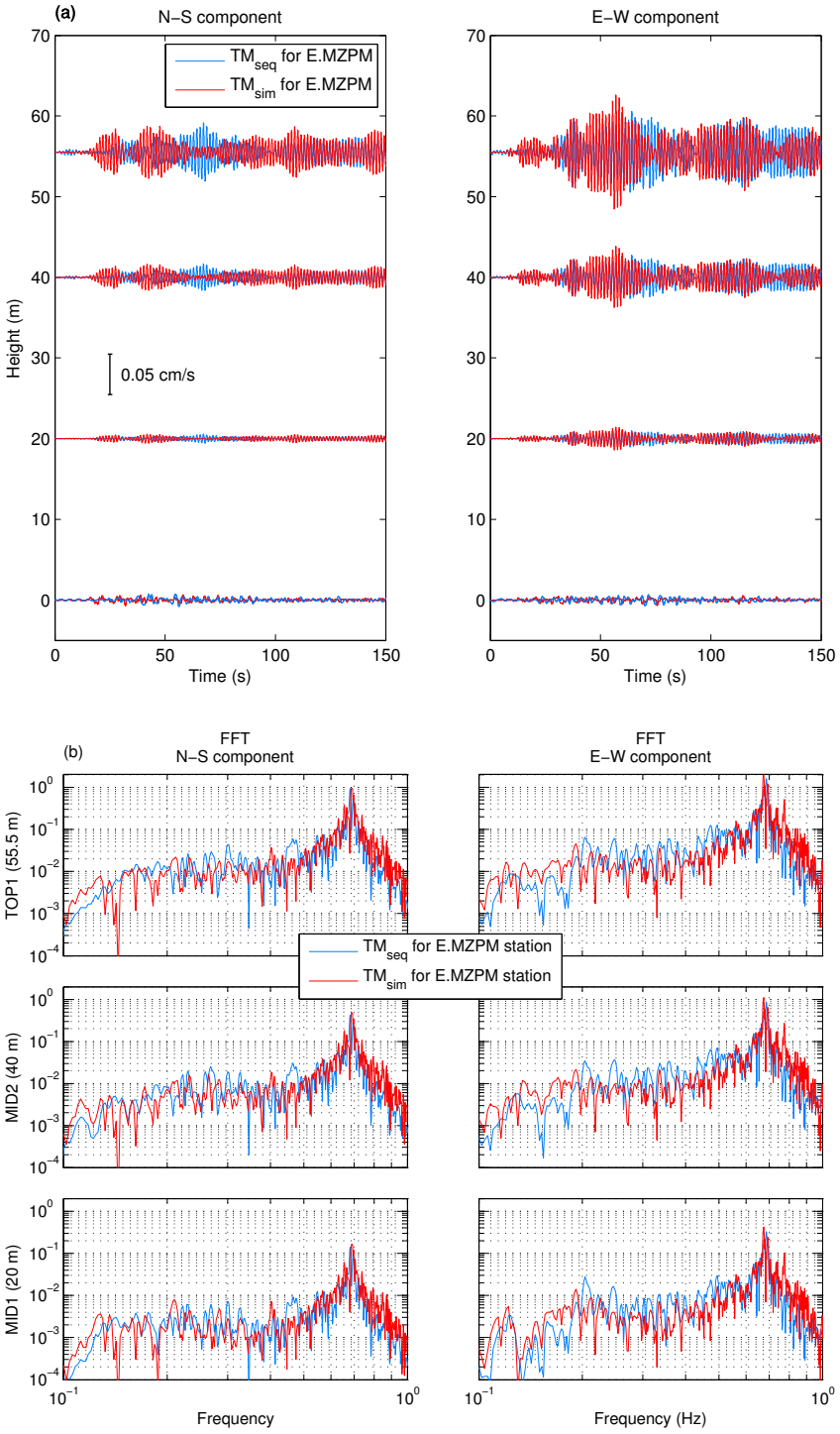

Figure 5.19: Same as Figure 5.18 for the waveforms at the E.MZPM station.

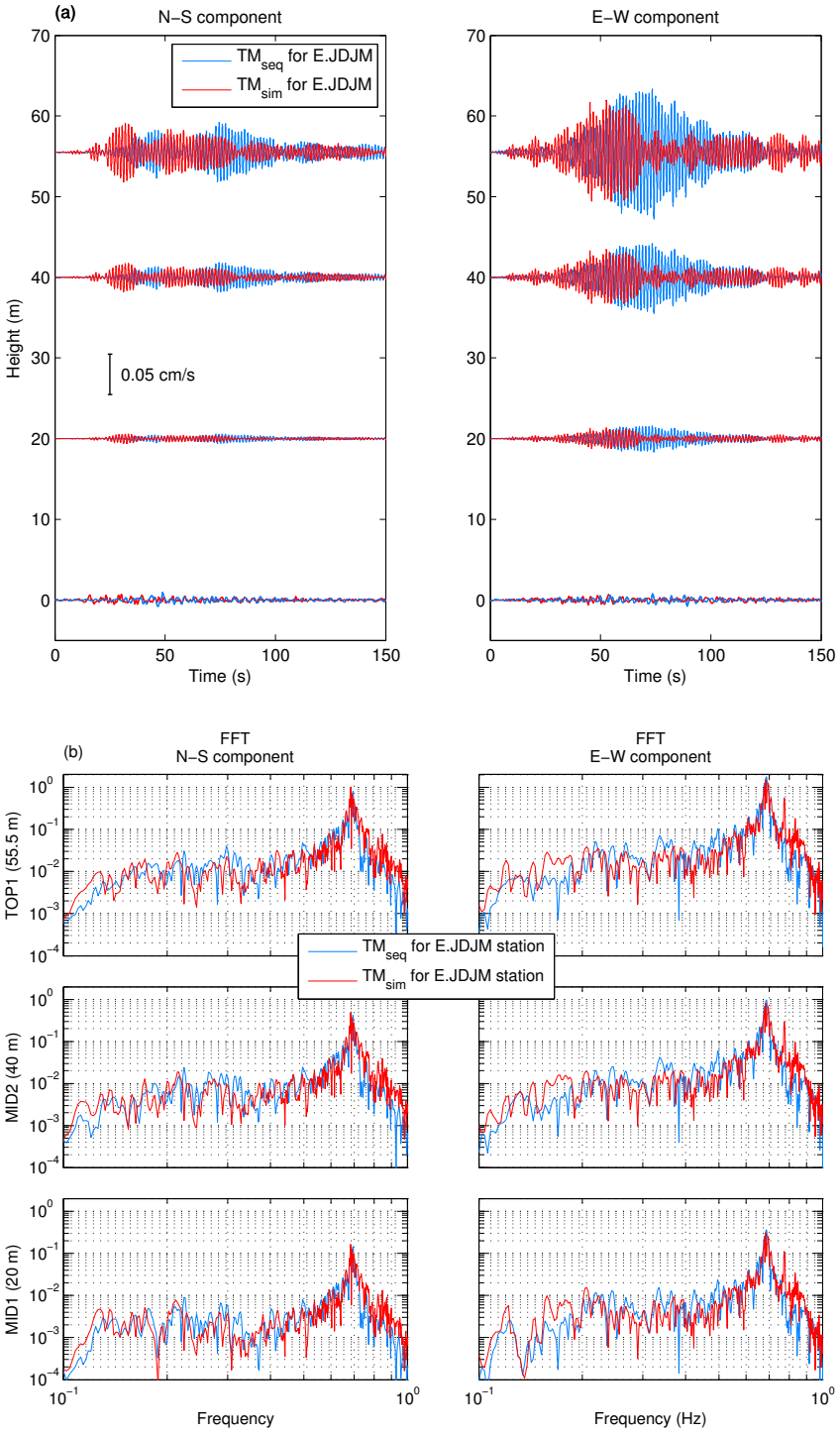

Figure 5.20: Same as Figure 5.18 for the waveforms at the E.JDJM station.

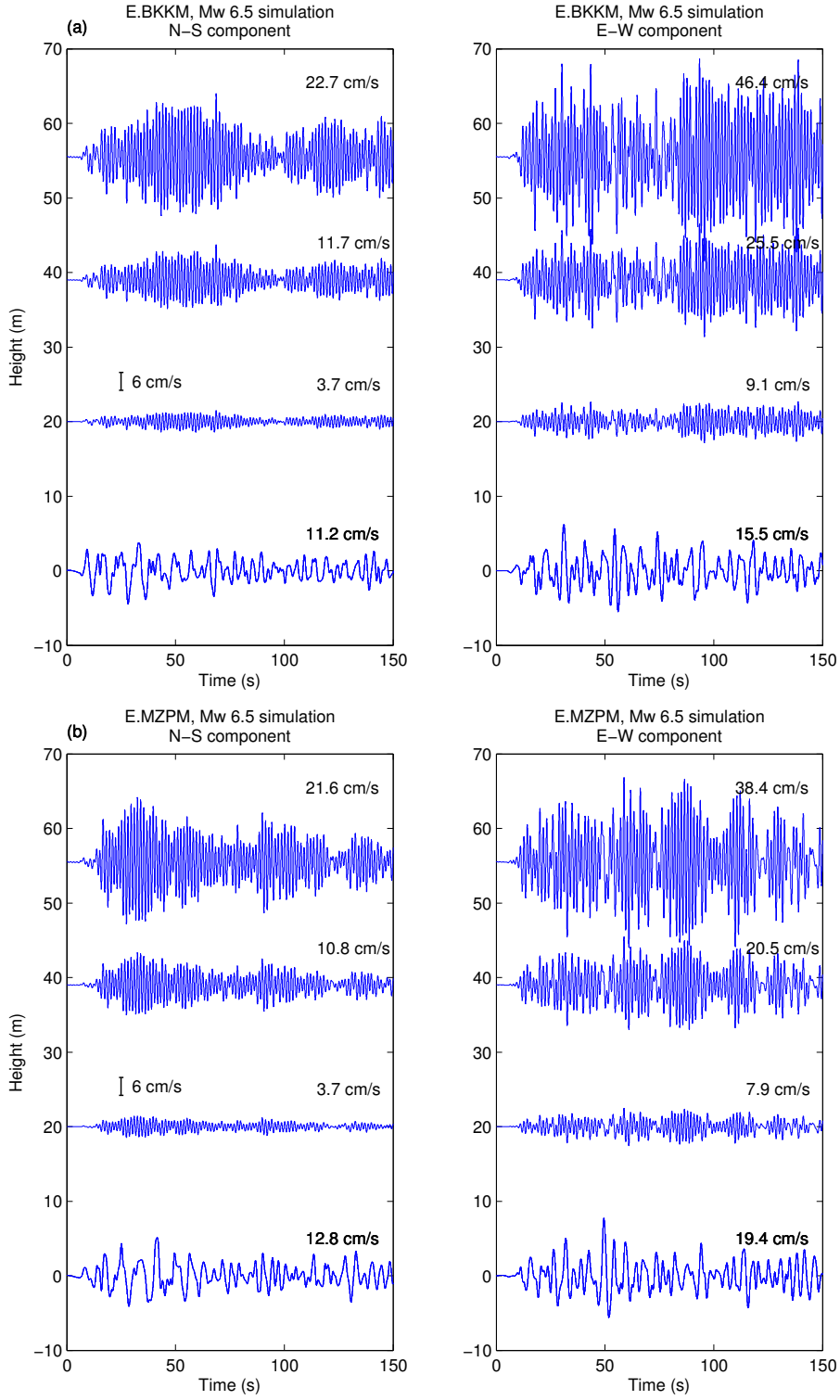

Figure 5.21: Prediction of the building motion during the M_w 6.5 earthquake scenario using the simulated waveforms at the (a) E.BKKM, (b) E.MZPM, and (c) E.JDJM stations. The waveforms are bandpass filtered between 1 and 10 s and the long-period PGVs are indicated for each waveform.

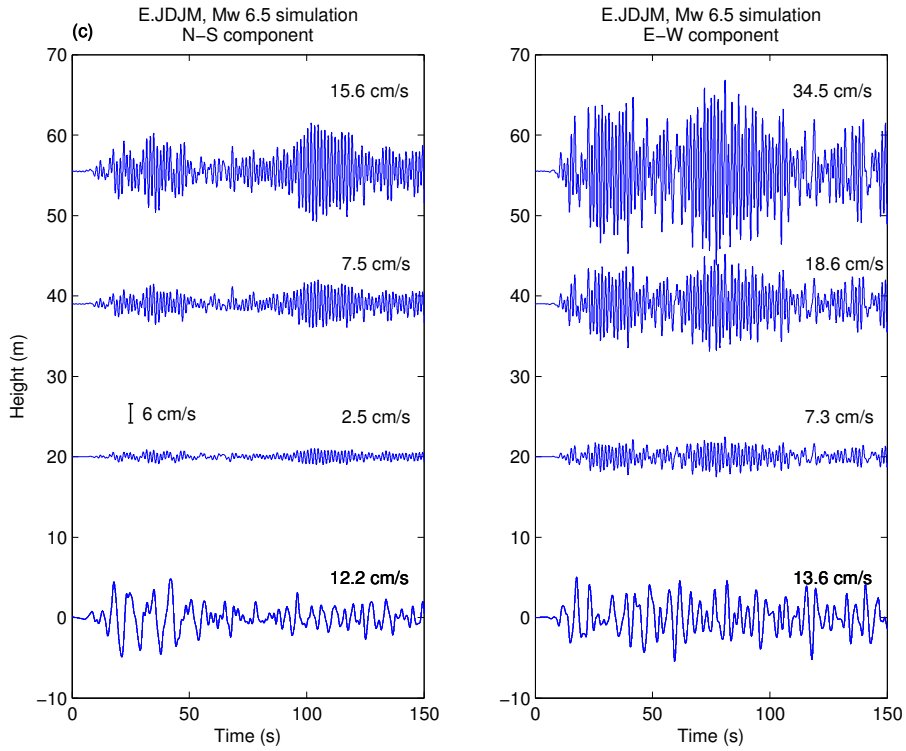

Figure 5.21: (Continued)

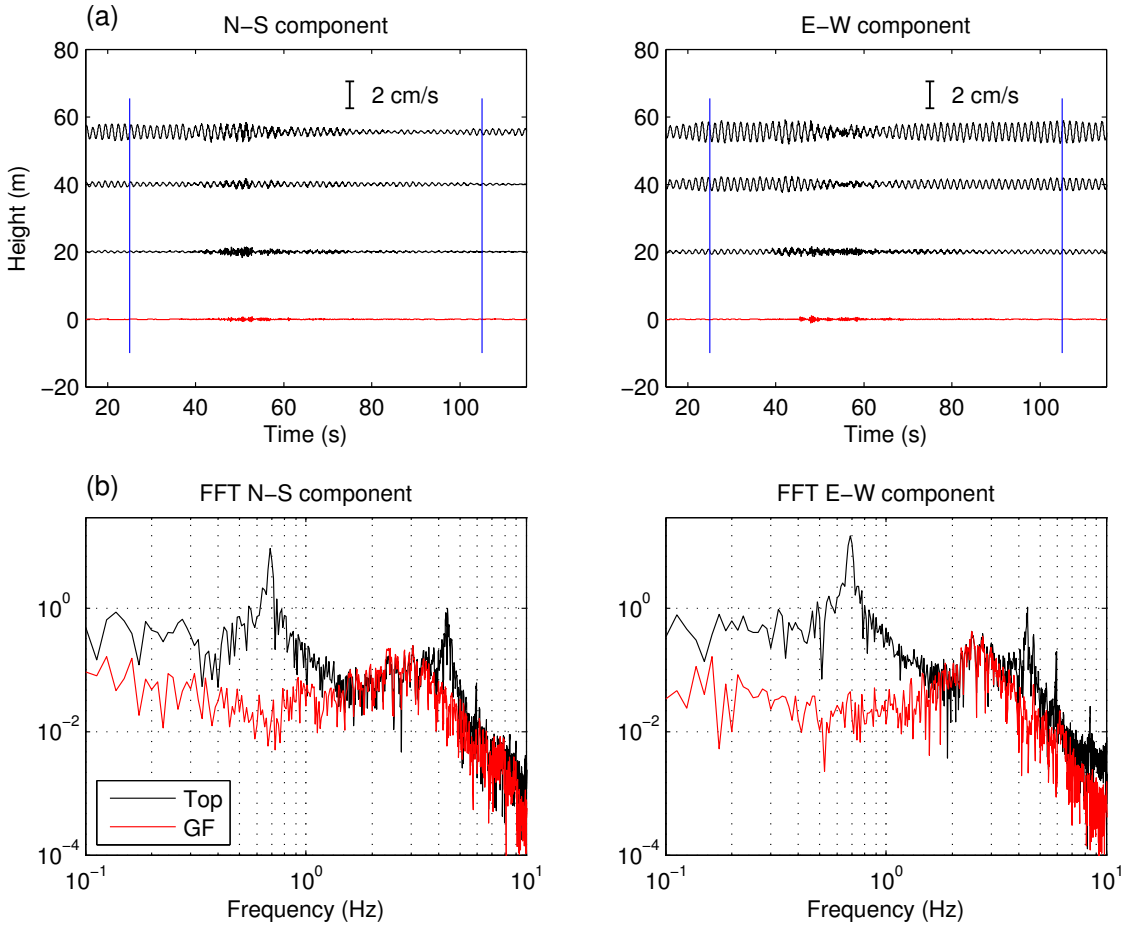

Figure 5.22: (a) Records at different heights of the Hazawa Tower of the M_w 4.1 earthquake that occurred on October 25, 2015 in the Yamanashi prefecture. The earthquake waveforms arrive at approximately 40 s (b) Fourier spectra of the waveforms at the ground level (red) and the top floor (black) of the tower for the (left) *N-S* and (right) *E-W* component. The Fourier spectra are computed between the two vertical blue lines in (a).

Chapter 6

Conclusions

6.1 General Conclusions

We explored the potential of seismic interferometry for predicting long-period ground motions of earthquakes. The deconvolution method allows to retrieve Green's functions between station pairs that have reliable phases and amplitudes. To validate the use of this method as an alternative to GMPEs and physics-based simulations for seismic hazard assessment purposes, we applied this technique to different kinds of earthquakes using thousands of seismometers which have been deployed in Japan.

In Chapter 2, we used the ambient seismic field recorded by offshore ocean bottom seismometers (OBSs) located atop the Nankai subduction zone and onshore stations. We extracted offshore-onshore Green's functions and showed that they can be used to predict the long-period ground motions generated by a moderate M_w 5.0 subduction earthquake that occurred in the vicinity of an OBS station (virtual source). After calibration of the Green's function amplitudes and taking into account that the sources of the ambient seismic field are not uniformly distributed with respect to the azimuth, we demonstrated that the distribution of the pseudovelocity response at different periods computed from earthquake and calibrated Green's function waveforms are highly similar. Such result validates

the use of the ambient seismic field recorded by the increasing number of offshore seismometers to predict the long-period ground motions of subduction events.

Sedimentary basins can significantly amplify seismic waves and their effect needs to be studied to accurately assess seismic hazard. In Chapter 3, we applied the deconvolution method to approximately 420 stations, which are mainly a part of the dense Metropolitan Seismic Observation network (MeSO-net), that have been deployed in the Kanto basin, Japan. We showed that the recovered Green's functions contain both body and surface waves that are sensitive to the different layers that compose the basin. We also used the Green's functions to simulate the ground motions of two moderate earthquakes that occurred on the eastern and southern edges of the basin. The density of the MeSO-net stations allows to simulate earthquake ground motions with a high spatial resolution. Such results demonstrate the potential of dense networks recording continuously the ambient seismic field for assessing seismic hazard in highly populated metropolitan areas.

As moderate events generally do not generate damaging long-period seismic waves, we also focused on the simulation of a large earthquake, for which the point source hypothesis that is made for moderate events is no longer valid. In Chapter 4, we combined finite rupture modeling and extracted Green's functions, which have their amplitudes calibrated with a M_w 5.0 aftershock, to simulate the long-period ground motions of the 2008 M_w 6.9 Iwate-Miyagi Nairiku earthquake. We constructed several finite source model having similar characteristics to the ones found by inversion studies using scaling relations between small and large earthquakes. We combined the finite source models with the extracted Green's functions and simulated the long-period ground motions of the mainshock. We found that simulated and observed waveforms agree well for the different source models that we constructed. Such result validates the combined use of the ambient seismic field and finite rupture modeling to simulate the long-period ground motions of large earthquakes.

In Chapter 5, we showed that seismic interferometry by deconvolution can be used to simulate the whole earthquake process from the source to building motions. We used point force Green's functions to simulate the long-period ground motions at three MeSO-net stations generated by a M_w 4.1 earthquake that occurred in the Hakone region in 2011. We constructed a finite source model using the methodology presented in Chapter 4 to predict the long-period ground motions of a M_w 6.5 earthquake scenario that could occur along the Sagami Trough. Using ambient vibrations recorded at different heights of a telecommunication tower located in the Tokyo metropolitan area, we extracted the response of the structure and studied its characteristics. We showed that the tower impulse response functions can be convolved with the Green's functions calibrated with the M_w 4.1 earthquake to simulate the motion of the fundamental mode of the tower. We also used the predicted ground motions of the M_w 6.5 earthquake scenario to study the building motion that could be generated by such event. The integrated simulation from earthquake source to building motion shows promising results that might help to mitigate seismic risk.

Despite the good fit between most of the Green's functions and earthquake waveforms presented in the four chapters of this thesis, the interferometry by deconvolution method also has some weaknesses that need to be discuss. First, the recovery of clear and realistic Green's functions between two seismic stations depends on several factors. Indeed, the distribution of the ambient seismic field sources, the location of stations, the quality of the records, or the preprocessing can affect the quality of the extracted Green's functions. This multitude of factors makes difficult to define general laws that ensure the best quality of the extracted Green's functions. Therefore, a special care needs to be taken when extracting Green's functions and a close examination of all the parameters mentioned above should be perform to evaluate the quality of the extracted waveforms. Second, only the relative, rather than the absolute amplitude of the Green's functions can be retrieved.

Therefore, the amplitude of the Green's functions always needs to be calibrated with earthquake records to simulate/predict ground motions. This calibration factor depends on the quality of the Green's functions, the component, and the period range of interest and needs to be calculated for each case.

6.2 Future Directions

We demonstrated that the ambient seismic field is a powerful tool to predict long-period ground motions of earthquakes. In Chapter 2, we showed that the long-period ground motions of a moderate offshore event can be accurately simulated using ocean bottom seismometers (OBSs) as virtual source stations. Despite the fact that the deployment of permanent OBSs remains costly, the increasing number of offshore networks recording continuously the ambient seismic field could be used to simulate large offshore earthquakes using the methodology presented in Chapter 4. For example, the DONET network, which is composed of 20 offshore stations, can be used to simulate earthquake scenarios that could occur along the Nankai Trough. Such simulations could also be performed with the data recorded by the OBSs that have been deployed along the Cascadia subduction zone in the United States. Finally, the S-net network, which is currently under deployed from the Kanto to Hokkaido regions, will be a good opportunity to validate the technique with megathrust earthquakes.

We demonstrated in Chapter 5 that simulations of the whole earthquake process from the source to the building motions can be performed. We analyzed the building motions of a telecommunication tower that has a fundamental resonance period of approximately 1.5 s. Such resonance period is shorter than the period range for which the potential of the ambient seismic field Green's functions has been demonstrated (e.g., periods longer than 4 s). Very large and tall structures, such as the Sakishima Office building shown in

Figure 1.1, have a resonance period that is longer than 4 s. Therefore, the combination of ambient seismic field Green's functions with the response of such structures should lead to a more accurate mitigation of seismic risk.

The great advantage of seismic interferometry to predict earthquake ground motions is that it does not require the large computational power that is needed for the physics-based simulations. Therefore, the waveforms of a large number of earthquake scenarios can be rapidly simulated. After identification of all the earthquake scenarios that are threatening a given site, waveforms of all the seismic events can be simulated and their ground motion parameters, such as PGV or PGD, quickly estimated. These parameters could be used in addition to the traditional values obtained from attenuation relations, and for a given exposure time and for a given level of ground motion, be combined into probabilistic seismic hazard assessment (PSHA).

References

Aki, K. (1957), Space and time spectra of stationary stochastic waves, with special reference to microtremors, *Bull. Earthq. Res. Inst., Univ. Tokyo*, *35*, 415–456.

Aki, K. (1965), A note on the use of microseisms in determining the shallow structure of the Earth's crust, *Geophysics*, *30*, 665–666, doi:10.1190/1.1439640.

Anderson, J. G., P. Bodin, J. N. Brune, J. Prince, S. K. Singh, R. Quaas, and M. Onate (1986), Strong ground motion from the Michoacan, Mexico, earthquake, *Science*, *233*, 1043–1049, doi:10.1126/science.233.4768.1043.

Ando, M. (1975), Source mechanisms and tectonic significance of historical earthquakes along the Nankai trough, Japan, *Tectonophysics*, *27*, 119–140, doi:10.1016/0040-1951(75)90102-X.

Aoi, S., T. Kunugi, and H. Fujiwara (2008), Trampoline effect in extreme ground motion, *Science*, *322*, 727–730, doi:10.1126/science.1163113.

Beck, J. L., and J. F. Hall (1986), Factors contributing to the catastrophe in Mexico City during the earthquake of September 19, 1985, *Geophys. Res. Lett.*, *13*, 593–596, doi:10.1029/GL013i006p00593.

Bertelli, T. (1872), Osservazioni sui piccolo movimenti dei pendoli in relazione ad alcuni fenomeni meteorologiche, *Bullettino Meteorologico dell'Osservatorio dell Colle-*

gio Romano, Roma, Italy, *101*.

Biot, M. (1933), Theory of elastic systems vibrating under transient impulse with an application to earthquake-proof buildings , *Proc. Nat. Acad. Sci.*, *19*, 262–268.

Blaser, L., F. Krüger, M. Ohrnberger, and F. Scherbaum (2010), Scaling relations of earthquake source parameter estimates with special focus on subduction environment, *Bull. Seismol. Soc. Am.*, *100*, 2914–2926, doi:10.1785/0120100111.

Bommer, J. J. and Alarcón, J. E. (2006), The prediction and use of peak ground velocity, *Journal of Earthquake Engineering*, *10*, 1–31.

Bonnefoy-Claudet, S., F. Cotton, and P.-Y. Bard (2006), The nature of noise wavefield and its applications for site effects studies: A literature review, *Earth-Science Reviews*, *79*, 205–227, doi:10.1016/j.earscirev.2006.07.004.

Boué, P., P. Poli, M. Campillo, H. Pedersen, X. Briand, and P. Roux (2013), Teleseismic correlations of ambient seismic noise for deep global imaging of the Earth, *Geophys. J. Int.*, *194*, 844–848, doi:10.1093/gji/ggt160.

Boué, P., M. A. Denolle, N. Hirata, S. Nakagawa, and G. C. Beroza (2016), Beyond basin resonance: characterizing wave propagation using a dense array and the ambient seismic field, *Geophys. J. Int.*, *206*, 1261–1272, doi:10.1093/gji/ggw205.

Bowden, D. C., V. C. Tsai, and F. C. Lin (2015), Site amplification, attenuation, and scattering from noise correlation amplitudes across a dense array in Long Beach, CA, *Geophys. Res. Lett.*, *42*, 1360–1367, doi:10.1002/2014GL062662.

Brenguier, F., N. M. Shapiro, M. Campillo, V. Ferrazzini, Z. Duputel, O. Coutant, and A. Nercessian (2008a), Towards forecasting volcanic eruptions using seismic noise, *Nature Geoscience*, *1*, 126–130, doi:10.1038/ngeo104.

Brenguier, F., M. Campillo, C. Hadziioannou, N. M. Shapiro, R. M. Nadeau, and E. Larose (2008b), Postseismic relaxation along the San Andreas fault at Parkfield from continuous seismological observations, *Science*, *321*, 1478–1481, doi: 10.1126/science.1160943.

Campillo, M., and A. Paul (2003), Long-range correlations in the diffuse seismic coda, *Science*, *299*, 547–549, doi:10.1126/science.1078551.

Campillo, M., J. C. Gariel, K. Aki, and F. J. Sánchez-Sesma (1989), Destructive strong ground motion in Mexico city: Source, path, and site effects during great 1985 Michoacán earthquake, *Bull. Seismol. Soc. Am.*, *79*, 1718–1735.

Cornell, C. A. (1968), Engineering seismic risk analysis, *Bull. Seismol. Soc. Am.*, *58*, 1583–1606.

Cultrera, G., G. Ameri, A. Saraò, A. Cirella, and A. Emolo (2013), Ground-motion simulations within ShakeMap methodology: application to the 2008 Iwate-Miyagi Nairiku (Japan) and 1980 Irpinia (Italy) earthquakes, *Geophys. J. Int.*, *193*, 220–237, doi: 10.1093/gji/ggs074.

Cupillard, P. and Y. Capdeville (2010), On the amplitude of surface waves obtained by noise correlation and the capability to recover the attenuation: a numerical approach, *Geophys. J. Int.*, *181*, 1687–1700, doi:10.1111/j.1365-246X.2010.04586.x.

Denolle, M. A. (2014), Seismic hazard analysis using the ambient seismic field, Ph.D. thesis, Stanford Univ., Stanford.

Denolle, M. A., E. M. Dunham, G. A. Prieto, and G. C. Beroza (2013), Ground motion prediction of realistic earthquake sources using the ambient seismic field, *J. Geophys. Res. Solid Earth*, *118*, 2102–2118, doi:10.1029/2012JB009603.

Denolle, M. A., E. M. Dunham, G. A. Prieto, and G. C. Beroza (2014a), Strong ground motion prediction using virtual earthquakes, *Science*, *343*, 399–403, doi: 10.1126/science.1245678.

Denolle, M. A., H. Miyake, S. Nakagawa, N. Hirata, and G. C. Beroza (2014b), Long-period seismic amplification in the Kanto Basin from the ambient seismic field, *Geophys. Res. Lett.*, *41*, 2319–2325, doi:10.1002/2014GL059425.

Douglas, J. (2014), Ground-motion prediction equations 1964-2014, Website: http://www.gmpe.org.uk.

Furumura, T., and T. Hayakawa (2007), Anomalous propagation of long-period ground motions recorded in Tokyo during the 23 October 2004 Mw 6.6 Niigata-ken Chuetsu, Japan, earthquake, *Bull. Seismol. Soc. Am.*, *97*, 863–880, doi:10.1785/0120060166.

Furumura, T., T. Hayakawa, M. Nakamura, K. Koketsu, and T. Baba (2008), Development of long-period ground motions from the Nankai Trough, Japan, earthquakes: Observations and computer simulation of the 1944 Tonankai (Mw 8.1) and the 2004 SE Off-Kii Peninsula (Mw 7.4) earthquakes, *Pure Appl. Geophys.*, *165*, 585–607, doi: 10.1007/s00024-008-0318-8.

Gerstoft, P., and T. Tanimoto (2007), A year of microseisms in southern California, *Geophys. Res. Lett.*, *34*, L20304, doi:10.1029/2007GL031091.

Graves, R., T. Jordan, S. Callaghan, E. Deelman, E. Field, G. Juve, C. Kesselman, P. Maechling, G. Mehta, K. Milner, D. Okaya, P. Small, and K. Vahi (2011), CyberShake: A physics-based seismic hazard model for Southern California, *Pure Appl. Geophys.*, *168*, 367–381, doi:10.1007/s00024-010-0161-6.

Graves, R. W., B. T. Aagaard, K. W. Hudnut, L. M. Star, J. P. Stewart, and T. H. Jor-

dan (2008), Broadband simulations for Mw 7.8 southern San Andreas earthquakes: Ground motion sensitivity to rupture speed, *Geophys. Res. Lett.*, *35*, L22302, doi: 10.1029/2008GL035750.

Gutenberg, B. (1911), Die seismische bodenunruhe [in German], Ph.D. thesis, University of Gottigen, Germany.

Harmon, N., D. Forsyth, and S. Webb (2007), Using ambient seismic noise to determine short-period phase velocities and shallow shear velocities in young oceanic lithosphere, *Bull. Seismol. Soc. Am.*, *97*, 2009–2023, doi:10.1785/0120070050.

Harmon, N., T. Henstock, F. Tilmann, A. Rietbrock, and P. Barton (2012), Shear velocity structure across the Sumatran Forearc-Arc, *Geophys. J. Int.*, *189*, 1306–1314, doi:10.1111/j.1365-246X.2012.05446.x.

Hartzell, S. H. (1978), Earthquake aftershocks as Green's functions, *Geophys. Res. Lett.*, *5*, 1–4, doi:10.1029/GL005i001p00001.

Hasselmann, K. (1963), A statistical analysis of the generation of microseisms, *Reviews of Geophysics*, *1*, 177–210, doi:10.1029/RG001i002p00177.

Hayashida, T., M. Yoshimi, and H. Horikawa (2014), Estimation of surface wave group velocity beneath the Chukyo area, Japan [in Japanese with English abstract], *Zisin*, *66*, 127–145, doi:10.4294/zisin.66.127.

Herrmann, R., and C. Ammon (2002), Computer programs in seismology: Surface waves, receiver functions and crustal structure, *St. Louis University, St. Louis, MO*.

Housner, G. (1959), Behavior of structures during earthquakes, *J. Eng. Mech. Div.*, *85*, 109–129.

Irikura, K. (1983), Semi-empirical estimation of strong ground motions during large earthquake, *Bulletin of the Disaster Prevention Research Institute*, *33*, 63–104.

Joint Reconnaissance Committee on the Iwate-Miyagi Nairiku Earthquake Disaster in 2008 (2009), Reconnaissance report on the Iwate-Miyagi Nairiku Earthquake Disaster in 2008 [in Japanese].

Kanai, K., and T. Tanaka (1961), On microtremors VIII, *Bull. Earthq. Res. Inst., Univ. Tokyo*, *39*, 97–114.

Kanai, K., T. Tanaka, and K. Osada (1954), Measurement of the micro-tremor I, *Bull. Earthq. Res. Inst., Univ. Tokyo*, *32*, 199–209.

Kanai, K., T. Tanaka, K. Osada, T. Suzuki, T. Morishita, and S. Yoshizawa (1966), On microtremors X: earthquake damage to wooden houses, *Bull. Earthq. Res. Inst., Univ. Tokyo*, *44*, 199–209.

Kanamori, H., and D. L. Anderson (1975), Theoretical basis of some empirical relations in seismology, *Bull. Seismol. Soc. Am.*, *65*, 1073–1095.

Kasahara, K., S. Sakai, Y. Morita, N. Hirata, H. Tsuruoka, S. Nakagawa, K. Z. Nanjo, and K. Obara (2009), Development of the Metropolitan Seismic Observation network (MeSO-net) for Detection of Mega-thrust beneath Tokyo Metropolitan Area, *Bull. Earthq. Res. Inst., Univ. Tokyo*, *84*, 71–88.

Kato, K., K. Aki, and T.-L. Teng (1993), 3-D simulations of surface wave propagation in the Kanto sedimentary basin, Japan—part 1: Application of the surface wave Gaussian beam method, *Bull. Seismol. Soc. Am.*, *83*, 1676–1699.

Kohler, M. D., T. H. Heaton, and S. C. Bradford (2007), Propagating waves in the steel, moment-frame factor building recorded during earthquakes, *Bull. Seismol. Soc. Am.*,

97, 1334–1345, doi:10.1785/0120060148.

Koketsu, K., and S. Higashi (1992), Three-dimensional topography of the sediment/basement interface in the Tokyo Metropolitan area, Central Japan, *Bull. Seismol. Soc. Am.*, *82*, 2328–2349.

Koketsu, K., and M. Kikuchi (2000), Propagation of seismic ground motion in the Kanto basin, Japan, *Science*, *288*, 1237–1239, doi:10.1126/science.288.5469.1237.

Koketsu, K., K. Hatayama, T. Furumura, Y. Ikegami, and S. Akiyama (2005), Damaging long-period ground motions from the 2003 Mw 8.3 Tokachi-oki, Japan earthquake, *Seismol. Res. Lett.*, *76*, 67–73, doi:10.1785/gssrl.76.1.67.

Koketsu, K., H. Miyake, H. Fujiwara, and T. Hashimoto (2008), Progress towards a Japan integrated velocity structure model and long-period ground motion hazard map, *Proceedings of the 14th World Conference on Earthquake Engineering*, pp. S10–038.

Koketsu, K., H. Miyake, Afnimar, and Y. Tanaka (2009), A proposal for a standard procedure of modeling 3-D velocity structures and its application to the Tokyo metropolitan area, Japan, *Tectonophysics*, *472*, 290–300, doi:10.1016/j.tecto.2008.05.037.

Koketsu, K., H. Miyake, and H. Suzuki (2012), Progress towards a Japan integrated velocity structure model and long-period ground motion hazard map, *Proceedings of the 15th World Conference on Earthquake Engineering*, p. 1773.

Komatitsch, D., Q. Liu, J. Tromp, P. Süss, C. Stidham, and J. H. Shaw (2004), Simulations of ground motion in the Los Angeles basin based upon the spectral-element method, *Bull. Seismol. Soc. Am.*, *94*, 187–206, doi:10.1785/0120030077.

Kudo, K. (1978), The contribution of Love waves to strong ground motions, *Proceedings of the 2nd International Conference on Microzonation*, *2*, 765–776.

Kudo, K. (1980), A study on the contribution of surface wave to strong ground motions, *Proceedings of the 7th World Conference on Earthquake Engineering*, pp. 499–506.

Li, Y.-G. (2012), *Imaging, modeling and assimilation in seismology*, Berlin: De Gruyter, http://site.ebrary.com/id/10554708.

Lin, F.-C., M. P. Moschetti, and M. H. Ritzwoller (2008), Surface wave tomography of the western United States from ambient seismic noise: Rayleigh and Love wave phase velocity maps, *Geophys. J. Int.*, *173*, 281–298, doi:10.1111/j.1365-246X.2008.03720.x.

Lobkis, O. I., and R. L. Weaver (2001), On the emergence of the Green's function in the correlations of a diffuse field, *The Journal of the Acoustical Society of America*, *110*, 3011–3017, doi:10.1121/1.1417528.

Longuet-Higgins, M. S. (1950), A Theory of the Origin of Microseisms, *Philosophical Transactions of the Royal Society of London A: Mathematical, Physical and Engineering Sciences*, *243*(857), 1–35.

Maeda, T., K. Obara, T. Furumura, and T. Saito (2011), Interference of long-period seismic wavefield observed by the dense Hi-net array in Japan, *J. Geophys. Res. Solid Earth*, *116*, B10303, doi:10.1029/2011JB008464.

Mamula, L., K. Kudo, and E. Shima (1984), Distribution of ground-motion amplification factors as a function of period (3-15 s), in Japan, *Bull. Earthq. Res. Inst., Univ. Tokyo*, *59*, 467–500.

McGuire, R. K. (2001), Deterministic vs. probabilistic earthquake hazards and risks, *Soil Dynamics and Earthquake Engineering*, *21*, 377–384, doi:10.1016/S0267-7261(01)00019-7.

Miyake, H., and K. Koketsu (2005), Long-period ground motions from a large offshore

earthquake: The case of the 2004 off the Kii peninsula earthquake, Japan, *Earth Planets Space*, *57*, 203–207, doi:10.1186/BF03351816.

Miyake, H., K. Koketsu, and T. Furumura (2008), Source modeling of subduction-zone earthquakes and long-period ground motion validation in the Tokyo metropolitan area, *Proceedings of the 14th World Conference on Earthquake Engineering*, *Paper No. S10-012*.

Mordret, A., M. Landès, N. M. Shapiro, S. C. Singh, and P. Roux (2014), Ambient noise surface wave tomography to determine the shallow shear velocity structure at Valhall: depth inversion with a Neighbourhood Algorithm, *Geophys. J. Int.*, *198*, 1514–1525, doi:10.1093/gji/ggu217.

Nakamura, Y. (1989), A method for dynamic characteristics estimation of subsurface using microtremor on the ground surface, *Quarterly Report of Railway Tech. Res. Inst.*, *30*, 25–30.

Nakamura, Y. (2000), Clear identification of fundamental idea of Nakamura's technique and its applications., in *Proceedings of the 12th World Conference on Earthquake Engineering*, Auckland, New Zealand.

Nakata, N., and R. Snieder (2014), Monitoring a building using deconvolution interferometry. II: ambient-vibration analysis, *Bull. Seismol. Soc. Am.*, *104*, 204–213, doi: 10.1785/0120130050.

Nakata, N., R. Snieder, S. Kuroda, S. Ito, T. Aizawa, and T. Kunimi (2013), Monitoring a building using deconvolution interferometry. I: Earthquake-data analysis, *Bull. Seismol. Soc. Am.*, *103*, 1662–1678, doi:10.1785/0120120291.

Nakata, N., J. P. Chang, J. F. Lawrence, and P. Boué (2015a), Body wave extraction and

tomography at Long Beach, California, with ambient-noise interferometry, *J. Geophys. Res. Solid Earth*, *120*, 1159–1173, doi:10.1002/2015JB011870.

Nakata, N., W. Tanaka, and Y. Oda (2015b), Damage detection of a building caused by the 2011 Tohoku-Oki earthquake with seismic interferometry, *Bull. Seismol. Soc. Am.*, *105*, 2411–2419, doi:10.1785/0120140220.

Nishida, K., H. Kawakatsu, and K. Obara (2008), Three-dimensional crustal S wave velocity structure in Japan using microseismic data recorded by Hi-net tiltmeters, *J. Geophys. Res. Solid Earth*, *113*, B10302, doi:10.1029/2007JB005395.

Nogoshi, M., and T. Igarashi (1970), On the propagation characteristics of microtremors [in Japanese with English abstract], *J. Seism. Soc. Japan*, *23*, 264–280.

Nogoshi, M., and T. Igarashi (1971), On the propagation characteristics of microtremors-part 2 [in Japanese with English abstract], *J. Seism. Soc. Japan*, *24*, 24–40.

Obara, K., K. Kasahara, S. Hori, and Y. Okada (2005), A densely distributed high-sensitivity seismograph network in Japan: Hi-net by National Research Institute for Earth Science and Disaster Prevention, *Rev. Sci. Instrum.*, *76*, 021301, doi: 10.1063/1.1854197.

Okada, Y., K. Kasahara, S. Hori, K. Obara, S. Sekiguchi, H. Fujiwara, and A. Yamamoto (2004), Recent progress of seismic observation networks in Japan - Hi-net, F-net, K-NET and KiK-net, *Earth Planets Space*, *56*, xv–xxviii, doi:10.1186/BF03353076.

Olsen, K. B., S. M. Day, J. B. Minster, Y. Cui, A. Chourasia, M. Faerman, R. Moore, P. Maechling, and T. Jordan (2006), Strong shaking in Los Angeles expected from southern San Andreas earthquake, *Geophys. Res. Lett.*, *33*, L07305, doi: 10.1029/2005GL025472.

Olsen, K. B., S. M. Day, L. A. Dalguer, J. Mayhew, Y. Cui, J. Zhu, V. M. Cruz-Atienza, D. Roten, P. Maechling, T. H. Jordan, D. Okaya, and A. Chourasia (2009), ShakeOut-D: Ground motion estimates using an ensemble of large earthquakes on the southern San Andreas fault with spontaneous rupture propagation, *Geophys. Res. Lett.*, *36*, L04303, doi:10.1029/2008GL036832.

Poli, P., H. A. Pedersen, M. Campillo, and t. P. W. Group (2012), Emergence of body waves from cross-correlation of short period seismic noise, *Geophys. J. Int.*, *188*, 549–558, doi:10.1111/j.1365-246X.2011.05271.x.

Prieto, G. A., and G. C. Beroza (2008), Earthquake ground motion prediction using the ambient seismic field, *Geophys. Res. Lett.*, *35*, L14304, doi:10.1029/2008GL034428.

Prieto, G. A., J. F. Lawrence, A. I. Chung, and M. D. Kohler (2010), Impulse response of civil structures from ambient noise analysis, *Bull. Seismol. Soc. Am.*, *100*, 2322–2328, doi:10.1785/0120090285.

Roux, P., K. G. Sabra, P. Gerstoft, W. A. Kuperman, and M. C. Fehler (2005), P-waves from cross-correlation of seismic noise, *Geophys. Res. Lett.*, *32*, L19303, doi:10.1029/2005GL023803.

Sabra, K. G., P. Gerstoft, P. Roux, W. A. Kuperman, and M. C. Fehler (2005), Extracting time-domain Green's function estimates from ambient seismic noise, *Geophys. Res. Lett.*, *32*, L03310, doi:10.1029/2004GL021862.

Sakai, S., and N. Hirata (2009), Distribution of the Metropolitan Seismic Observation network, *Bull. Earthq. Res. Inst., Univ. Tokyo*, *84*, 57–69.

Sánchez-Sesma, F., L. Pérez-Rocha, and E. Reinoso (1993), Ground motion in Mexico City during the April 25, 1989, Guerrero earthquake, *Tectonophysics*, *218*, 127–140,

doi:10.1016/0040-1951(93)90264-K.

Savage, M. K., F.-C. Lin, and J. Townend (2013), Ambient noise cross-correlation observations of fundamental and higher-mode Rayleigh wave propagation governed by basement resonance, *Geophys. Res. Lett.*, *40*, 3556–3561, doi:10.1002/grl.50678.

Shapiro, N. M., and M. Campillo (2004), Emergence of broadband Rayleigh waves from correlations of the ambient seismic noise, *Geophys. Res. Lett.*, *31*, L07614, doi:10.1029/2004GL019491.

Shapiro, N. M., M. Campillo, L. Stehly, and M. H. Ritzwoller (2005), High-resolution surface-wave tomography from ambient seismic noise, *Science*, *307*, 1615–1618, doi:10.1126/science.1108339.

Snieder, R., and E. Şafak (2006), Extracting the building response using seismic interferometry: Theory and application to the Millikan Library in Pasadena, California, *Bull. Seismol. Soc. Am.*, *96*, 586–598, doi:10.1785/0120050109.

Somerville, P., K. Irikura, R. Graves, S. Sawada, D. Wald, N. Abrahamson, Y. Iwasaki, T. Kagawa, N. Smith, and A. Kowada (1999), Characterizing crustal earthquake slip models for the prediction of strong ground motion, *Seismol. Res. Lett.*, *70*, 59–80, doi:10.1785/gssrl.70.1.59.

Stehly, L., M. Campillo, and N. M. Shapiro (2006), A study of the seismic noise from its long-range correlation properties, *J. Geophys. Res. Solid Earth*, *111*, B10306, doi:10.1029/2005JB004237.

Stockwell, R. G., L. Mansinha, and R. P. Lowe (1996), Localization of the complex spectrum: the S transform, *IEEE Trans Signal Processing*, *44*, 998–1001.

Suzuki, H. (1996), Geology of the Koto deep borehole observatory and geological struc-

ture beneath the Metropolitan Area, Japan [in Japanese with English abstract], *Rep. Natl. Res. Inst. Earth Sci. Disaster Prev.*, *56*, 77–123.

Suzuki, H. (1999), Deep geological structure and seismic activity in Tokyo Metropolitan area [in Japanese with English abstract], *J. Geogr.*, *108*, 336–339.

Suzuki, W., S. Aoi, and H. Sekiguchi (2010), Rupture process of the 2008 Iwate–Miyagi Nairiku, Japan, earthquake derived from near-source strong-motion records, *Bull. Seismol. Soc. Am.*, *100*, 256–266, doi:10.1785/0120090043.

Takagi, R., and K. Obara (2014), Spatiotemporal variation of ambient noise wavefield in Japan, *Abstract S41A–4432*, *presented at 2014 Fall Meeting, AGU, San Francisco, Calif., 15-19 dec*.

Takemura, S., M. Akatsu, K. Masuda, K. Kajikawa, and K. Yoshimoto (2015), Long-period ground motions in a laterally inhomogeneous large sedimentary basin: observations and model simulations of long-period surface waves in the northern Kanto Basin, Japan, *Earth Planets Space*, *67*, 33, doi:10.1186/s40623-015-0201-7.

Takeo, A., K. Nishida, T. Isse, H. Kawakatsu, H. Shiobara, H. Sugioka, and T. Kanazawa (2013), Radially anisotropic structure beneath the Shikoku Basin from broadband surface wave analysis of ocean bottom seismometer records, *J. Geophys. Res. Solid Earth*, *118*, 2878–2892, doi:10.1002/jgrb.50219.

Takewaki, I., S. Murakami, K. Fujita, S. Yoshitomi, and M. Tsuji (2011), The 2011 off the Pacific coast of Tohoku earthquake and response of high-rise buildings under long-period ground motions, *Soil Dyn. Earthq. Eng.*, *31*, 1511–1528, doi:10.1016/j.soildyn.2011.06.001.

Todorovska, M. I., and M. D. Trifunac (2008), Impulse response analysis of the Van

Nuys 7-storey hotel during 11 earthquakes and earthquake damage detection, *Structural Control and Health Monitoring*, *15*, 90–116, doi:10.1002/stc.208.

Tsuno, S., M. Yoshikawa, T. Uetake, and K. Kudo (2003), S-wave velocity structures in the southern Shizuoka prefecture determined by dispersion of surface waves of microtremors and strong motion data, *Summ. Tech. Pap. Ann. Meet. Archit. Inst. Jpn.*, *21135*.

Viens, L., A. Laurendeau, L. F. Bonilla, and N. M. Shapiro (2014), Broad-band acceleration time histories synthesis by coupling low-frequency ambient seismic field and high-frequency stochastic modelling, *Geophys. J. Int.*, *199*, 1784–1797, doi:10.1093/gji/ggu362.

Viens, L., H. Miyake, and K. Koketsu (2015), Long-period ground motion simulation of a subduction earthquake using the offshore-onshore ambient seismic field, *Geophys. Res. Lett.*, *42*, 5282–5289, doi:10.1002/2015GL064265.

Viens, L., K. Koketsu, H. Miyake, S. Sakai, and S. Nakagawa (2016), Basin-scale Green's functions from the ambient seismic field recorded by MeSO-net stations, *J. Geophys. Res. Solid Earth*, *121*, 2507–2520, doi:10.1002/2016JB012796.

Yamada, M., J. Mori, and T. Heaton (2009), The slapdown phase in high-acceleration records of large earthquakes, *Seismol. Res. Lett.*, *80*, 559–564, doi:10.1785/gssrl.80.4.559.

Yamanaka, H., and N. Yamada (2002), Estimation of 3D S-wave velocity model of deep sedimentary layers in Kanto plain, Japan, using microtremor array measurements [in Japanese with English abstract], *Butsuri Tansa*, *55*, 53–65.

Yamanaka, H., and N. Yamada (2006), Modeling 3D S-wave velocity structure of Kanto

basin for estimation of earthquake ground motion [in Japanese with English abstract], *Butsuri Tansa*, *59*, 549–560, doi:10.3124/segj.59.549.

Yokota, Y., K. Koketsu, K. Hikima, and S. Miyazaki (2009), Ability of 1-Hz GPS data to infer the source process of a medium-sized earthquake: The case of the 2008 Iwate-Miyagi Nairiku, Japan, earthquake, *Geophys. Res. Lett.*, *36*, L12301, doi: 10.1029/2009GL037799.

Yoshimoto, K., and S. Takemura (2014), A study on the predominant period of long-period ground motions in the Kanto Basin, Japan, *Earth Planets Space*, *66*, 100, doi: 10.1186/1880-5981-66-100.

Appendix: Code Verification

Prediction of earthquake ground motions using computer programs faces two challenging issues: verification and validation of the codes that are used to perform the simulations. As described by *Li* (2012) for numerical methods, the verification is the comparison of the results obtained by several codes for one specific problem. On the other hand, the validation refers to the comparison of the simulated ground motions with the observed ones. In this thesis, we only focused on the validation by simulating the recorded ground motions of different kinds of earthquakes with Green's functions extracted from the ambient seismic field.

Physics-based simulations usually verify the numerical solution with an analytical solution. For Green's functions extracted from the ambient seismic field, the real Green's function is unknown and it is impossible to generate an analytical solution. As this technique is relatively new, the ground motions of moderate earthquakes have been only simulated by extracted Green's functions in a few studies (e.g., *Prieto and Beroza* (2008) and *Denolle et al.* (2013) in California, and *Viens et al.* (2014), *Viens et al.* (2015), and *Viens et al.* (2016) in Japan). *Denolle* (2014) and *Denolle et al.* (2014b) also extracted Green's functions between MeSO-net stations and used them to study the site amplification in the Kanto basin.

To verify the accuracy of the codes used in this study, we compare the waveforms of the extracted Green's functions with the ones obtained by *Denolle* (2014) in the Kanto

basin. We use the N.CHSH Hi-net station as the virtual source and 4 MeSO-net stations as receivers. These stations are shown in Figure A1. *Denolle* (2014) extracted the Green's functions using the data recorded from January to June 2013. In our study, the Green's functions are retrieved from the ambient seismic field recorded in October 2014. Moreover, *Denolle* (2014) did not use any water level on the denominator term of the deconvolution to compute the Green's functions. Despite the difference between the data-set and a slightly different processing, the extracted Green's functions for these two studies agree very well in the period range of 3 to 10 s (Figure A2). At the present stage, this is the only comparison that can be done with another study to verify the accuracy of the codes.

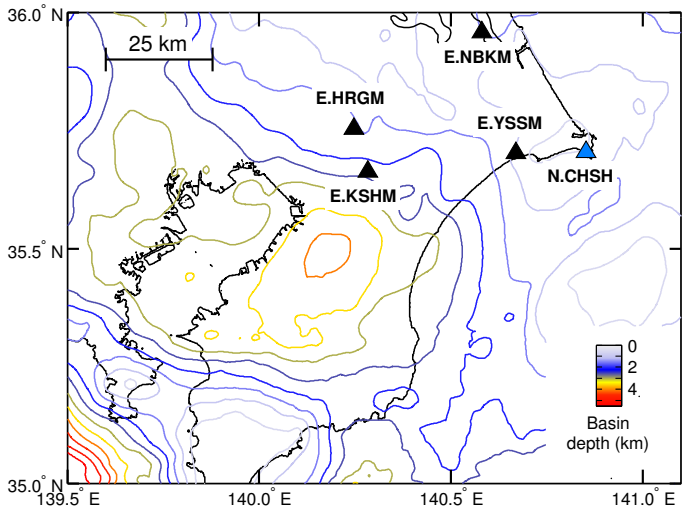

Figure A1: Map of the Kanto basin depth including the virtual source (N.CHSH) and the 4 receiver stations. Coast lines are shown in black.

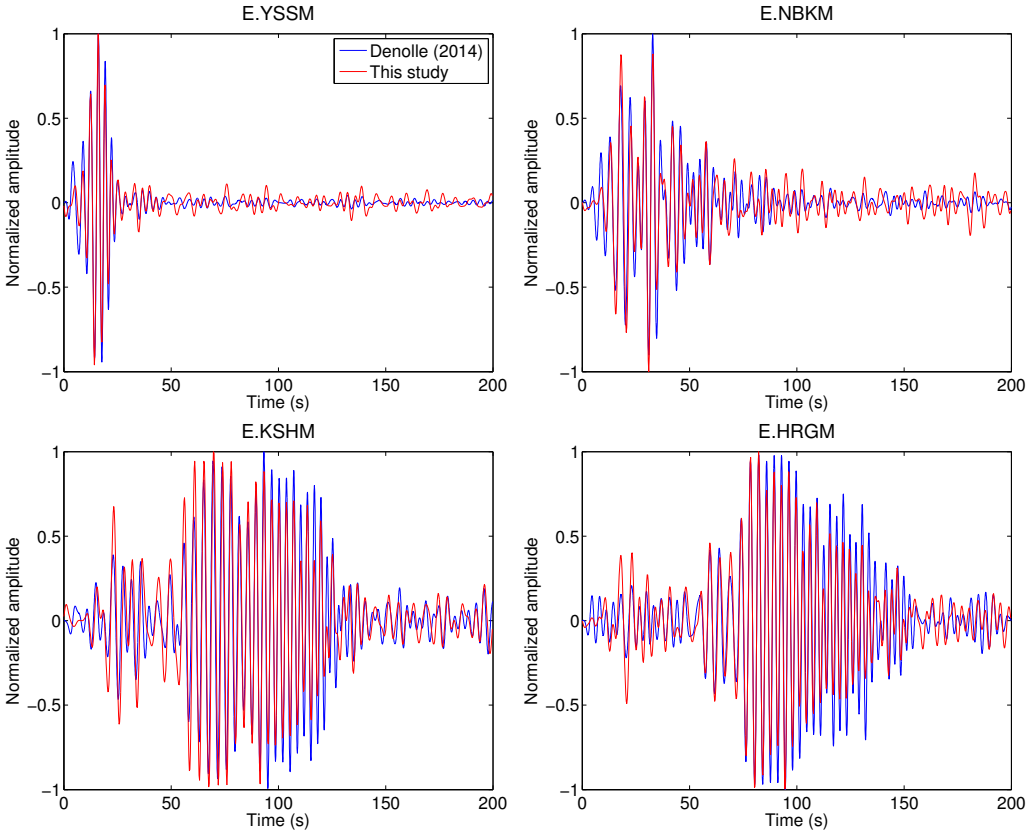

Figure A2: Comparison between the normalized waveforms obtained by *Denolle* (2014) (blue) and this study (red) for the 4 MeSO-net stations shown in Figure A1. The Green's functions (causal part) are shown for the vertical component and are bandpass filtered between 3 and 10 s.